Missouri S&T Library and Learning Resources

Scholars' Mine

Doctoral Dissertations | Student Theses and Dissertations

Spring 2024

Modeling and Analysis Methods for ESD and EMI Problems

Xin Yan
Missouri University of Science and Technology

Follow this and additional works at: https://scholarsmine.mst.edu/doctoral_dissertations

Part of the Electrical and Computer Engineering Commons

Department: Electrical and Computer Engineering

Recommended Citation

Yan, Xin, "Modeling and Analysis Methods for ESD and EMI Problems" (2024). *Doctoral Dissertations*. 3298.
https://scholarsmine.mst.edu/doctoral_dissertations/3298

This thesis is brought to you by Scholars' Mine, a service of the Missouri S&T Library and Learning Resources. This work is protected by U. S. Copyright Law. Unauthorized use including reproduction for redistribution requires the permission of the copyright holder. For more information, please contact scholarsmine@mst.edu.

MODELING AND ANALYSIS METHODS FOR ESD AND EMI PROBLEMS

by

XIN YAN

A DISSERTATION

Presented to the Graduate Faculty of the

MISSOURI UNIVERSITY OF SCIENCE AND TECHNOLOGY

In Partial Fulfillment of the Requirements for the Degree

DOCTOR OF PHILOSOPHY

in

ELECTRICAL ENGINEERING

2023

Approved by:

Daryl Beetner, Advisor
Jun Fan, Co-Advisor
DongHyun (Bill) Kim
Chulsoon Hwang
Shaowei Deng

© 2023

Xin Yan

All Rights Reserved

PUBLICATION DISSERTATION OPTION

This dissertation consists of the following three articles, formatted in the style used by the Missouri University of Science and Technology:

Paper I, found on pages 4–30, has been published in IEEE Transactions on Electromagnetic Compatibility.

Paper II, found on pages 31–56, has been submitted to IEEE Transactions on Electromagnetic Compatibility.

Paper III, found on pages 57–71, has been published in IEEE Transactions on Electromagnetic Compatibility.

Paper IV, found on pages 72–91, is intended for submission to IEEE Transactions on Electromagnetic Compatibility.

ABSTRACT

Electrostatic discharge (ESD) failures and Electromagnetic interference (EMI) problems are becoming more critical in electronic devices and large systems. In this work, four studies are presented to model and analyze ESD and EMI problems.

First, a simplified physical-based model for deep-snapback transient voltage suppressors (TVS) is developed. While based on physics, the number of parameters and components is minimized. Results show that the proposed model captures the most important behaviors of the TVS response using a limited number of parameters, allowing the model to be tuned relatively easily using data obtained only from package-level transient and quasi-static measurements. Second, a phaseless EMI source imaging method is proposed based on microwave holography. The field produced by the device under test (DUT) is not measured directly; instead, the interference pattern between the emitted field and the reference wave is created and measured as a hologram. Third, a simulation methodology is presented to analyze the acoustic noise created by MLCCs on a PCB. A simulation model for the PCB vibration modal response is built to analyze the harmonic response of the PCB excited by the capacitor. Total response is obtained by multiplying the measured power noise spectrum on the MLCC with the simulated deformation of the PCB found from the harmonic response analysis. The proposed method shows promise for analyzing and predicting the acoustic noise from singing capacitors. Finally, the unwanted magnetic field coupling mechanism of shielded magnetic near-field probe is revealed and analyzed.

ACKNOWLEDGMENTS

I express my sincere appreciation and gratitude to my advisor, Dr. Daryl Beetner, and my co-advisor, Dr. Jun Fan, for their guidance and help throughout my M.S. and PhD studies. They guide me to build good research abilities and help me whenever I encountered difficulties.

I thanks to the professors I have been working with, Dr. Victor Khilkevich, Dr. DongHyun Kim, Dr. Chulsoon Hwang, and Dr. David Pommerenke for their priceless inspiration, guidance, and inclusiveness. Thanks to Dr. Shaowei Deng for serving on my doctoral committee and providing helpful feedback on my research work.

In addition, I express my thanks to my friends and all other faculty members in Missouri S&T EMC lab for their support, encouragement, and help in my research and coursework.

Finally, thanks to my parents for their love and support. Special thanks to my wife Wei Zhang, for her endless love and support. I'm so lucky to have you by my side.

This dissertation is based upon work supported partially by the National Science Foundation (NSF) under Grant No. IIP-1916535.

TABLE OF CONTENTS

Page

PUBLICATION DISSERTATION OPTION iii

ABSTRACT........ iv

ACKNOWLEDGMENTS v

LIST OF ILLUSTRATIONS........ x

LIST OF TABLES........ xiii

SECTION

1. INTRODUCTION........ 1

PAPER

I. A PHYSICS-BASED MODEL FOR SNAPBACK TYPE ESD PROTECTION DEVICES........ 4

ABSTRACT 4

1. INTRODUCTION........ 5

2. MODEL DESCRIPTION........ 7

2.1. COUPLED NPN AND PNP TRANSISTORS 7

2.2. CONDUCTIVITY MODULATION 8

2.3. AVALANCHE BREAKDOWN........ 9

2.4. JUNCTION AND DIFFUSION CAPACITANCES 10

2.5. OTHER COMPONENTS 10

3. CONVERGENCE ISSUES........ 11

4. MODEL VALIDATION........ 16

4.1. DEVICE LEVEL MODELING 16

4.2. SYSTEM LEVEL MODELING 19

5. MODEL TUNING 24

6. CONCLUSIONS 26

REFERENCES 27

II. MICROWAVE HOLOGRAPHY FOR EMI SOURCE IMAGING 31

ABSTRACT 31

1. INTRODUCTION 32

2. MICROWAVE HOLOGRAPHY IMAGING ALGORITHM 34

2.1. 2D ESM ALGORITHM 34

2.2. HOLOGRAM FORMATION AND RECONSTRUCTION 35

2.3. TWIN OBJECT EFFECT 37

2.4. MICROWAVE HOLOGRAPHY IMAGING ALGORITHM 40

3. MEASUREMENT VALIDATION 42

3.1. PASSIVE DUT – ANTENNA SOURCE 42

3.2. ACTIVE DUT – COMMERCIAL ROUTER 44

4. CONCLUSION 54

REFERENCES 55

III. A METHODOLOGY FOR PREDICTING ACOUSTIC NOISE FROM SINGING CAPACITORS IN MOBILE DEVICES 57

ABSTRACT 57

1. INTRODUCTION 58

2. ACOUSTIC NOISE MECHANISM AND ANALYSIS METHOD 60

2.1. MLCC AND PCB VIBRATION 60

2.2. MODAL ANALYSIS AND HARMONIC ANALYSIS 60

2.3. TOTAL RESPONSE 62

3. SIMULATION AND VALIDATION ON A REAL PRODUCT 62

3.1. MODAL ANALYSIS OF PCB 62

3.2. HARMONIC ANALYSIS OF PCB 65

3.3. MEASURED ACOUSTIC NOISE AND PREDICTED RESPONSE 66

4. CONCLUSIONS 69

REFERENCES 71

IV. UNWANTED FIELD COUPLING MECHANISM OF MAGNETIC NEAR-FIELD PROBE 72

ABSTRACT 72

1. INTRODUCTION 72

2. PROBE STRUCTURE AND UNWANTED COUPLING TEST 74

2.1. PROBE STRUCTURE 74

2.2. UNWANTED COUPLING TEST 75

3. UNWANTED MAGNETIC FIELD COUPLING MECHANISM 76

3.1. SYMMETRIC AND ASYMMETRIC PROBE 76

3.2. SHORTED MICROSTRIP 77

3.3. SURFACE CURRENT 80

3.4. UNWANTED MAGNETIC FIELD COUPLING MECHANISM 83

4. PROBE DESIGN OPTIMIZATION 85

5. CONCLUSION 87

REFERENCES 88

SECTION

2. CONCLUSIONS AND RECOMMENDATIONS 92

REFERENCES 94

VITA 102

LIST OF ILLUSTRATIONS

PAPER I Page

Figure 1. High-level circuit model of a SCR-type TVS. 7

Figure 2. PNP transistor represented by the modified Eber-moll model. 8

Figure 3. Comparisons of the peak TVS voltage versus TLP voltage simulated with different strategies to mitigate convergence issues. 11

Figure 4. Comparisons of the peak TVS voltage versus TLP voltage for different integration methods when using a fixed time step. 15

Figure 5. Measured and simulated response of the Nexperia PESD3V3Y1BSF TVS device. 17

Figure 6. Measurement and simulation comparisons for the Nexperia PESD1V2Y1BSF TVS device. 18

Figure 7. SEED test schematic. 19

Figure 8. Measured and simulated SEED simulation results for the PESD3V3Y1BSF TVS device when using a 1 ns TLP rise time. 21

Figure 9. Measured and simulated SEED simulation results for the PESD1V2Y1BSF TVS device when using a 1 ns TLP rise time. 22

Figure 10. Simulated (red) and measured (blue) transient currents and voltages associated with components in the SEED simulation when using TVS device PESD3V3Y1BSF and a 1 ns TLP rise time. 23

Figure 11. Simulated (red) and measured (blue) transient currents and voltages associated with components in the SEED simulation when using TVS device PESD1V2Y1BSF and a 1 ns TLP rise time. 23

PAPER II

Figure 1. 2D ESM setup. 34

Figure 2. In-line holography diagram. 35

Figure 3. A diagram of the twin object effect. 38

Figure 4. Simulated imaging of a point source. 39

Figure 5. Microwave holography imaging setup. 41

Figure 6. Horn antenna imaging (a) Measurement setup. (b) Top view to the scan area. 43

Figure 7. Horn antenna imaging results (a) Hologram (raw data). (b) Normalized hologram. (c) Ex Image at the source plane. 44

Figure 8. The commercial router. 45

Figure 9. Interior of an optical module. 45

Figure 10. Internet router imaging. 46

Figure 11. Top view to the scan area. 46

Figure 12. Measurement results of case 1. 48

Figure 13. Measurement results of case 2. 49

Figure 14. Measurement results of case 3. 50

Figure 15. Comparison between ESM and holographic imaging. 52

PAPER III

Figure 1. Mechanical model of the PCB. 63

Figure 2. Modal shapes associated with (a) Mode 1, and (b) Mode 2. 64

Figure 3. Power noise spectrum of the dominant MLCC. 65

Figure 4. The deformation of the structure. 66

Figure 5. Acoustic noise measurement setup. 67

Figure 6. Blue curve/dots: measured acoustic noise. 67

Figure 7. Flow chart of the proposed acoustic noise analysis. 70

PAPER IV

Figure 1. (a) Overview of the probe (b) Probe tip structure. 75

Figure 2. (a) Diagram of unwanted coupling test. (b) A typical distribution of the unwanted coupling across the microstrip. 76

Figure 3. (a) Structures of asymmetric and symmetric probes. (b) Unwanted coupling of asymmetric and symmetric probes. 77

Figure 4. (a) Shorted microstrips with air dielectric. (b) Off-center Ex and Hz field distributions along the 300 cm microstrip. (c) Diagram of probe positions for unwanted E and H field coupling. 78

Figure 5. Surface current from H-field coupling. 81

Figure 6. Surface current from E-field coupling. 82

Figure 7. Diagram of the unwanted magnetic field coupling mechanism. 83

Figure 8. Hy and Hz distributions above air microstrip with and without probe grounding structure. 85

Figure 9. Probe optimization methods. 86

Figure 10. Comparison of the Hy magnitude between original asymmetric probe and the probe with shield (design shown in Figure 9 (b)). 87

Figure 11. Comparisons of the optimization designs. 87

LIST OF TABLES

PAPER I Page

Table 1. Parameters of the TVS diode models 25

PAPER II

Table 1. Maximum field and radiated power comparison 53

Table 2. Maximum field and radiated power validation 53

PAPER III

Table 1. First eight modal frequencies of the DUT 64

Table 2. Comparison of the Broad Peaks 68

PAPER IV

Table 1. Unwanted Coupling from E-field and H-field 79

1. INTRODUCTION

With the increasing operating data rates of electronic devices, electromagnetic compatibility (EMC) and electromagnetic interference (EMI) issues are becoming more critical for both compact consumer devices and large systems. Near-field scanning methods are often utilized to investigate EMC issues and diagnose root-cause for compact devices, in which near-field probes are used for near-field pattern acquisition over the device under test (DUT). For large systems, emission source microscopy (ESM) techniques are often used to identify the radiating sources of the EMI that contribute to the far-field region, by measuring the radiated fields over a plane at an electrically large distance from the DUT and back-propagating the field onto the DUT plane.

Electrostatic discharge (ESD) and other similar transient electrical overstress events are also common causes of failure in integrated circuits (ICs). Although ESD events typically only last between 1 ns and 1 us, the peak current can reach tens of amperes. In order to provide system level ESD protection, the on- and off-chip protection must be designed to shunt the ESD current away from sensitive components during an ESD event, while still ensuring the normal operation of ICs. Critical to optimizing the off-chip protection strategy is system-efficient ESD design (SEED) simulations, which requires highly accurate transient device models.

In this dissertation, four papers are presented to model and analyze ESD and EMI problems. In the first paper, a simplified physics-based model for SCR-type snapback TVS devices was proposed. By reducing the number of components and parameters, the model can be relatively easily tuned using only measurements performed on the package

device, without the need for detailed silicon-level information. Issues with convergence were studied to determine its root cause and were eliminated by adding a non-linear damping resistance in series with the PN junction capacitance of the junction responsible for turn on. Device and system-level (SEED) simulations with two commercially available TVS devices were utilized to validate the model. Simulation results demonstrate matched measurements within about 20% for both quasistatic and transient results for each of the TLP conditions tested. The model show promise as a tool for representing TVS devices in SEED simulations.

In the second paper, we proposed a phaseless EMI source imaging method based on microwave holography, which is an alternative solution for localization and characterization of active radiation sources. The hologram is created by combining the field from the scan antenna with a reference signal collected by the second antenna placed near the DUT and naturally producing a much stronger signal than the scan antenna. The normalized hologram is backpropagated to the source plane and the image of sources is obtained. The proposed method is validated through measurements in which the radiation sources are visualized and localized successfully.

In the third paper, the mechanisms by which MLCCs generate acoustic noise on PCBs were studied, and a method for predicting the severity of that noise was presented. The inherent vibration properties of a PCB can be analyzed using modal analysis, and a transfer function for MLCC vibration to board response can be estimated using modal superposition. An equation predicting the PCB displacement from the MLCC/board transfer function and the MLCC power supply noise was proposed. The proposed methods were validated on a prototype earbud. The trends in the average predicted board

displacement are similar to the measured acoustic noise, with the major broad peaks in the acoustic noise found in both simulations and measurement. The proposed simulation methods show promise for analyzing the impact of singing capacitors on acoustic noise.

In the last paper, the unwanted magnetic field coupling of a magnetic near-field probe is analyzed and explained. A shorted microstrip is utilized to separate the magnetic and electric field coupling in the full wave simulation tool. Simulation results show that a symmetric stack-up PCB probe could mitigate the unwanted magnetic field effectively. The unwanted magnetic field coupling mechanism is validated through simulation, and improved designs are proposed.

PAPER

I. A PHYSICS-BASED MODEL FOR SNAPBACK TYPE ESD PROTECTION DEVICES

Xin Yan, Seyed Mostafa Mousavi, Li Shen, Yang Xu, Wei Zhang, Sergej Bub, Steffen Holland, and Daryl G. Beetner

ABSTRACT

A simplified physical-based model for deep-snapback transient voltage suppressors (TVS) is developed in this paper. While based on physics, the number of parameters and components is minimized so the model can be tuned easily from available measurements of the packaged TVS. SPICE convergence issues seen in previous snapback device models are eliminated by adding non-linear damping components to the model. No convergence issues were seen among any of the simulations performed for this study, which includes transmission-line pulse tests with multiple levels and rise times. The proposed model was used to represent two different TVS devices and was validated in both device- and system-level simulations. Simulations of quasi-static and transient behavior matched measurement results within about 20% among all of the tested cases.

Keywords: ESD protection, snapback, silicon-controlled rectifier (SCR), SEED simulation, transient voltage protection

1. INTRODUCTION

Electrostatic discharge (ESD) and other similar transient electrical overstress events are common causes of failure in integrated circuits (ICs). Although ESD events typically only last between 1 ns and 1 us, the peak current can reach tens of amperes. In order to provide system level ESD protection, the on- and off-chip protection must be designed to shunt the ESD current away from sensitive components during an ESD event, while still ensuring the normal operation of ICs. As the on-chip protection is often not effective against system-level ESD events, carefully designed and implemented off-chip protection is often required to achieve high levels of robustness. Critical to optimizing the off chip protection strategy is System-Efficient ESD Design (SEED) simulations, which require highly accurate transient device models [1][2].

Many transient voltage suppression (TVS) devices used for off chip protection are based on a silicon-controlled rectifier (SCR) response which features a deep snapback characteristic. SCR-type TVS devices are increasingly popular as they can handle large currents with a small holding voltage in a relatively small sized package and with low capacitance. A number of models for snapback type TVS devices have been proposed in the literature. The models in [3]-[5] closely represent the physics behind the operation of SCR type devices. While these models can be highly accurate, they cannot reasonably be used by an engineer who has little information about the detailed properties of the device, like its layout and doping characteristics. Tuning the models based on transmission line pulse (TLP) measurements would be extremely challenging due to the many equations and parameters contained within the model. The models in [6][7] were developed to

represent the fundamental behavior of TVS devices and to be easy to tune, but they only account for the steady-state IV curve of the device, and not its transient characteristics. The model in [8] is a behavioral model which captures some transient characteristics, but its ability to determine the voltage overshoot is limited. The authors of [9] develop a behavioral model which is capable of accurately capturing the transient characteristics of the TVS, but tuning becomes more difficult as the model becomes more complex and SPICE convergence issues have been observed during in-system simulations [10]. The model in [11] uses a voltage-controlled current-source to model ESD MOS snapback and is capable of reproducing double snapback behavior, but is only built to capture quasi-static IV characteristics, and not the transient response. Machine learning techniques are used in [12]-[14] to model snapback and non-snapback ESD devices. While manual tuning of the model is no longer needed in this case, the large amount of raw silicon data required to train the neural network presents challenges.

In addition to achieving good accuracy and being relatively easy to tune, models should also be robust to SPICE convergence issues. Such issues can be especially problematic in SEED simulations when both off-chip and on-chip protection devices are present, where the simultaneous highly nonlinear response of the two models presents significant challenges [10][15]. Adding more components to dampen the device response is a typical way to solve convergence issues for the TVS behavior model [8][10]. These convergence issues were seen with the physics-based model in [5] and were eliminated within the simulations shown in that study, but the convergence robustness in SEED simulations is still unknown.

2. MODEL DESCRIPTION

The proposed model is based on a modified Ebers-Moll model of coupled NPN and PNP transistors, with additional components to capture the transient behavior as shown in Figure 1 [5].

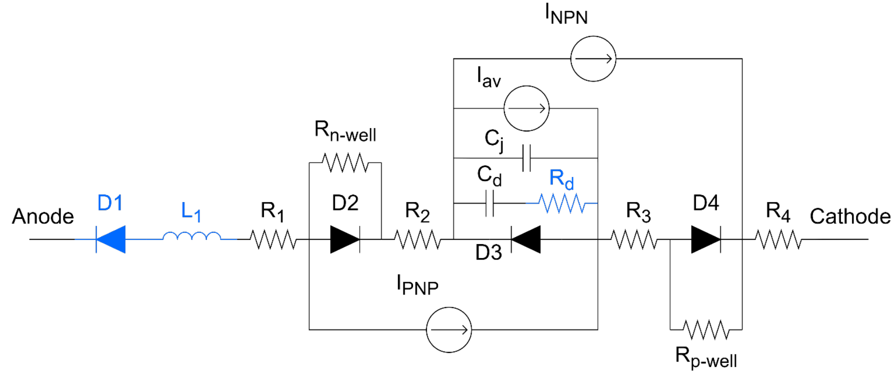

Figure 1. High-level circuit model of a SCR-type TVS. L_1 and D_1 were added to the model in [5] (shown in blue) to capture the transient behavior and to ease the tuning process. R_d was added to eliminate convergence issues.

2.1. COUPLED NPN AND PNP TRANSISTORS

The NPN or PNP transistors are represented by two ideal diodes and a controlled current source [5], as shown in Figure 2. The currents through the diodes and the current source are given by:

$$I_{D2} = \frac{I_s}{\beta_F} \left(e^{\frac{V_{EB}}{V_T}} - 1 \right), \tag{1}$$

$$I_{D3} = \frac{I_s}{\beta_R} \left(e^{\frac{V_{CB}}{V_T}} - 1 \right), \tag{2}$$

$$I_{PNP} = I_s \left(e^{\frac{V_{EB}}{V_T}} - e^{\frac{V_{CB}}{V_T}} \right), \tag{3}$$

where I_s is the leakage current, V_T is the thermal voltage, β_F and β_R are the forward and reverse gain of the BJT, respectively, and V_{EB} and V_{CB} are the emitter-to-base and collector-to-base voltages, respectively. The gains are assumed to be constant to help simplify this model. The coupled NPN and PNP transistors form the basic structure of the SCR type TVS device, along with the well resistances R_{n-well} and R_{p-well}.

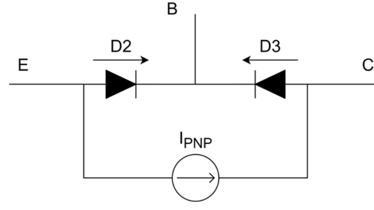

Figure 2. PNP transistor represented by the modified Eber-moll model.

2.2. CONDUCTIVITY MODULATION

Conductivity modulation describes the change in conductivity due to the change in carrier concentration of (typically) low-doped regions of the SCR. Conductivity modulation and the device inductance together determine the voltage overshoot across the TVS during turn on. In the proposed model, conductivity modulation is included in the (presumably lightly-doped) base resistors R_2 and R_3, as [16][17]:

$$R_2(t), R_3(t) = \frac{R_0}{1 + \frac{Q_{charge}(t)}{Q_0}}, \tag{4}$$

where R_0 is the resistance when current starts to flow, and Q_0 is the threshold charge required to establish increased conduction. The on-resistance of the device is separated from the modulated resistance and represented by R_1 and R_4. R_2 and R_3 are set equal to each other for simplicity in tuning. Q_{charge} is the charge injected into diode D_3, given by:

$$Q_{charge} = I_s\tau(e^{\frac{V_{D3}}{V_T}} - 1), \tag{5}$$

where τ is the transit time of the PN junction. R_0 and Q_0 determine the conductivity modulation voltage overshoot and the falling-edge of the voltage waveform at the end of a TLP excitation. They can be tuned from transient measurements of the TVS.

2.3. AVALANCHE BREAKDOWN

Avalanche breakdown which occurs in the middle junction, D_3, causes the SCR to turn on. The breakdown behavior needs to be accurately modeled to obtain the correct IV curve and transient waveforms. An approach similar to the one presented in [5] is used to model this behavior. The equation for the avalanche breakdown current is broken into 2 parts:

$$I_{av} = (I_s + I_{PNP} + I_{NPN})\left(\frac{1}{1 - \frac{V}{V_{BV}}^{n}} - 1\right), \quad when\ V < kV_{BV},\ k = 0.99 \tag{6}$$

$$I_{av} = (I_s + I_{PNP} + I_{NPN})\left(\frac{1}{1 - k^n} - 1\right) + \frac{V - kV_{BV}}{R}, \quad When\ V \geq kV_{BV},\ k = 0.99,\ R = 0.01 \tag{7}$$

The standard Miller multiplication expression is utilized in (6) when the reverse voltage on D_3 is smaller than or close to the breakdown voltage. When the reverse voltage is at or above the breakdown voltage the relationship between voltage and current is changed to a linear one to avoid singularity issues. In (6) and (7), V_{BV} is the breakdown voltage, and n is a constant which depends on the transistor's semiconductor characteristics (fixed here to 3, a typical value for silicon, for simplicity). The value of k is set close to 1 to ensure the breakdown occurs close to V_{BV}.

2.4. JUNCTION AND DIFFUSION CAPACITANCES

In a p-n junction, the junction capacitance C_j dominates when the diode is reverse biased and the diffusion capacitance C_d dominates when the diode is forward biased. Only the capacitance of the middle junction (D3) was considered in the proposed model, as it plays the most important role in the transient waveform when the device is turning on. In practice, once the diode is turned on, the junction capacitance could be fixed to a constant value. The current through the non-linear diffusion capacitance was modeled as:

$$I = \frac{dQ_{charge}}{dt} = \frac{d}{dt}\left[I_s\tau\left(e^{\frac{V_{D3}}{V_T}} - 1\right)\right] = \frac{I_s\tau}{V_T} \cdot e^{\frac{V_{D3}}{V_T}} \cdot \frac{dV_{D3}}{dt},$$
$$\text{where } \frac{I_s\tau}{V_T} \cdot e^{\frac{V_{D3}}{V_T}} = C_d \tag{8}$$

and C_d is the diffusion capacitance. When the device is reverse biased, the diffusion capacitance given by this equation is small and could cause numerical simulation issues. The diffusion capacitance is therefore set to zero when $V_{D3} < 0$.

2.5. OTHER COMPONENTS

R_1 and R_4 are used to represent the series resistance of the device and determine the slope of the quasi-static IV curve after the holding voltage is reached. L_1 is the inductance of the device and contributes to the peak level of the voltage overshoot. An ideal reversed diode D_1 was placed in series with other components to provide an additional voltage drop which can be tuned to match the measured characteristics of a variety of TVS devices.

3. CONVERGENCE ISSUES

The proposed model was implemented in Keysight ADS. While this model performed better in terms of convergence than in our experience with the previous TVS behavioral models based on switches [10][15], convergence issues were still observed. For example, Figure 3 (a) shows a plot of the peak transient waveform voltage across the TVS versus the TLP voltage when using the proposed model in a system-level simulation. The estimated peak voltage oscillates with the TLP voltage as a result of numerical oscillations in the simulation. While these oscillations could be mitigated by decreasing the simulation time step or changing the SPICE integration method, a TVS model which is naturally robust to convergence problems is preferred.

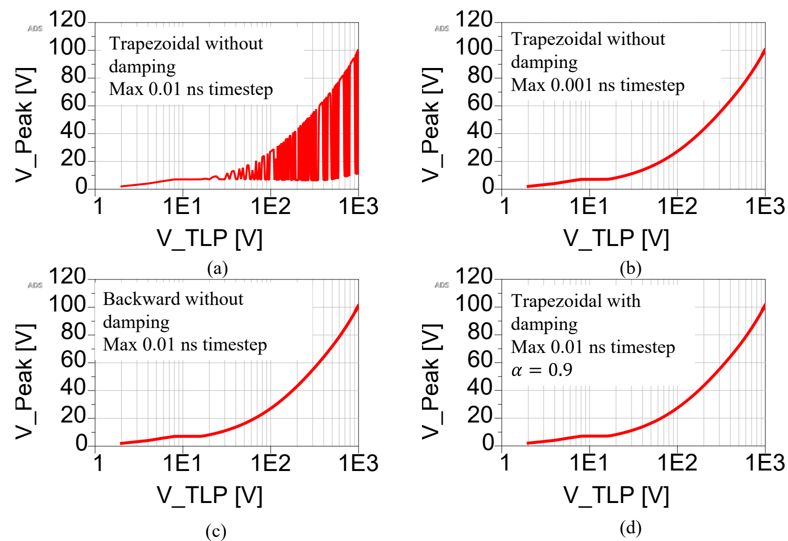

Figure 3. Comparisons of the peak TVS voltage versus TLP voltage simulated with different strategies to mitigate convergence issues. (a) Trapezoidal integration with maximum 0.01 ns time step, without damping. (b) Trapezoidal integration with maximum 0.001 ns time step, without damping. (c) Backward integration with maximum 0.01 ns time step, without damping. (d) Trapezoidal integration with maximum 0.01 ns time step, with damping $\alpha = 0.9$.

Two common events leading to numerical oscillations are a step change in current through an inductor or a step change in voltage across a capacitor. The trapezoidal integration method, which is an easily-implemented second order numerical integration technique used by SPICE and is the default integration method in ADS, is susceptible to such numerical oscillations. The iteration equation for this method is given by [18]:

$$y(t) = y(t - \Delta t) + \frac{\Delta t}{2}\big(x(t) + x(t - \Delta t)\big) \tag{9}$$

where $x = ky'$(and $k = 1$ is assumed for simplicity), Δt is the time step, and $x(t)$ an unknown to be solved. Equation (9) can be rewritten as:

$$x(t) = -x(t - \Delta t) + \frac{2}{\Delta t}(y(t) - y(t - \Delta t)) \tag{10}$$

From (10), if there is a step change of the input y from $t = t - \Delta t$ to $t = t$, and the value of y remains the same afterwards, x will take on a value equal to the negative of the previous value of x, and then will oscillate between those values. That is:

$$\begin{gathered} x(t + n\Delta t) = -x(t + (n-1)\Delta t), \\ \text{when } \; y(t + n\Delta t) = y(t + (n-1)\Delta t), n = 1,2,3.. \end{gathered} \tag{11}$$

These oscillations could be mitigated using the backward or Gear 2 integration method, shown in (12) and (13) respectively, as the value of x at the previous timestep is not part of the calculation.

$$y(t) = y(t - \Delta t) + \Delta t\big(x(t)\big) \tag{12}$$

$$y(t) = \frac{4}{3}y(t - \Delta t) - \frac{1}{3}y(t - 2\Delta t) + \frac{2}{3}\Delta t\big(x(t)\big) \tag{13}$$

One way to eliminate the numerical oscillations is to introduce damping [16]. The trapezoidal integration method with an added damping factor α is given by:

$$y(t) = y(t - \Delta t) + \frac{\Delta t}{2}\big((1 + \alpha)x(t) + (1 - \alpha)x(t - \Delta t)\big) \tag{14}$$

Rewriting (14) gives:

$$x(t) = -\frac{1 - \alpha}{1 + \alpha}x(t - \Delta t) + \frac{2}{\Delta t}\frac{1}{1 + \alpha}\big(y(t) - y(t - \Delta t)\big) \tag{15}$$

The damping factor α ranges in value from 0 to 1. Equation (15) shows that the damping is equivalent to a linear interpolation between the trapezoidal and backward integration methods. When α is equal to 1, trapezoidal integration with damping becomes the backward integration method. By adding an appropriate value for the damping factor, numerical oscillations could be suppressed in a few time steps without significantly impacting other simulation results.

Modeling an ideal capacitor using (14) is equivalent to using ordinary trapezoidal integration in a capacitor with a series “damping” resistance. Assuming an ideal capacitor with a capacitance C_0, the expression for the voltage and current using trapezoidal integration with damping is:

$$V(t) = V(t - \Delta t) + \frac{\Delta t}{2C_0}[(1 + \alpha)I(t) + (1 - \alpha)I(t - \Delta t)] \tag{16}$$

$$V(t) - V(t - \Delta t) = \frac{\Delta t}{2C_0}[I(t) + I(t - \Delta t)] + \frac{\alpha\Delta t}{2C_0}[I(t) - I(t - \Delta t)] \tag{17}$$

where (17) is a rewritten form of (16). The right-hand side of (17) has two terms. The first term is the ordinary trapezoidal integration for an ideal capacitor, and the second term comes from the damping, which is equivalent to a series resistor with $R = \alpha\Delta t/(2C_0)$. The resistance is determined by the damping factor α, the time step Δt, and the capacitance C_0.

In the proposed model, the numerical oscillation occurs during the turn on of the device. The voltage on the middle junction changes dramatically within a few time steps as does the value of the diffusion capacitance. Although there is no warning or error when numerical oscillations are present, and the transient simulation completes "successfully", unreasonably large currents and voltages were observed in simulations at the junction after break down, which suggested the diffusion capacitance was the root cause. To eliminate the numerical oscillation in the proposed model, a non-linear damping resistance, R_d, was added in series with the diffusion capacitance with a value determined by an equation derived from (8) and (17) as

$$R_d = \frac{\alpha \Delta t}{2\frac{I_s \tau}{V_T} \cdot e^{\frac{V_n}{V_T}}} \tag{18}$$

The damping resistance R_d was implemented in ADS by setting the value of Δt to the internal variable 'timestep'. During the default ADS simulation approach based on truncation error, this timestep will change throughout the simulation. By allowing the value of R_d to change accordingly ensures only the required level of damping is used and no more at each simulation interval.

Figure 3 shows the impact of different convergence mitigation strategies when using the model to predict the peak transient voltage across the TVS in a system-level simulation. Numerical oscillations in the results are observed in Figure 3 (a) when using a maximum 0.01 ns time step an no damping. These oscillations could be eliminated by reducing the time step as shown in Figure 3 (b), though simulation time will increase and the user must be on the lookout for such issues and be ready to modify the simulation time if required. Figure 3 (c) shows the oscillations can also be eliminated using the

backward integration method without reducing the 0.01 ns time step. Figure 3 (d) shows the results when adding the proposed dynamic damping resistance R_d to the model. The numerical oscillations were eliminated in this case without reducing the time step or requiring additional actions from the user.

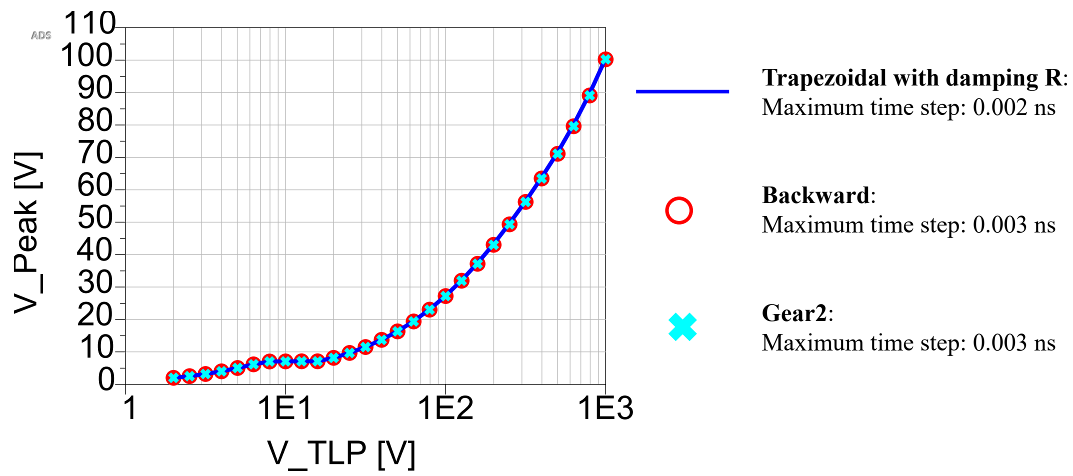

Figure 4. Comparisons of the peak TVS voltage versus TLP voltage for different integration methods when using a fixed time step. Results are shown for the maximum simulation time step which yields consistently stable results.

If this model was implemented in a SPICE tool where the time step was unavailable, a value of R_d could be used which was sufficiently large to make convergence issues unlikely, or a fixed simulation timestep could be used along with an appropriate value of R_d. In this case, the maximum time step should be smaller than those encountered using the truncation error method to avoid unstable results or errors, no matter which integration method is used. Figure 4 shows that the three integration methods can have similar performance if the correct maximum timestep is chosen. The disadvantage compared to the proposed damping resistance, however, is that the user

must be aware of how to tune the simulation to ensure convergence and, in fact, must be aware that a convergence issue occurred.

4. MODEL VALIDATION

4.1. DEVICE LEVEL MODELING

The model was validated through application to two commercial SCR-type TVS devices, the Nexperia PESD3V3Y1BSF [19] and the Nexperia PESD1V2Y1BSF [20]. The turn-on behavior of each TVS was measured through very fast transmission line pulse (VF-TLP) testing. An ESD-EMC TLP-ES620-50 compact pulsed IV-curve system along with a 2 GHz 10 GSa/s Rohde & Schwarz oscilloscope was used to create and record the 10 ns TLP waveforms with a rise time of 0.65 ns. Both quasi-static IV curves and the transient responses were captured using the TLP software. The proposed model was then tuned based on the measured results. Examples of the measured and simulated quasi-static and transient results for the PESD3V3Y1BSF TVS device are shown in Figure 5.

Simulations were performed using an ideal voltage source representing the TLP pulse. The quasi-static IV curve was obtained by calculating the average voltage and current in a time window from 7 ns to 9 ns, similar to the measured results. As shown in Figure 5 (a), the simulated quasi-static IV curve matches with measured curve well, within about a 10% error. As the TLP pulse was only 10 ns long, self-heating can be ignored. Figure 5 (b) compares the transient response for two example TLP voltages. Although there is a small discrepancy between simulations and measurements at low TLP

levels (e.g. at 10 V), the overall simulation matches measurements well, particularly at higher voltages (e.g. above 100 V). The voltage overshoot and the falling edges of the waveform were captured well.

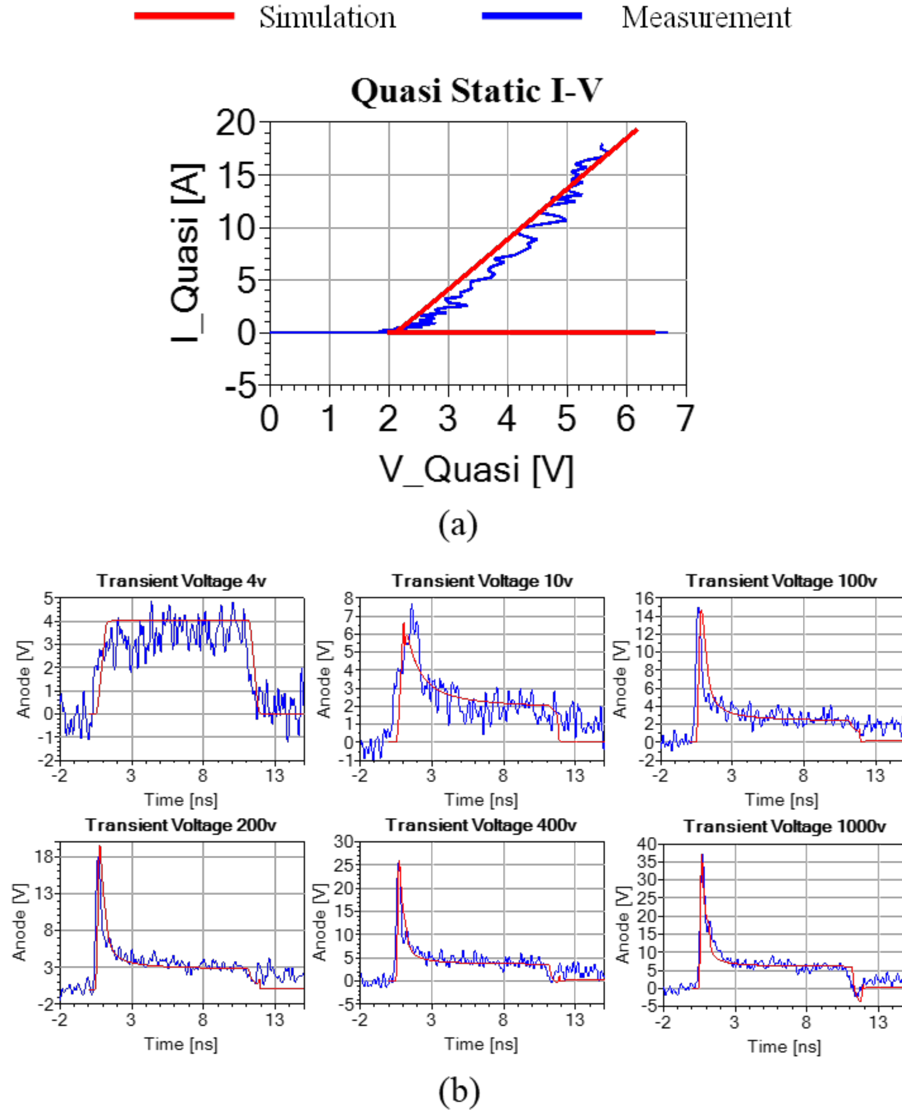

Figure 5. Measured and simulated response of the Nexperia PESD3V3Y1BSF TVS device. Measurements are shown in blue and simulations in red. (a) Quasi-static IV curve. (b) Transient responses for six TLP voltages.

Figure 6 shows the measured and simulated results when modeling the Nexperia PESD1V2Y1BSF TVS device. The simulated results also closely match the measured quasi-static IV and transient curves, within about an 10% maximum error.

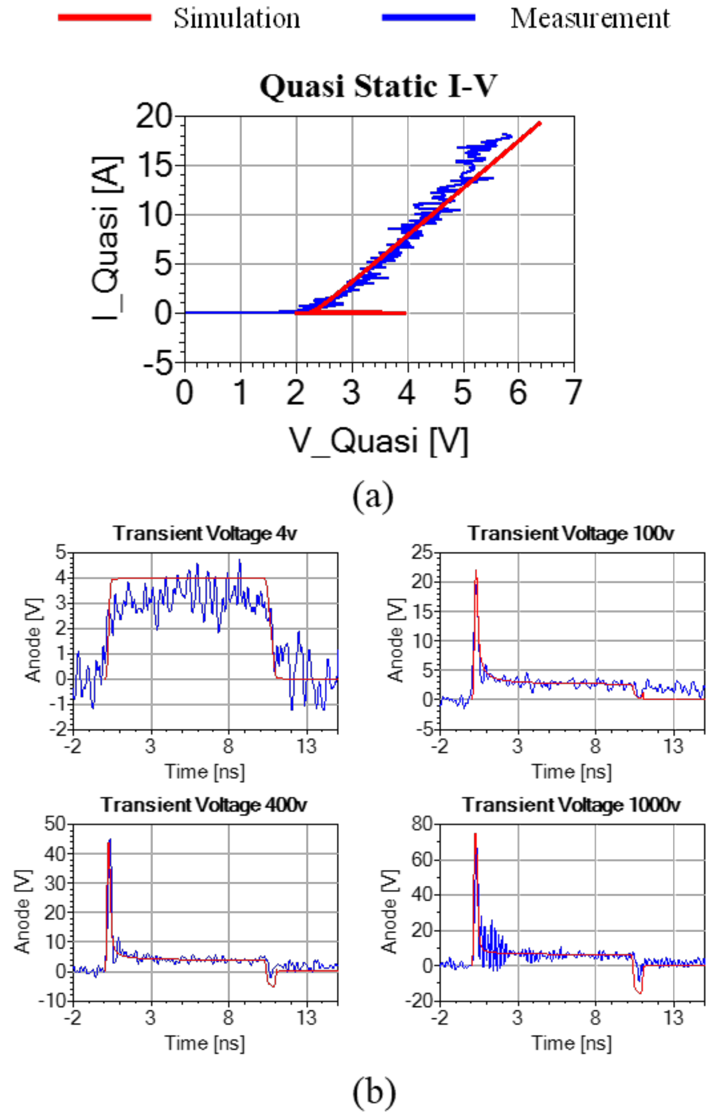

Figure 6. Measurement and simulation comparisons for the Nexperia PESD1V2Y1BSF TVS device. Measurements are shown in blue and simulations in red. (a) Quasi-static IV curve. (b) Transient responses for four TLP voltages.

4.2. SYSTEM LEVEL MODELING

The ability to predict the interaction between two ESD protection devices is more challenging than capturing the behavior of one device alone. The proposed model was validated in a System Efficient ESD Design (SEED) simulation where an off-chip protection device protected an IC with an on-chip diode, with a 50-ohm trace in between, as shown in Figure 7. The IC was represented by a protection diode and the two modeled TVS devices were used as the off-chip protection in subsequent simulations. A 20 ns TLP pulse was injected into one end of the trace. The rise time of the pulse was varied from 0.65 ns to 5 ns and the level from 10 V to 94 V with a linear step of 6 V. The transient voltages and currents at the IC and at the off-chip TVS device were captured as described in [9][15]. The measured TLP voltage when injecting into a 50-ohm load was also captured and used as the source waveform in the SEED simulations.

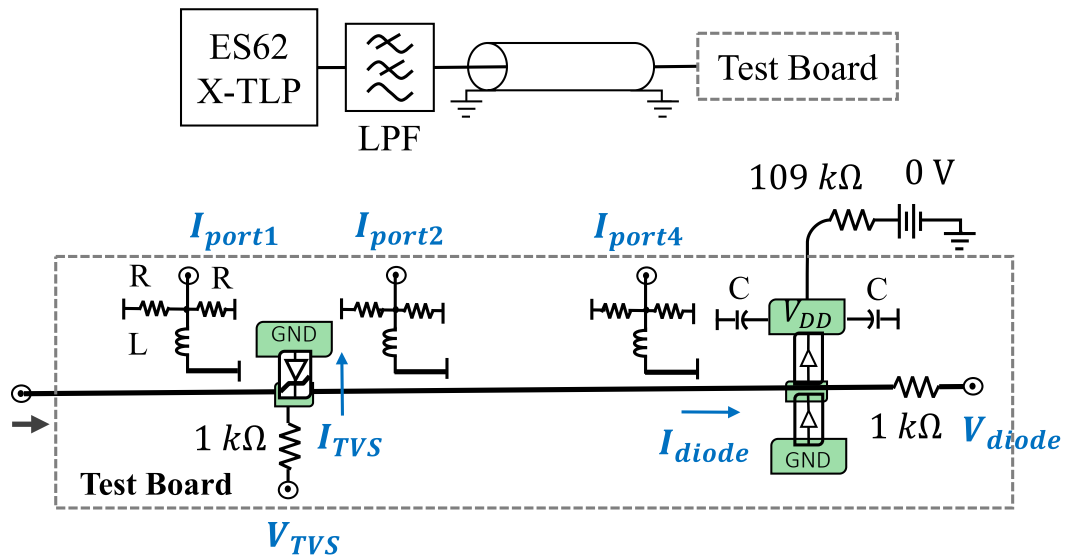

Figure 7. SEED test schematic.

Comparisons between the measured and simulated results when the PESD3V3Y1BSF TVS was used as the off-chip protection are shown in Figure 8. Results are shown for the quasi-static and peak values of the current and voltage at both the off-chip and on-chip devices for a 1 ns rise time. The simulated peak and quasistatic voltages and currents were within a maximum error of 20% and 15% of RMS error for each case. Figure 9 shows similar comparisons when the PESD1V2Y1BSF TVS was used as the off-chip protection. Similar to the first TVS, the overall prediction accuracy was within a maximum error of 20% and 12% of RMS error. Similar results were observed for the other three rise times tested.

Example transient responses for the PESD3V3Y1BSF and PESD1V2Y1BSF TVS devices are shown in the Figure 10 and Figure 11, respectively. The ringing of the on-chip diode voltage in the measurements is caused by multiple reflections between the TVS and on-chip diode once they turn on and appear as “shorts”. There is also some difference in the response after the TLP injection ends, because of a non-ideal behavior of the TLP which is not included in our model, though this difference is not critical and can be ignored. Overall, the proposed model did a good job of capturing and predicting the most important behaviors in this SEED simulation (i.e. peak voltage and current, and quasi-static voltage and current, for both TVS and on-chip diode).

It is noteworthy that no convergence issues or numerical oscillations were observed among all 1120 simulations performed here for the two devices, for different TLP levels and rise times, and for both device-level and system-level simulations.

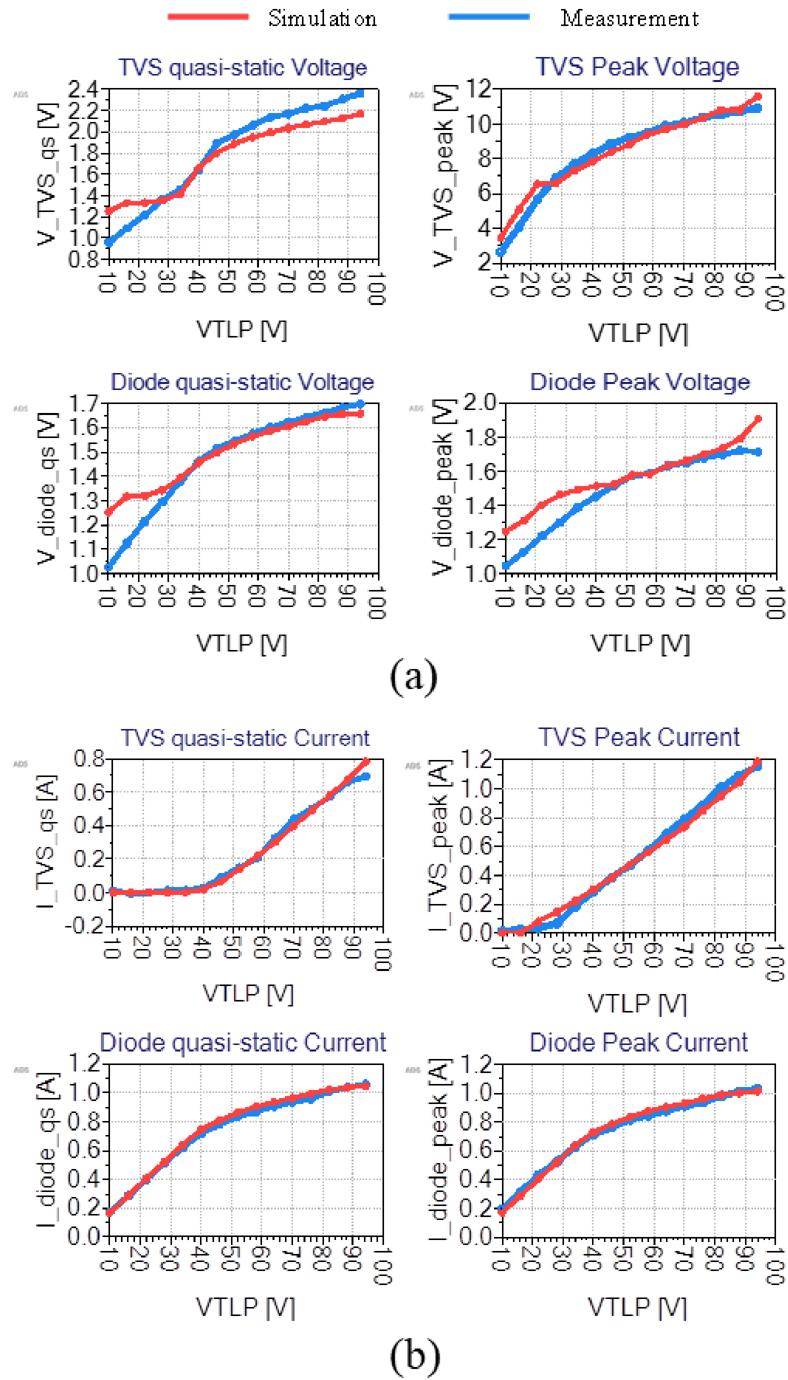

Figure 8. Measured and simulated SEED simulation results for the PESD3V3Y1BSF TVS device when using a 1 ns TLP rise time. Measurements are shown in blue and simulations in red. (a) Voltage across the off-chip TVS and on-chip diode. (b) Current through the off-chip TVS and on-chip diode.

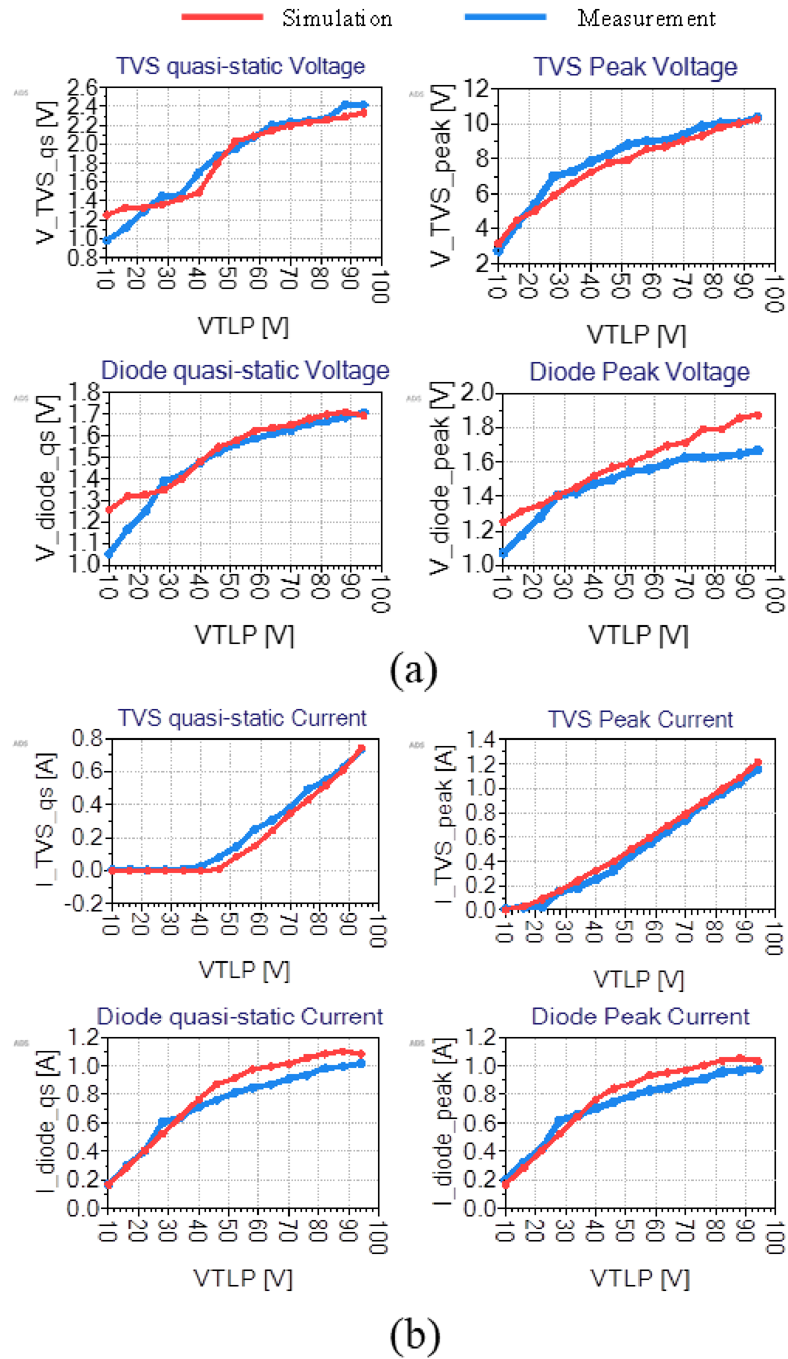

Figure 9. Measured and simulated SEED simulation results for the PESD1V2Y1BSF TVS device when using a 1 ns TLP rise time. Measurements are shown in blue and simulations in red. (a) Voltage across the off-chip TVS and on-chip diode. (b) Current through the off-chip TVS and on-chip diode.

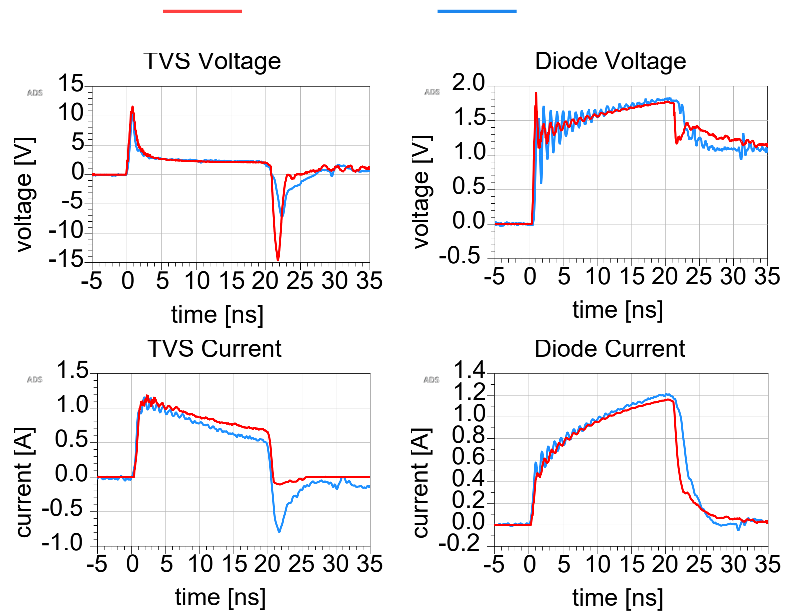

Figure 10. Simulated (red) and measured (blue) transient currents and voltages associated with components in the SEED simulation when using TVS device PESD3V3Y1BSF and a 1 ns TLP rise time.

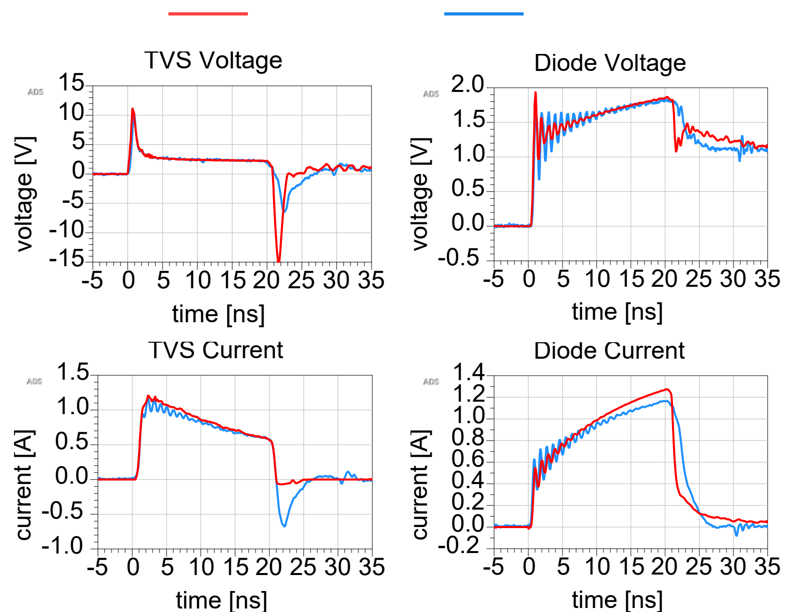

Figure 11. Simulated (red) and measured (blue) transient currents and voltages associated with components in the SEED simulation when using TVS device PESD1V2Y1BSF and a 1 ns TLP rise time.

5. MODEL TUNING

The proposed model was designed to be tuned using only measurements easily performed at the package level. For simplicity, some parameters were fixed to reasonable “known” values before tuning. These parameters are typical for most SCR type TVS diodes [21], so can be assumed to be known and do not need to be tuned during the normal tuning process. The well resistances R_{n-well} and R_{p-well} were fixed at 200 ohms. The junction capacitance was set to 0.1 pF. The junction capacitance cannot be set too large or dv/dt triggering caused by the well resistance and junction capacitance could cause the device to incorrectly turn on at low voltages. The forward and reverse gain of the NPN and PNP were set to 2 and 1, respectively. The forward gain could change the turn on behavior. A forward gain that is too high may result in an underestimated peak voltage, while a forward gain that is too low may result in the device failing to turn on at the desired breakdown voltage [5]. The damping factor was set to $\alpha = 0.9$, which was found to be a reasonable value to avoid numerical oscillations. While these parameter values worked well here and should be appropriate for many SCR type TVS diodes, users may find they need to be modified for other devices.

The other parameters were tuned one at a time based on measurements. The quasi-static IV curve should be tuned first. The reverse breakdown voltage of the ideal diode D_1 should next be tuned to match the holding voltage. Then, the parameter V_{BV} in (6) should be tuned to match with the breakdown voltage. The breakdown voltage of D_1, V_{BV}, and the initial voltage drop from the coupled NPN and PNP transistors together determine the breakdown voltage of the model, as:

$$V_{Breakdown} = V_{D1} + V_{BV} + V_{CE(sat)} + V_{EB(on)} \tag{19}$$

$V_{CE(sat)}$ is the voltage drop across the NPN and $V_{EB(on)}$ is the voltage between the emitter and the base of PNP. R_1 and R_4 are the series resistance in the device and determine the slope of the quasi-static IV curve after the holding voltage and current is reached.

Table 1. Parameters of the TVS diode models

PESD3V3Y1BSF		PESD1V2Y1BSF	
V_{BV}	4 V	V_{BV}	2 V
V_{D1}	0.7 V	V_{D1}	1 V
R_1, R_4	0.09 ohm	R_1, R_4	0.09 ohm
L_1	0.2 nH	L_1	0.6 nH
R_0	90 ohm	R_0	100 ohm
Q_0	1e-11	Q_0	5e-12
Other Parameters			
C_j		0.1 pF	
R_{n-well}, R_{p-well}		200 ohm	
β_F		2	
β_R		1	
τ		50e-9	
I_s		1e-15	
α (damping)		0.9	

After matching the quasistatic IV curve, the values of R_0 and Q_0 determining conductivity modulation should be tuned to match the voltage overshoot and the falling edge of the transient waveforms. The inductance L_1 also contributes to the voltage overshoot, but as the relationship between the TLP voltage versus overshoot are different for inductance and conductivity modulation [17], it is possible to get reasonable values for all three, L_1, R_0 and Q_0. To tune these values, a relatively slow rise time should be chosen (e.g., 1 ns or 2 ns), and the double peaks in the transient overshoot may be seen [17]. The first peak is caused by the conductivity modulation and the second peak is from the inductance. The R_0 and Q_0 are tuned for the first peak and L_1 is tuned for the second peak, respectively. Once initial values of parameters are tuned to roughly capture the behavior of the device, then parameters can be fine-tuned together or separately, as appropriate, to better capture results at different rise times.

The parameters of the TVS diode models used in this paper are listed in Table 1 as a reference.

6. CONCLUSIONS

In this paper, we proposed a simplified physics-based model for SCR-type snapback TVS devices. By reducing the number of components and parameters, the model can be relatively easily tuned using only measurements performed on the package device, without the need for detailed silicon-level information. Issues with convergence were studied to determine its root cause and were eliminated by adding a non-linear damping resistance in series with the PN junction capacitance of the junction responsible

for turn on. The damping resistance was set according to the simulation time step to ensure stability in a wide variety of simulation setups, though could also be set to a constant value if required for compatibility with a specific SPICE tool. By adding this damping resistance to the model, the model's stability could be assured without requiring additional intervention from the user. This feature is important as not all users may understand how to modify the SPICE tool setup to ensure stability or even recognize when a stability issue is present, as not all convergence issues are obvious. Device and system-level (SEED) simulations with two commercially available TVS devices were utilized to validate the model. Simulation results demonstrate matched measurements within about 20% for both quasistatic and transient results for each of the TLP conditions tested. No convergence issues or numerical oscillation were observed for all 1120 simulations of the two devices, the device- and system-level setups, and the various TLP levels and rise times. We found this physics-based model to be both easier to tune and more stable than previous behavioral models built for similar purposes [9] [15]. Overall, this model show promise as a tool for representing TVS devices in SEED simulations.

REFERENCES

[1] "White Paper 3: System level ESD—Part 1: Common misconceptions and recommended basic approaches," *Industry Council on ESD Target Levels*, Dec. 2010. [Online]. Available: https://www.esdindustrycouncil.org/ic/docs/Industry%20Council%20White%20Paper%203%20PI%20Rev1%20Dec%202010.pdf

[2] P. Wei, G. Maghlakelidze, A. Patnaik, H. Gossner and D. Pommerenke, "TVS Transient Behavior Characterization and SPICE Based Behavior Model," *2018 40th Electrical Overstress/Electrostatic Discharge Symposium (EOS/ESD)*, 2018, pp. 1-10.

[3] J. Di Sarro and E. Rosenbaum, "A Scalable SCR Compact Model for ESD Circuit Simulation," *2008 IEEE International Reliability Physics Symposium*, Phoenix, AZ, USA, 2008, pp. 254-261, doi: 10.1109/RELPHY.2008.4558895.

[4] J. P. Di Sarro and E. Rosenbaum, "A Scalable SCR Compact Model for ESD Circuit Simulation," in *IEEE Transactions on Electron Devices*, vol. 57, no. 12, pp. 3275-3286, Dec. 2010, doi: 10.1109/TED.2010.2081674.

[5] R. Mertens and E. Rosenbaum, "A Physics-based Compact Model for SCR Devices Used in ESD Protection Circuits," *2013 IEEE International Reliability Physics Symposium (IRPS), Monterey*, CA, USA, 2013, pp. 2B.2.1-2B.2.7, doi: 10.1109/IRPS.2013.6531947.

[6] N. Monnereau, F. Caignet, N. Nolhier, D. Trémouilles and M. Bafleur, "Behavioral-modeling Methodology to Predict Electrostatic-Discharge Susceptibility Failures at System Level: An IBIS Improvement," *10th International Symposium on Electromagnetic Compatibility*, York, UK, 2011, pp. 457-463.

[7] L. Wei, C. E. Gill, W. Li, R. Wang and M. Zunino, "A Convergence Robust Method to Model Snapback for ESD Simulation," *CAS 2011 Proceedings (2011 International Semiconductor Conference)*, Sinaia, Romania, 2011, pp. 369-372.

[8] F. Caignet, N. Monnereau, N. Nolhier and M. Bafleur, "Behavioral ESD Protection Modeling to Perform System Level ESD Efficient Design," *2012 Asia-Pacific Symposium on Electromagnetic Compatibility*, Singapore, 2012, pp. 401-404, doi: 10.1109/APEMC.2012.6238002.

[9] J. Zhou, Y. Xu, S. Bub, S. Holland, J. Meiguni, D. Pommerenke, D. Beetner, "Transient Response of ESD Protection Devices for a High-Speed I/O Interface," in *IEEE Transactions on Electromagnetic Compatibility*, vol. 64, no. 4, pp. 907-14, 2022.

[10] L. Shen, Y. Xu, S. Holland, S. Bub, D. Pommerenke, D. Beetner, "Application of TVS Models for SEED Simulation of a Variety of TVS Devices," *Asia-Pacific EMC Symposium*, 2023.

[11] Y. Li, Y. Wang and Y. Wang, "Modeling IC Snapback Characteristics Using a VCCS Model for Circuit-Level ESD Simulation," *2019 IEEE 26th International Symposium on Physical and Failure Analysis of Integrated Circuits (IPFA)*, Hangzhou, China, 2019, pp. 1-3, doi: 10.1109/IPFA47161.2019.8984808.

[12] J. Xiong, Z. Chen, Y. Xiu, Z. Mu, M. Raginsky and E. Rosenbaum, "Enhanced IC Modeling Methodology for System-level ESD Simulation," *2018 40th Electrical Overstress/Electrostatic Discharge Symposium (EOS/ESD)*, Reno, NV, USA, 2018, pp. 1-10.

[13] W. Liang, X. Yang, A. Loiseau, S. Mitra and R. Gauthier, "Novel ESD Compact Modeling Methodology Using Machine Learning Techniques," *2020 42nd Annual EOS/ESD Symposium (EOS/ESD)*, Reno, NV, USA, 2020, pp. 1-7.

[14] W. Liang, X. Yang, M. Miao, A. Loiseau, S. Mitra and R. Gauthier, "Novel ESD Compact Modeling Methodology Using Machine Learning Techniques for Snapback and Non-Snapback ESD Devices," in *IEEE Transactions on Device and Materials Reliability*, vol. 21, no. 4, pp. 455-464, Dec. 2021, doi: 10.1109/TDMR.2021.3116599.

[15] Y. Xu, J. Zhou, S. Bub, S. Holland, J. Meiguni, D. Pommerenke, D. Beetner, "Improved SEED Modeling of an ESD Discharge to a USB Cable," in *IEEE Transactions on Electromagnetic Compatibility*, vol. 65, no. 3, 2023.

[16] K. J. Tseng and S. Pan, "Modified charge-control equation for more realistic simulation of power diode characteristics," *Proceedings of Power Conversion Conference - PCC '97*, Nagaoka, Japan, 1997, pp. 439-444 vol.1, doi: 10.1109/PCCON.1997.645651.

[17] G. Notermans, H. Ritter, S. Holland and D. Pogany, "Dynamic Voltage Overshoot During Triggering of an SCR-Type ESD Protection," in *IEEE Transactions on Device and Materials Reliability*, vol. 19, no. 4, pp. 583-590, Dec. 2019, doi: 10.1109/TDMR.2019.2952713.

[18] F. L. Alvarado, R. H. Lasseter and J. J. Sanchez, "Testing of Trapezoidal Integration with Damping for the Solution of Power Transient Problems," in *IEEE Transactions on Power Apparatus and Systems*, vol. PAS-102, no. 12, pp. 3783-3790, Dec. 1983.

[19] *PESD3V3Y1BSF*, Nexperia. [Online]. Available: https://www.nexperia.com/products/esd-protection-tvs-filtering-and-signal-conditioning/esd-protection/low-capacitance-esd-protection-for-high-speed-interfaces/PESD3V3Y1BSF.html

[20] *PESD1V2Y1BSF*, Nexperia. [Online]. Available: https://www.nexperia.com/products/esd-protection-tvs-filtering-and-signal-conditioning/esd-protection/low-capacitance-esd-protection-for-high-speed-interfaces/PESD1V2Y1BSF.html

[21] R. Mertens, "A Compact Model for Silicon Controlled Rectifiers in Low Voltage CMOS Processes." M.S. thesis, Dept. Elect. Comput. Eng., University of Illinois at Urbana-Champaign, 2014.

II. MICROWAVE HOLOGRAPHY FOR EMI SOURCE IMAGING

Xin Yan, Jiangshuai Li, Wei Zhang, Kaustav Ghosh, Philippe Sochoux, Daryl Beetner, and Victor Khilkevich

ABSTRACT

Emission source microscopy technique can be utilized to localize the radiation sources in complex and electrically large electronic systems. In the 2-D emission source microscopy algorithm both magnitude and phase of the field need to be measured, and a vector network analyzer or an oscilloscope have to be used as a receiver, resulting in reduced signal-to-noise ratio and longer measurement time compared to a spectrum analyzer. In this paper, a phaseless EMI source imaging method is proposed based on microwave holography. The field produced by the device under test is not measured directly, instead, the interference pattern between the emitted field and the reference wave is created and measured as the hologram. The hologram is a real-valued function that can be measured using a spectrum analyzer. The proposed method is validated through measurements for both passive and active devices. The proposed algorithm is efficient and reliable in identifying major radiation sources and determining their location and relative strength.

Keywords: Emission source microscopy, radiation sources, microwave holography, source imaging

1. INTRODUCTION

With increase of the operating data rate in electronic devices electromagnetic interference (EMI) issues are becoming more critical for complex and large systems. For instance, the optical modules used in network equipment could cause EMI problems at frequencies up to tens of GHz [1]. To identify the radiating sources of the EMI that contribute to the far-field region, the emission source microscopy (ESM) technique could be used by measuring the field over a plane at an electrically large distance from the device under test (DUT) and back-propagating the field onto the DUT plane.

In previous works, the 2D ESM algorithm was derived [2][3]. The uniformly distributed scanning points are picked on the scan plane with the separation between the points less than $\lambda/2$ in order to satisfy the Nyquist spatial sampling criterion. In [4], the sparse emission source microscopy was proposed to minimize the number of required spatial samples. Another sparse ESM scan using Gaussian process regression was proposed in [5]. In [6], the effects on image quality of different scanning point selection methods were analyzed.

The ESM algorithm has been analyzed and optimized by researchers, however, the method requires to measure both the magnitude and phase of the field and a vector network analyzer (VNA) or an oscilloscope have to be used as a receiver, resulting in a relatively low signal-to-noise ratio and long measurement time (due to a relatively slow sweep of the VNAs and a large amount of the data needed to be collected in the time-domain measurement to achieve high frequency resolution). These deficiencies of the

traditional 2D ESM algorithm have significant impact on the applicability of the method in cases of weak radiation sources.

Holography is an imaging technique used to reconstruct the object wavefront (i.e. the wavefront scattered or produced by the object) from the recording of an interference pattern created by an object beam and a reference beam. This technique was originally introduced by Gabor to increase the resolution of electron microscopes [7] and later extended to the microwave field [8]. The interference pattern, known as the hologram, is a real-valued function, which can be measured by a spectrum analyzer (SA), alleviating the deficiencies of the traditional imaging technique outlined above. An example of the phaseless antenna diagnostics based on the microwave holography was presented in [9].

In this paper, we propose a phaseless EMI source imaging method based on microwave holography, which is an alternative solution for localization and characterization of active radiation sources. The hologram is created by combining the field from the scan antenna with a reference signal collected by the second antenna placed near the DUT and naturally producing a much stronger signal than the scan antenna. The normalized hologram is backpropagated to the source plane and the image of sources is obtained. The proposed method is validated through measurements in which the radiation sources are visualized and localized successfully.

The paper is organized as follows. Section 2 presents the analytical formulation of the microwave holography imaging methodology. The measurement setup and results are demonstrated in Section 3, and conclusions in Section 4.

2. MICROWAVE HOLOGRAPHY IMAGING ALGORITHM

2.1. 2D ESM ALGORITHM

The 2D ESM algorithm is based on the synthetic aperture radar (SAR) technique, and a typical implementation of the method is illustrated by Figure 1. The electric field on a plane with elevation 0 can be represented as a superposition of plane waves in the form of the Fourier transform [3]:

$$E(x, y, 0) = \frac{1}{4\pi^2} \int_{-\infty}^{\infty} \int_{-\infty}^{\infty} f(k_x, k_y) e^{-j(k_x x + k_y y)} dk_x dk_y \tag{1}$$

where $f(k_x, k_y)$ is spectrum of the field distribution, and k_x and k_y are the spatial frequencies in the x and y directions, respectively. The spectrum of the field on any plane (x, y, z_0) parallel to $(x, y, 0)$ can be found as:

$$f\left(k_x, k_y, z_0\right) = f\left(k_x, k_y\right) \cdot e^{-jk_z z_0} \tag{2}$$

where

$$k_z = \sqrt{k^2 - k_x^2 - k_y^2}, \qquad \text{if } k_x^2 + k_y^2 \leq k^2, \tag{3a}$$

$$k_z = -j\sqrt{k_x^2 + k_y^2 - k^2}, \qquad \text{otherwise.} \tag{3b}$$

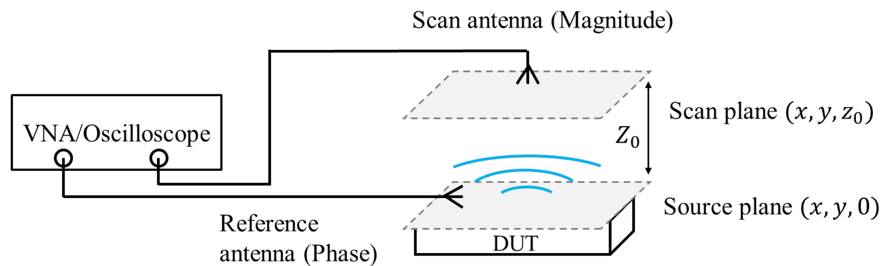

Figure 1. 2D ESM setup.

In (3) k is the wavenumber, and k_z is the z component of the propagation vector. Real k_z corresponds to propagating components of the spectrum, while the imaginary values give the evanescent waves. Formulas (1), (2) can be used to transform the field between any parallel planes. For example, if the field on the scanning plane (x, y, z_0) is known, the field on the DUT plane $(x, y, 0)$ can be backpropagated as

$$E(x, y, 0) = \mathcal{F}^{-1}(\mathcal{F}[E(x, y, z_0)]e^{jk_z z_0}) \quad (4)$$

where $\mathcal{F}$ and $\mathcal{F}^{-1}$ are the forward and inverse Fourier operators, respectively. Equation (4) serves as the basis of the 2-D ESM algorithm.

2.2. HOLOGRAM FORMATION AND RECONSTRUCTION

In the field of optics and electron microscopy, it is impossible to measure the phase of the signal directly. The hologram provides a way to record and reproduce the field information by including the phase information as the magnitude variation of the interference pattern. Here we explain the hologram formation and image reconstruction using in-line holography as an example. The diagram of the in-line holography is shown in Figure 2 [10].

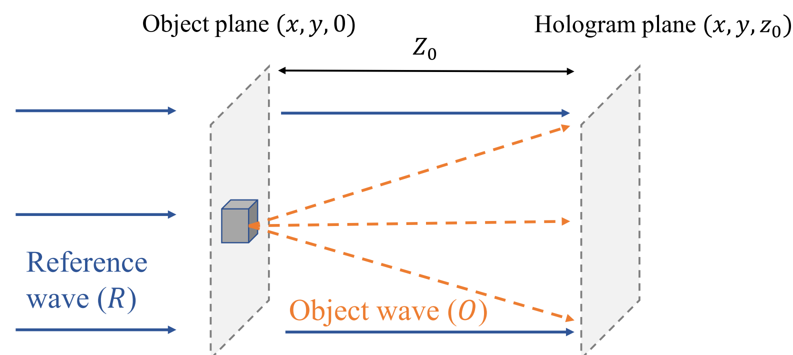

Figure 2. In-line holography diagram.

Consider a plane wave R passing by an object located on the plane $(x, y, 0)$. Part of the wave is scattered by the object, which creates the object wave O. The two waves interfere beyond the object and the power of the interference pattern $U = R + O$ is recorded at some distance z_0, i.e at the hologram plane (x, y, z_0). The recorded hologram $H(x, y, z_0)$ therefore is given by:

$$\begin{gathered} H(x,y,z_0) = |U(x,y,z_0)|^2 = |R(x,y,z_0)|^2 \\ +|O(x,y,z_0)|^2 + R^*(x,y,z_0)O(x,y,z_0) \\ +O^*(x,y,z_0)R(x,y,z_0) \end{gathered} \tag{5}$$

where $|R(x, y, z_0)|^2$ is the power of the reference wave, and $|O(x, y, z_0)|^2$ is the power of the scattered wave. The last two terms are the interference pattern observed in the hologram. For successful imaging it is required that the power of the reference wave is much larger than the power of the object wave, i.e. $|R|^2 \gg |O|^2$. Under this condition the hologram is approximated as:

$$\begin{gathered} H(x,y,z_0) \approx |R(x,y,z_0)|^2 + R^*(x,y,z_0)O(x,y,z_0) \\ +O^*(x,y,z_0)R(x,y,z_0) \end{gathered} \tag{6}$$

Before generating the image, the hologram is normalized as:

$$\begin{gathered} H_0(x,y,z_0) = \frac{H(x,y,z_0)}{|R(x,y,z_0)|^2} - 1 \approx \\ \frac{R^*(x,y,z_0)O(x,y,z_0)}{|R(x,y,z_0)|^2} + \frac{O^*(x,y,z_0)R(x,y,z_0)}{|R(x,y,z_0)|^2} \end{gathered} \tag{7}$$

The normalized hologram is then backpropagated to produce the normalized image on the source/object plane using the same transformation as in (4):

$$I_0(x,y,0) = \mathcal{F}^{-1}(\mathcal{F}[H_0(x,y,z_0)]e^{jk_z z_0}) \tag{8}$$

The intensity of the image I_0 is given relative to the intensity of the reference wave $R(x, y, z_0)$. To obtain the absolute values of the image intensity, the normalized image needs to be multiplied by $|R(x, y, z_0)|$.

2.3. TWIN OBJECT EFFECT

As the 2D ESM algorithm uses both the magnitude and phase of the scanned field, the resulting image is free of any artifacts other than those related to limited scan area (aperture diffraction) and sampling (aliasing). In holography, however, the interference pattern $R^*O + O^*R$ is recorded, where the component proportional to O would produce the actual image of the object, and the component O^* which is due to the imaginary object located on the opposite side of the hologram plane and emitting waves in the opposite direction relative to the actual object (the complex conjugate in O^* reverses the propagation direction of all waves in the plane wave spectrum) would produce the twin image. The image of the twin object is always presented in holography and is especially detrimental for in-line measurement as in Figure 2. However, the effect of the twin object is mitigated as the distance between the actual object and the hologram plane is increased. A diagram of the twin object effect is shown in Figure 3. The image at the object plane includes the focused image of the real object and the unfocused image of the twin object, which can be considered as noise added to the image.

To analyze the image quality, a hologram of a short dipole is calculated numerically. The frequency is set to 5 GHz, and the distance between the source and hologram planes is 0.5 m. The electric field generated by the dipole is calculated on a

2 m × 2 m hologram plane and a large (compared to the field values) constant is added to the field distribution to form the hologram.

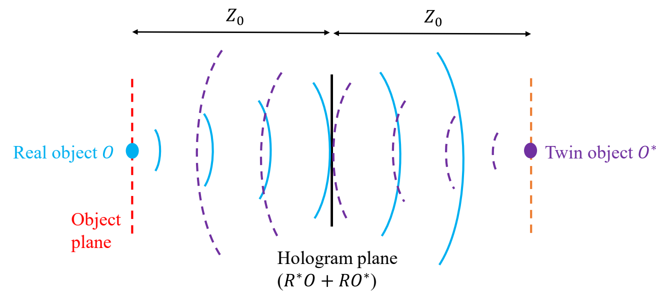

Figure 3. A diagram of the twin object effect.

The simulation results are shown in Figure 4. The object and reference waves at the hologram plane (at z=0.5 m) are shown in Figure 4 (a) and (b) respectively. The image in Figure 4 (c) represents the hologram. As can be seen, the hologram pattern has small variations of the magnitude relative to the value of the reference wave (less than 0.2 dB). The image at z = 0 m produced from the hologram is shown in Figure 4 (d). The point source is visualized and localized successfully. For comparison Figure 4 (e) and (f) show the images from the real and twin object at the source plane, respectively. The holography image in Figure 4 (d) is a summation of the actual object (Figure 4 (e)) and twin object (Figure (f)) images. As can be seen, the twin object significantly increases the amount of the background noise, but since the twin object is out of focus, the peak value of its image is more than 25 dB lower than the peak of the actual object image, which is sufficient for many practical applications. It is noticed that the twin object effect is influenced by the distance between the source plane and hologram plane. When the backpropagation distance is small, the twin image may be strong enough to cause

considerable degradation of the object image, however a proper selection of the distance between the object and hologram plane allows to decrease the contribution of the twin object to an acceptable level in many cases.

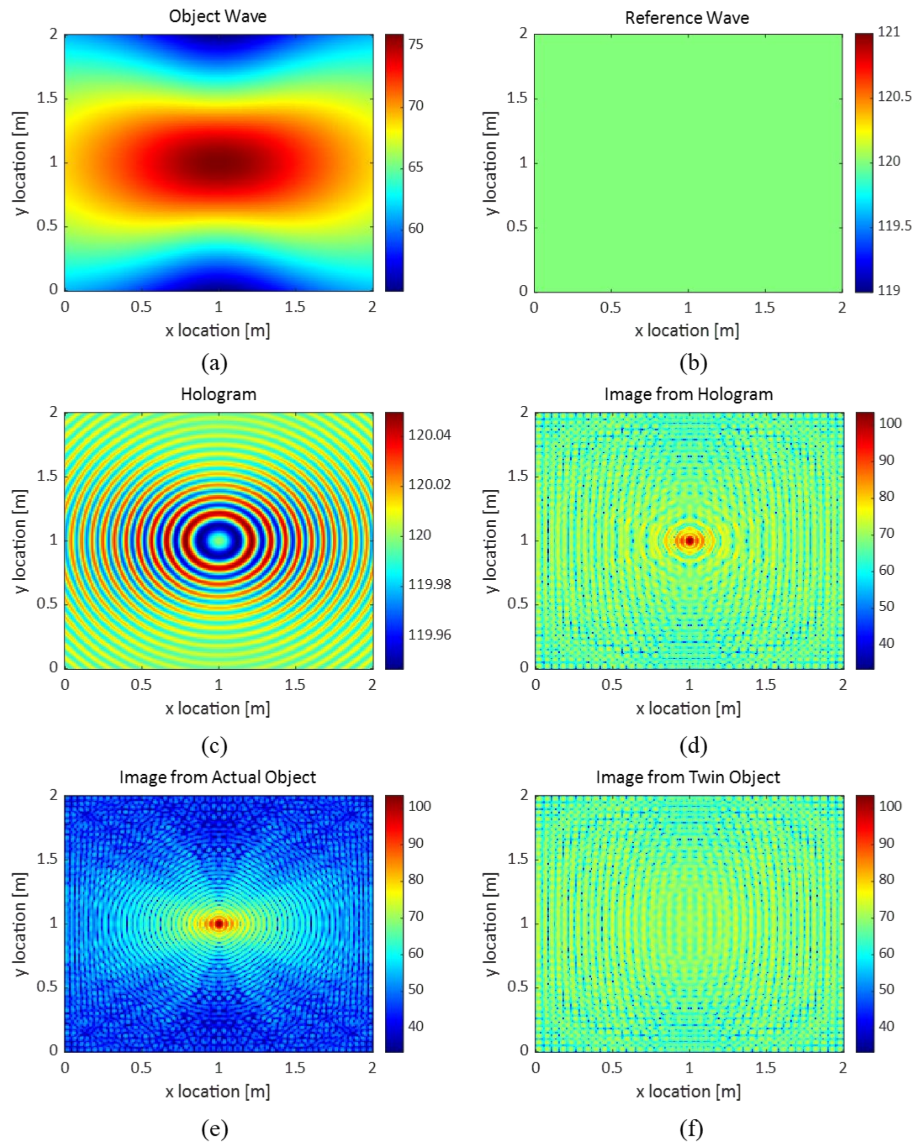

Figure 4. Simulated imaging of a point source. The color scale represents the values in dB relative to 1 V/m. (a) Object wave at the hologram plane. (b) Reference wave at the hologram plane. (c) Hologram. (d) Image backpropagated from the hologram. (e) Image from the actual object only (ESM). (f) Image from the twin object only.

2.4. MICROWAVE HOLOGRAPHY IMAGING ALGORITHM

Optical holography is almost always performed by creating a physical reference wave using a laser source. A similar approach can be used at microwave frequencies if the object is illuminated by a wave produced by a generator loaded by an antenna. However, a more practical approach is to use a synthetic reference wave created by combining the signals from the reference generator and the scanning antenna [9]. The diagrams of the corresponding setup are shown in Figure 5. In a passive DUT measurement, the reference signal could be obtained directly from the source (Figure 5 (a)). A more general setup uses a reference antenna configuration, which is suitable for both passive and active DUT measurement, as shown in Figure 5 (b). The reference signal needs to be coherent with the scan signal (i.e. originate from the same source) and its amplitude must be much larger than the amplitude of the scan signal. The combined signal (hologram) is measured by a spectrum analyzer, or even by a much simpler device, for instance, a power meter [9].

In summary, the proposed method consists of the following steps:

i. Setup the scan antenna and reference signal. Make sure the reference signal is much stronger than the scan signal.

ii. Measure the field on a 2D plane to obtain $H(x, y, z_0)$.

iii. Measure or estimate the reference signal $|R(x, y, z_0)|$. The mean value of the hologram amplitude is used in this paper as an approximation (the oscillating functions O and O^* in (6) have approximately zero mean values, therefore $\langle H \rangle \approx |R|^2$).

iv. Calculate normalized hologram $H_0(x, y, z_0)$ according to (7).

v. Back propagate to the source plane according to (8). Multiply with the reference plane amplitude $|R(x, y, z_0)|$, to obtain the absolute values of the EMI source image if needed.

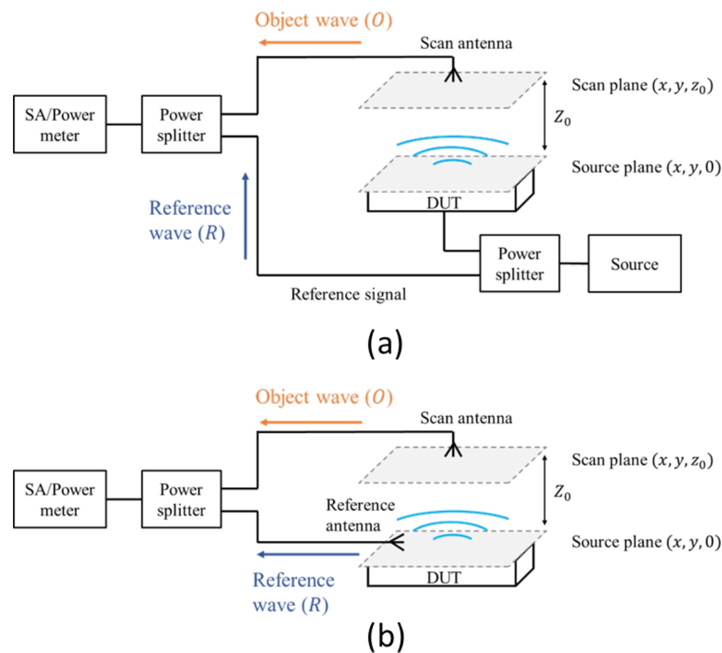

Figure 5. Microwave holography imaging setup. The scan and reference signals can be understood as object and reference waves respectively. (a) Imaging of passive DUTs. (b) Imaging of passive or active DUTs.

The condition for successful imaging is that the reference wave is significantly stronger than the object wave ($|R|^2 \gg |O|^2$). In practice, to ensure that this condition is met, the scan antenna is first connected to the receiver, and a quick manual scan is performed above the DUT at roughly the hologram plane to determine the maximum scan signal level. Afterwards, the scan antenna is replaced by the reference antenna which is placed close to the DUT at a location where the reference signal is significantly stronger

than the scan signal (the amplitude of which was estimated earlier). Based on the conducted experiments we observed that a difference of around 10 dB is enough to achieve acceptable image quality.

As has been said above, a larger distance between the source and hologram planes could help reducing the twin image effect, at the same time, increasing this distance reduces the signal-to-noise ratio of the normalized hologram (7). Another detrimental effect of increasing the distance to the scan plane (while maintaining the size of the scan area) is the decrease of the image resolution (see equation (7) in [3]).

The scan step size should be smaller than $\lambda/2$ according to the Nyquist criterion [6].

3. MEASUREMENT VALIDATION

3.1. PASSIVE DUT – ANTENNA SOURCE

The proposed algorithm is validated first on a passive DUT. The measurement setup is shown in Figure 6. A horn antenna is placed at the bottom and excited by a VNA at 26 GHz. The scan antenna is fixed on the arm of the scanner driven by two motors. The distance between the scan and the source antennas is about 70 cm. The scan area is set to 40 cm × 40 cm, and the step size is 4 mm. To form the hologram, a near-field probe is placed close to the source antenna to obtain the reference signal. A power splitter is used to combine the scan and reference signals. The combined signal is measured by the spectrum analyzer.

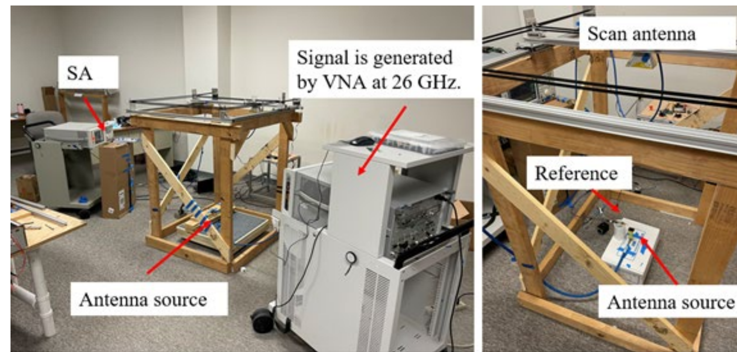

(a)

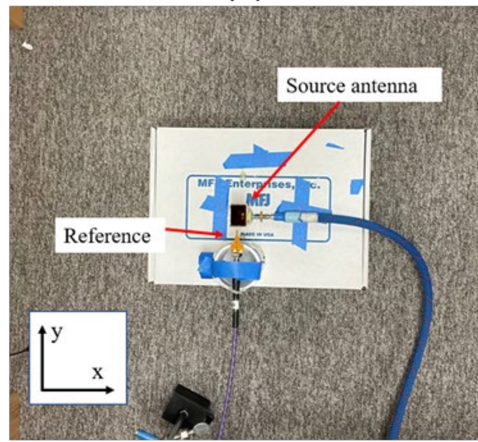

(b)

Figure 6. Horn antenna imaging (a) Measurement setup. (b) Top view to the scan area.

The measurement results are shown in Figure 7. Figure 7 (a) demonstrates the raw data obtained from the SA. As the reference signal is much stronger than the scan signal, the hologram amplitude variations are small – less than 2 dB in this case. Since the interference pattern in the hologram has small variations, the stability of the measurement instrument may compromise the quality of the hologram. For example, a horizonal line in the hologram pattern which can be seen in Figure 7 (a) at y=0.27 m is the result of a sudden change (of about 0.3 dB) in the output of the SA (probably due to the SA self-calibration). However, since the information about the source is distributed over the

entire area of the hologram, local defects in the hologram usually do not cause a noticeable degradation of the image quality. Figure 7 (b) shows the normalized hologram and (c) is the image at the source plane backpropagated and reconstructed from the normalized hologram. The peak in the center of the image represents the source antenna location. The noise in the image is mainly from the twin object effect and the diffraction of the waves on a relatively small scan aperture. Even so, the noise level is approximately 10 dB lower than the image peak. Overall, the algorithm is validated on the passive DUT and the radiation source is visualized and localized successfully.

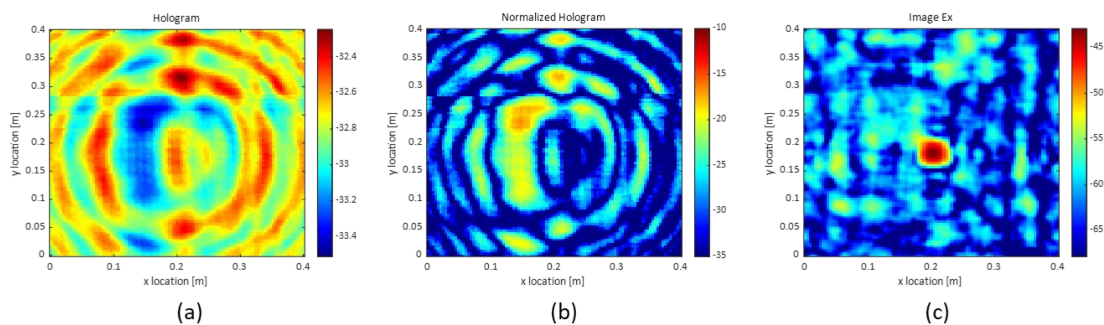

Figure 7. Horn antenna imaging results (a) Hologram (raw data). (b) Normalized hologram. (c) Ex Image at the source plane. Color scale in dB (arbitrary unit).

3.2. ACTIVE DUT – COMMERCIAL ROUTER

In this section holographic imaging is applied to an active DUT, a commercial network router, as shown in Figure 8. The router has 32 ports for 100 Gbps optical modules, and 4 ports for 400 Gbps optical modules. Only one of the 100 Gbps port is activated in the loopback mode to create the radiation source. The measurement frequency was set to 25.78 GHz which corresponds to the peak of the module emissions.

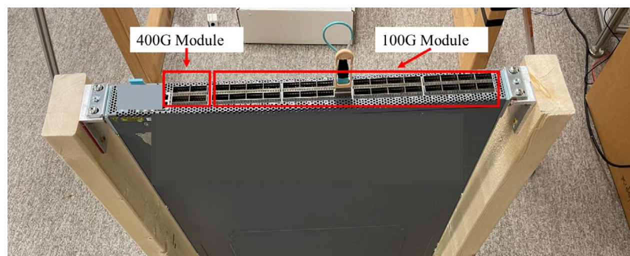

Figure 8. The commercial router.

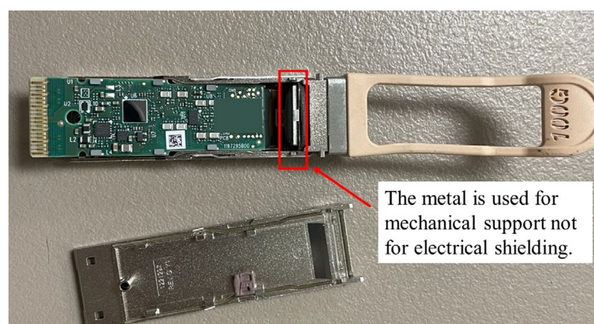

Figure 9. Interior of an optical module.

When the optical module is plugged to the connector, the gaps between the module and the cage could be a potential radiation source. Also, a lack of electrical shielding at the front side of the module (Figure 9) leads to the radiation from the module itself. To identify the radiation sources, 3 different cases are measured, as shown in Figure 10. The setup in Figure 10 (a) is the reference case, where one of the 100 Gbps port is activated, and adjacent groups of ports are covered by copper tape. Other ports are blocked by inactive electrical loopback modules. In Figure 10 (b), the gaps between the module and cage are additionally covered by copper tape. And finally in the setup in Figure 10 (c) the entire module is shielded by copper tape. The radiation level in case 3 is expected to be the lowest.

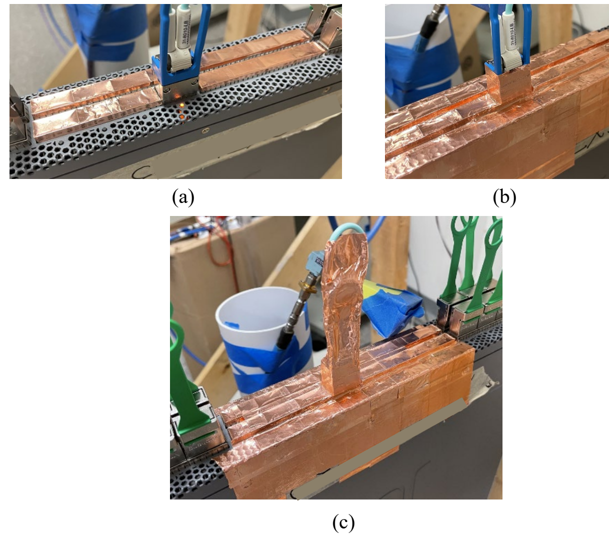

Figure 10. Internet router imaging. (a) Case 1: reference. One of the 100G port is activated and adjacent ports are covered by copper tape. (b) Case 2: The gap between the module and the cage is shielded. (c) Case 3: The gap and the module are shielded.

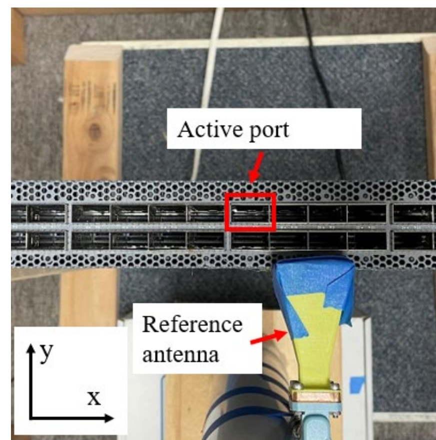

Figure 11. Top view to the scan area. The ports adjacent to the active one are covered by copper tape in reality.

The scan area is shown in Figure 11. A horn antenna is placed close to the active port and serves as the source of the reference signal. The distance between the face panel

of the router and scan area is about 18 cm. The scan area is 21 cm × 21 cm, scanned with a 3 mm step. High frequency amplifiers are utilized for both scan and reference signals. Since router power-cycling or module re-insertion changes the field patterns and the EMI levels, the measurements were conducted one after another without power-cycling or module re-insertion.

The measurement results for case 1, 2 and 3 are shown in Figures 12, 13 and 14, respectively. Both E_x and E_y components are measured and the images for both of them are created. The total tangential (to the scan plane) field is calculated as $E_{tan} = \sqrt{|E_x|^2 + |E_y|^2}$ where E_x and E_y are the component images. The radiation powers for all 3 cases are calculated, by integrating the E field over the scan area:

$$P_{rad} = \int_S |E_{tan}|^2 ds \tag{9}$$

It should be noted that since the scan aperture does not represent a closed surface around the DUT, the radiated power calculated this way is not equal to the total radiated power produced by the DUT and represents only a portion of it propagating through the scan aperture.

In case 1, the holograms are formed successfully, and the images show that the EMI hot spot surrounds the active port with no radiations seen above the other ports. The background noise for both E_x and E_y is 10 dB lower than the peaks. The maximum value of the EMI (E_{tan}) of case 1 is -84 dB and the P_{rad} is -113.2 dB (both values are given in arbitrary units since the antenna factor, cable loss, and the amplifier gain were not compensated).

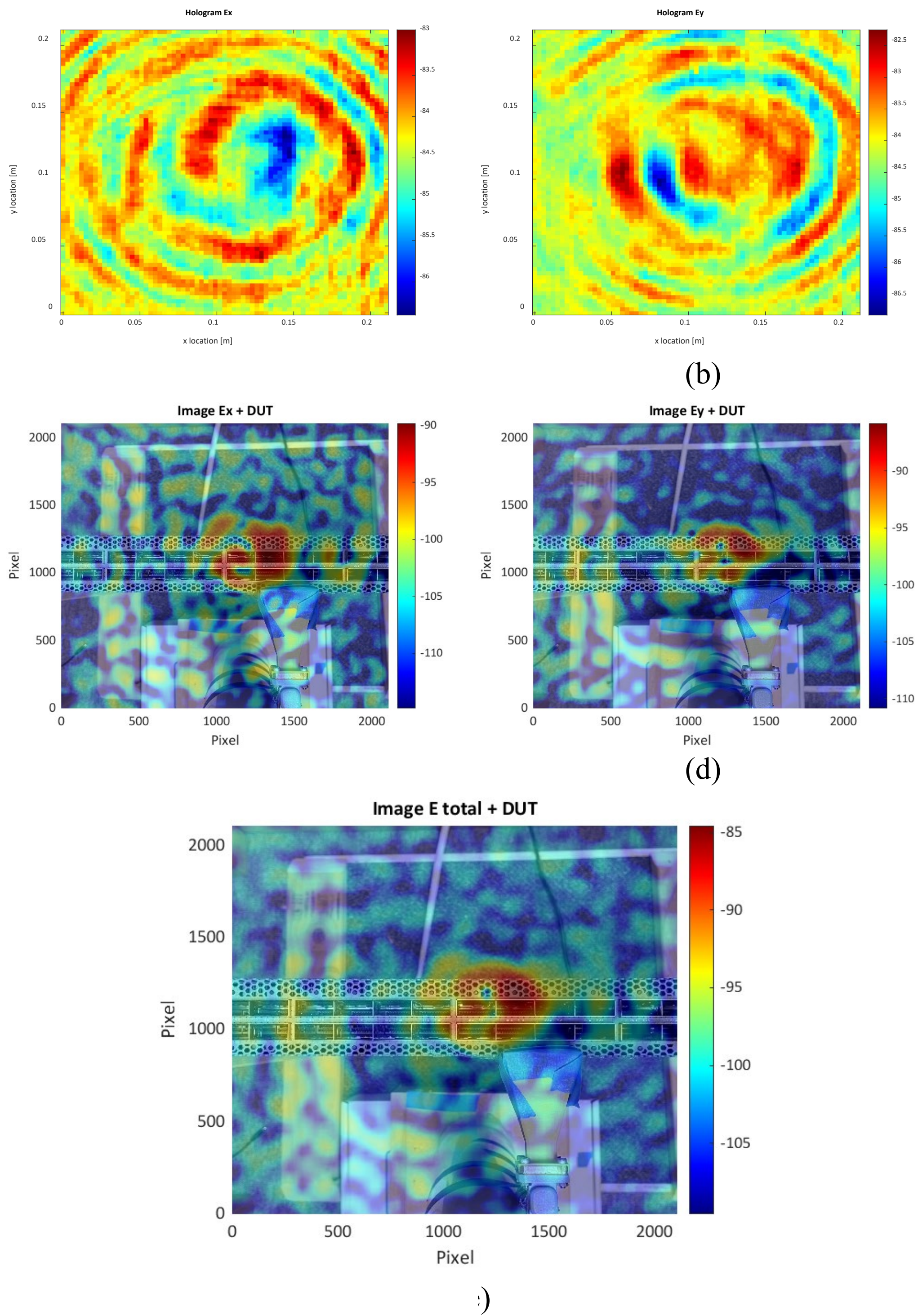

Figure 12. Measurement results of case 1. (a) Hologram of E_x. (b) Hologram of E_y. (c) Image of E_x. (d) Image of E_y. (e) Image of E tangential. Color scale in dB (arbitrary unit).

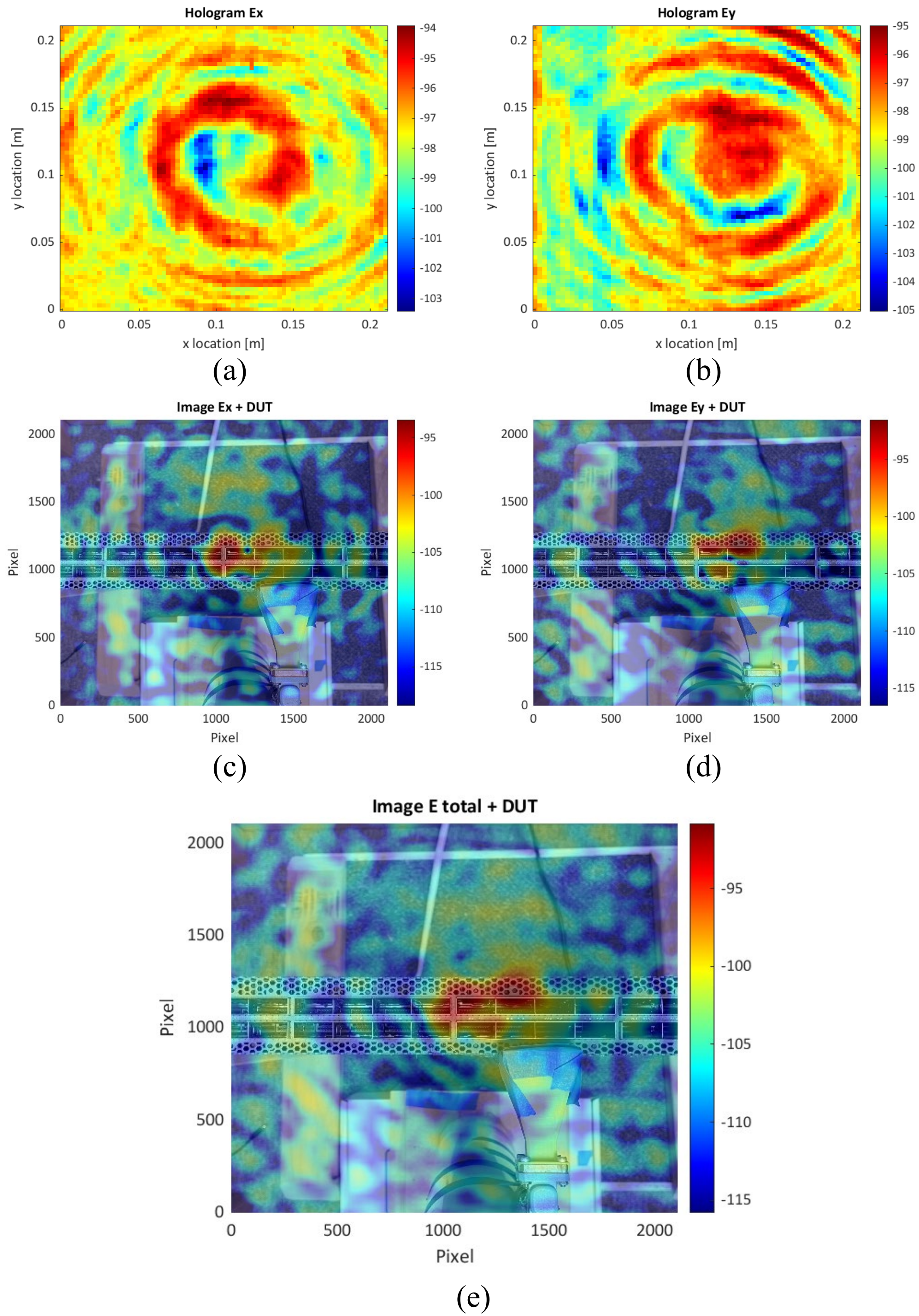

Figure 13. Measurement results of case 2. (a) Hologram of E_x. (b) Hologram of E_y. (c) Image of E_x. (d) Image of E_y. (e) Image of E tangential. Color scale in dB (arbitrary unit).

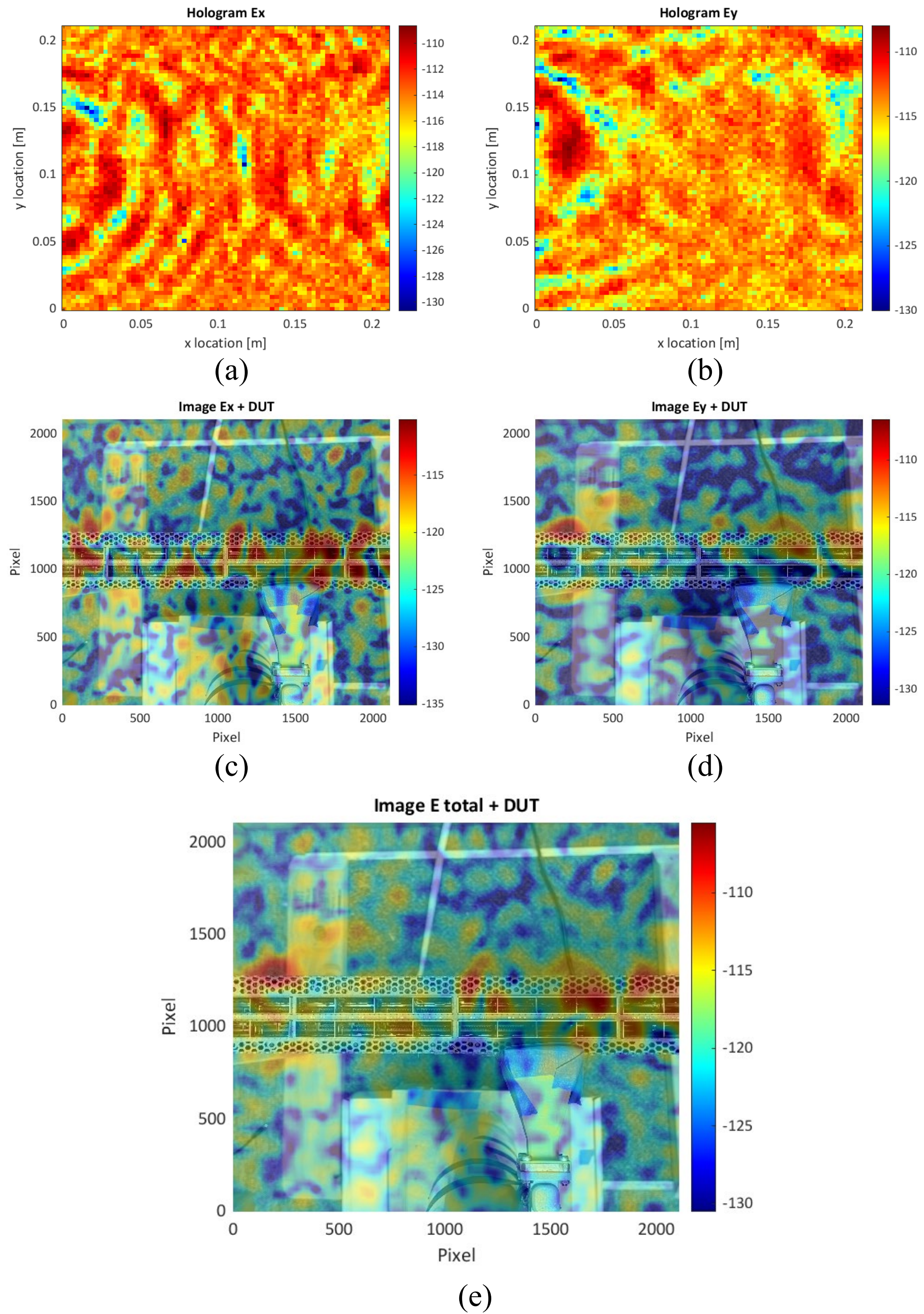

Figure 14. Measurement results of case 3. (a) Hologram of E_x. (b) Hologram of E_y. (c) Image of E_x. (d) Image of E_y. (e) Image of E tangential. Color scale in dB (arbitrary unit).

In case 2, as shown in Figure 13, the maximum value of the EMI is reduced compared with the reference case, which points to the gap between the module and the cage as the source of radiation. However, the hot spots for both E_x and E_y are still near the module, which indicates that the shielding did not suppress the source completely. The maximum value of the EMI for case 2 is -91.9 dB, and the P_{rad} is -121.9 dB. 7.9 dB reduction of E field and 8.7 dB reduction of P_{rad} are achieved by covering the gap between the module and the cage.

In case 3, as shown in Figure 14, after covering the top of the module, the holograms become very noisy. This happened because the amplitude of the reference signal is close to the noise floor of the SA, and the signal from the scan antenna even falls below the noise floor. However, despite this, the images are still reasonably clean and allow to detect the residual EM leakage which happens along the front panel of the router. The maximum EMI in this case is about -105.6 dB and the P_{rad} is about -131.6 dB. A summary of the measurement results for 3 cases are shown in Table 1. As can be seen, after the entire module is shielded by copper tape (case 3), 21.6 dB reduction of E field and 18.4 dB of P_{rad} are achieved compared with the reference case. The measurement results indicate that the gap between the module and cage and the top of the module are the main radiation sources. In conclusion, the measurement results demonstrate that the proposed algorithm is reliable in identifying major radiation sources and determining their location and relative strength.

To demonstrate the reliability of the holographic imaging, the images obtained holographically and by ESM imaging (with the VNA as the receiver) are shown in Figure 15. Since router power-cycling or module re-insertion changes the field patterns and the

EMI levels, the measurements were conducted immediately one after another without any change in the setup. As can be seen, the patterns and the amplitudes of the radiated sources given by the ESM and holography are very close. The accuracy of the radiated power measurement for the ESM imagining was investigated before in [3] and [4]. The maximum electric field values and the total radiated power for both measurements were calculated and are given in Table 2.

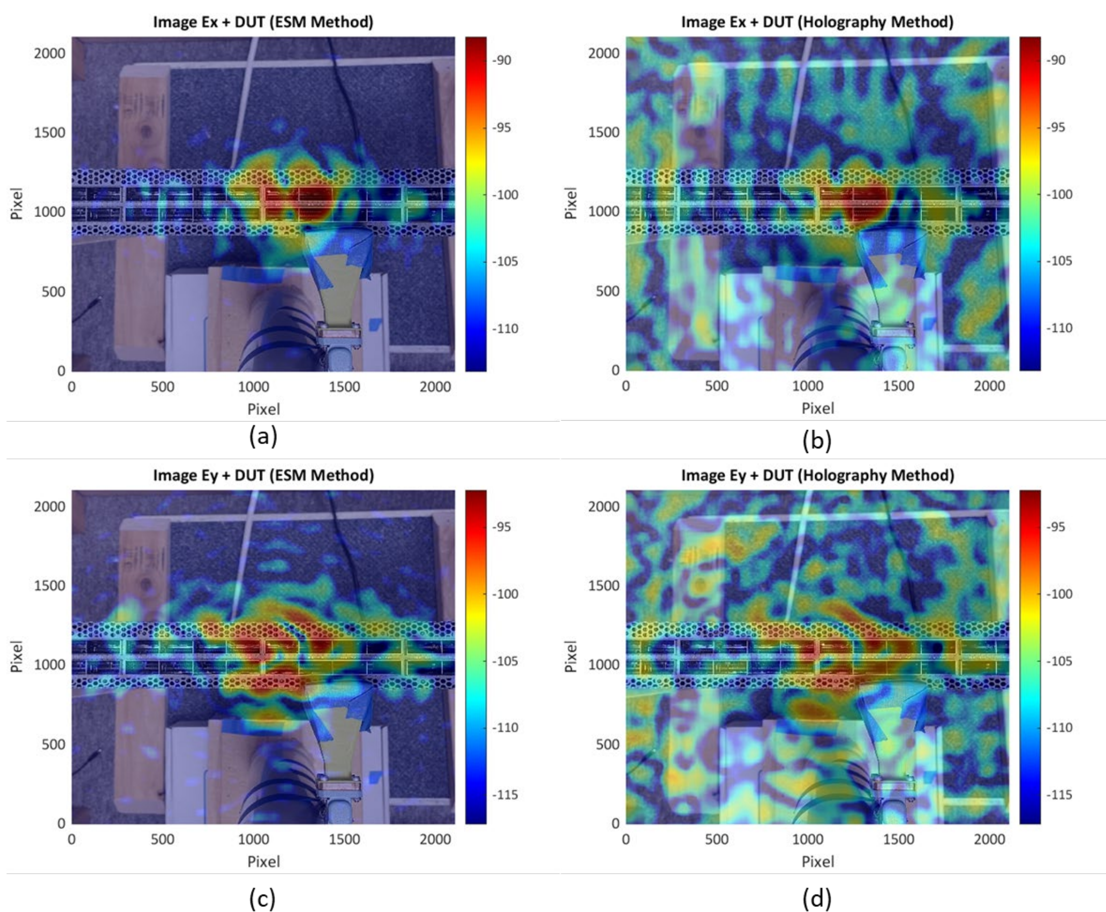

Figure 15. Comparison between ESM and holographic imaging. (a) ESM image of E_x. (b) Holographic image of E_x. (c) ESM image of E_y. (d) Holographic image of E_y. Color scale in dB (arbitrary unit).

Table 1. Maximum field and radiated power comparison

Cases	Maximum E-field	P_{rad}	Reduction of E-field	Reduction of P_{rad}
1	-84.0 dB	-113.2 dB	--	--
2	-91.9 dB	-121.9 dB	7.9 dB	8.7 dB
3	-105.6 dB	-131.6 dB	21.6 dB	18.4 dB

Table 2. Maximum field and radiated power validation

Method	Maximum E-field	P_{rad}
ESM	-86.6 dB	-117.5 dB
Holography	-88.5 dB	-115.0 dB

As can be seen, the differences between the values do not exceed 1.9 dB for the maximum field and 2.5 dB for the radiated power. It should be noted here that the presence of the twin object in holography affects both the maximum field value and the total radiated power. And while the contribution of the twin object image to the maximum field value can be reduced by increasing the from the object to the hologram plane, the contribution of the twin image to the total power does not depend on this distance. Definitely, since the focusing procedure (4) does not affect the absolute value of image spectrum, its power will not be affected as well. By Parseval's theorem, the total radiated power (9) can be calculated by integration of (7) on the hologram plane:

$$P_{rad} = \int_S \left|\frac{R^*O}{|R|^2} + \frac{O^*R}{|R|^2}\right|^2 ds =$$
$$2\int_S \frac{|O|^2}{|R|^2} ds + \int_S \frac{(R^*)^2 O^2 + (O^*)^2 R^2}{|R|^4} ds\,. \qquad (10)$$

The first term in (10) represents the doubled power radiated by the object, while the second one – the mutual power between the actual and twin object waves. The numerical experiments and measurement results in Table 2 indicate that the mutual power is close to zero and the total radiated power measured holographically is two times (3 dB) higher than the actual power produced by the object. Whether or not the mutual power is close to zero under all possible conditions requires additional investigation.

4. CONCLUSION

In this paper, we proposed a phaseless EMI source imaging method based on microwave holography, which is an alternative solution for localization and characterization of active radiation sources by measuring only the magnitude of the fields. The hologram is created by combining the signal from a scan antenna with a reference signal obtained by a stationary antenna. The normalized hologram is backpropagated to the source plane and the image of sources are reconstructed. Comparing with the traditional 2-D ESM algorithm, the twin object effect may degrade the quality of the image. On practice, however, this effect can be mitigated by increasing the backpropagation distance.

The proposed algorithm is efficient and reliable in identifying major radiation sources, determining their location and relative strength. Using the measurement setup

and results shown in Figure 15 as an example, it took 4 hours to finish the scan using ESM method by VNA (Model: Keysight N5245A), as the IF bandwidth had to be reduced to 200 Hz to achieve a sufficient signal-to-noise ratio; zero-span with 250 sampling points and averaging over time samples was used to increase the measurement accuracy. In comparison, it took 40 minutes using the holography method by SA (Model: Agilent E4440A) with 30 Hz resolution bandwidth. In particular, when the amplitude of the radiation sources is very weak such that the measured signals are at or even below the noise level, as shown in Figure 14, the proposed algorithm is still able to produce useful images as opposed to the ESM method which requires a clean signal in the phase reference channel. In addition, using an SA as a receiver allows to increase the measurement sensitivity and reduces costs compared to the methods using a VNA or an oscilloscope. The future work would include calibration of the holographic method and quantitative validation of the radiated power measurement.

REFERENCES

[1] L. Zhang et al., "EMI Coupling Paths and Mitigation in Optical Transceiver Modules," in *IEEE Transactions on Electromagnetic Compatibility*, vol. 59, no. 6, pp. 1848-1855, Dec. 2017.

[2] P. Maheshwari, V. Khilkevich, D. Pommerenke, H. Kajbaf and J. Min, "Application of emission source microscopy technique to EMI source localization above 5 GHz," *2014 IEEE International Symposium on Electromagnetic Compatibility (EMC)*, 2014, pp. 7-11.

[3] P. Maheshwari, H. Kajbaf, V. V. Khilkevich and D. Pommerenke, "Emission Source Microscopy Technique for EMI Source Localization," in *IEEE Transactions on Electromagnetic Compatibility*, vol. 58, no. 3, pp. 729-737, June 2016.

[4] L. Zhang et al., "Sparse Emission Source Microscopy for Rapid Emission Source Imaging," in *IEEE Transactions on Electromagnetic Compatibility*, vol. 59, no. 2, pp. 729-738, April 2017.

[5] J. Li, J. Zhou, S. Yong, Y. Liu and V. Khilkevich, "Automatic sparse ESM scan using Gaussian process regression," *2020 IEEE International Symposium on Electromagnetic Compatibility & Signal/Power Integrity (EMCSI)*, 2020, pp. 671-675.

[6] M. Sørensen, H. Kajbaf, V. V. Khilkevich, L. Zhang and D. Pommerenke, "Analysis of the Effect on Image Quality of Different Scanning Point Selection Methods in Sparse ESM," in *IEEE Transactions on Electromagnetic Compatibility*, vol. 61, no. 6, pp. 1823-1831, Dec. 2019.

[7] D. Gabor, "A new microscopic principle, " *Nature*, vol. 161, no. 4098, pp. 777-778, 1948.

[8] G. Tricoles and N. H. Farhat, "Microwave holography: Applications and techniques," in *Proceedings of the IEEE*, vol. 65, no. 1, pp. 108-121, Jan. 1977.

[9] J. Laviada Martínez, A. Arboleya-Arboleya, Y. Álvarez-López, C. García-González and F. Las-Heras, "Phaseless Antenna Diagnostics Based on Off-Axis Holography With Synthetic Reference Wave," in *IEEE Antennas and Wireless Propagation Letters*, vol. 13, pp. 43-46, 2014.

[10] Tatiana Latychevskaia and Hans-Werner Fink, "Practical algorithms for simulation and reconstruction of digital in-line holograms," Appl. Opt. 54, 2424-2434 (2015).

III. A METHODOLOGY FOR PREDICTING ACOUSTIC NOISE FROM SINGING CAPACITORS IN MOBILE DEVICES

Xin Yan, Jianmin Zhang, Songping Wu, Mingfeng Xue, Chi Kin Benjamin Leung, Eric MacIntosh, and Daryl Beetner

ABSTRACT

Multilayer ceramic capacitors (MLCCs) connected to a power distribution network (PDN) can create acoustic noise through a combination of the power rail noise at the MLCCs and the piezoelectric effect of the capacitor's ceramic material. The deformation of the MLCCs brought on by power supply noise creates vibrations which cause the printed circuit board (PCB) to vibrate and generate the audible acoustic noise. In the following paper, a simulation methodology is presented to analyze the acoustic noise created by MLCCs on a PCB. A simulation model for the PCB vibration modal response is built and the modal superposition method is used to analyze the harmonic response of the PCB excited by the capacitor. By multiplying the measured power noise spectrum on the MLCC with the simulated deformation of the PCB found from the harmonic response analysis, the total response is obtained. Simulated results show a good correlation with the measured acoustic noise. The proposed method shows promise for analyzing and predicting the acoustic noise from singing capacitors.

Keywords: Acoustic noise, harmonic response, modal analysis, multilayer ceramic capacitors, piezoelectric effect

1. INTRODUCTION

With the rapid advance of high-speed digital devices and their integration throughout society, the demand for multilayer ceramic capacitors (MLCCs) has never been higher. One of the most important applications of MLCCs is as decoupling capacitors for the power distribution network (PDN). MLCCs limit power bus noise, which is necessary to ensure the functionality of integrated circuits (IC) connected to the PDN. The effects of MLCC packaging, placement, and ground via layout on PDN noise has been extensity studied [1][2].

With the surge in MLCC usage, however, another issue has become increasingly common. The acoustic noise generated by MLCCs in consumer devices like laptops, cell phones and wireless earbuds, gives the impression of poor product quality and impacts customer satisfaction. While the $BaTiO_3$ dielectric commonly used in MLCCs allows small sized capacitors with high value, it also has a piezoelectric effect. When an electrical signal passes through the MLCC, the MLCC will contract and expand in proportion to the signal. This vibration of the MLCC will be transferred to the PCB to which it is soldered. The MLCC piezoelectric effect is often called ‘singing’ [3][4].

Even through the vibration of an MLCC could be small, there could be dozens to hundreds of MLCCs on the PCB which collectively can create a large “speaker” area and noticeable noise. As a result, the PDN may not only need to be evaluated for its electrical performance, but for the acoustic noise induced by power rail noise on the MLCCs. The correlation between acoustic noise and MLCC vibration was demonstrated in [5], based on a simple test board. In [6], the acoustic noise induced by MLCCs was studied through

a simulation-based investigation of the vibration behavior of the PCB. Optimizing the placement of MLCCs can reduce acoustic noise [7]. Measurement techniques to identify the primary MLCC vibration sources on a PCB were demonstrated in [8] and the relationship between the PDN noise, PCB vibration and acoustic noise were studied.

Although the correlation between the electrical noise on MLCCs and acoustic noise from the system has been demonstrated [7][8], and a practical simulation flow for performing acoustic noise analysis has been presented [9], it is still challenging to predict the acoustic noise over a broad frequency range. Previous studies show that frequencies where the electrical noise on the MLCCs peak correspond to those found in the acoustical noise, but do not show a firm link between the two. Both the power noise spectrum and the PCB vibration properties should be studied when analyzing acoustic noise. A simulation and validation methodology for predicting acoustic noise is proposed in the following article. The acoustic noise can be found from three properties: the PDN noise at the MLCC, the MLCC transfer function from electrical noise to mechanical force, and the vibrational response of the PCB. Acoustic noise can be mitigated by reducing any of these aspects. The PCB vibration properties are found through simulation and considered as a system response. The overall acoustic noise is obtained by combining the electrical power spectrum seen at the MLCCs with the system response. The predicted acoustic noise shows good correlation with the measured acoustic noise, suggesting the proposed method could help engineers analyze and mitigate acoustic noise issues more effectively.

2. ACOUSTIC NOISE MECHANISM AND ANALYSIS METHOD

2.1. MLCC AND PCB VIBRATION

The deformation of MLCCs due to PDN noise causes vibrations which directly generates acoustic noise. While this noise alone is not noticeable to human ears, the MLCC vibration could be transferred to the PCB and produce audible levels of acoustic noise. The PCB response is a primary contributor to the acoustic noise induced by MLCCs. It has been demonstrated that acoustic noise could be analyzed from the vibration of the PCB in previous studies [8]. This article focuses on the simulation analyses of the PCB properties.

2.2. MODAL ANALYSIS AND HARMONIC ANALYSIS

Modal analysis is the study of the vibration characteristics of a structure and can be used to study vibration of a PCB [8]. The analysis starts with the equation of motion:

$$[M]\{\ddot{u}\} + [C]\{\dot{u}\} + [K]\{u\} = [F] \tag{1}$$

where M is the mass, $\ddot{u}$ is acceleration, C is damping, $\dot{u}$ is velocity, K is stiffness, u is displacement, and F is the applied force. As the natural frequencies and associated mode shapes are inherent properties of the structure, independent of external force, and damping has little influence on the structure's modal parameters, the equation of motion used for modal analysis of a free and undamped system can be written as:

$$[M]\{\ddot{u}\} + [K]\{u\} = \{0\} \tag{2}$$

Assuming harmonic motion for every point of the structure, the displacement and acceleration expressions can be written as:

$$\{u\} = \{\phi\}_i \sin(\omega_i t + \theta_i) \tag{3}$$

$$\{\ddot{u}\} = -\omega_i^2 \{\phi\}_i \sin(\omega_i t + \theta_i) \tag{4}$$

Substituting (3) and (4) into (2):

$$([K] - \omega_i^2 [M])\{\phi\}_i = \{0\} \tag{5}$$

where ω_i^2 are the square of the natural frequencies of the structure (i.e. the eigenvalues), and $\{\phi\}_i$ is the mode shape at certain natural frequencies (i.e. the eigenvectors). $[M]$ and $[K]$ are known matrices associated with the PCB structure, so ω_i and $\{\phi\}_i$ can be determined.

The structure tends to vibrate at its natural frequencies. The modal analysis shows the locations where the structure is sensitive to an external applied force. In practice, the PCB is generally fixed to a rigid structure (e.g. the case) at several support locations. These locations need to be set properly in the mechanical model as boundary conditions to accurately calculate natural frequencies and mode shapes.

The results of modal analysis can be used to estimate the displacement of the PCB from an external applied force – in this case the vibration force of the MLCCs – to predict acoustic noise. The displacement of the board at position $\mathbf{X}=\{x,y\}$ from a unit force at the position of MLCC k located at position $\{x_k,y_k\}$ can be expressed as a linear combination of modal shapes:

$$D_{k,\mathbf{X}}(f) = \sum_{i=1}^{n} \phi_{i,X} \{Y_{i,X}\} \tag{6}$$

where $D_{k,\mathbf{X}}(f)$ is the transfer function for the displacement, $\phi_{i,X}$ are the mode shapes calculated through modal analysis for an excitement at $\mathbf{X}$, $\{Y_{i,X}\}$ are the modal

coordinates which will be calculated in harmonic analysis, and n is the number of modes used.

2.3. TOTAL RESPONSE

In addition to the board response, the acoustical noise also depends on the vibration of the MLCCs caused by power supply noise. Here we propose to predict the total response $R_{\boldsymbol{X}}(f)$ at position **X** as:

$$R_{\boldsymbol{X}}(f) = \sum_{k=1}^{m} a_k\,(f) \cdot P_k(f) \cdot D_{k,\boldsymbol{X}}(f) \tag{7}$$

where f is frequency, $P_k(f)$ is the power supply noise at MLCC k, $a_k(f)$ is a transfer function between the electrical noise (in watts) at MLCC k to the force generated by the MLCC, and the total response is determined from a summation of the displacement caused by all MLCCs on the board, m. Here, the transfer function $a_k(f)$ will be assumed to have a uniform value over the frequency range of interest for simplicity, as the aim of the study is to estimate the frequency response of the acoustic noise, rather than estimate its actual value.

3. SIMULATION AND VALIDATION ON A REAL PRODUCT

3.1. MODAL ANALYSIS OF PCB

The device under test (DUT) investigated in this article was a PCB from a wireless earbud. The PCB consists of 8 copper layers with FR-4 dielectric in between. The mechanical model of the PCB is shown in Figure 1. All components were included

and are modeled as rectangular or cylindrical blocks, including individual RLC components, ICs, connectors and microphones.

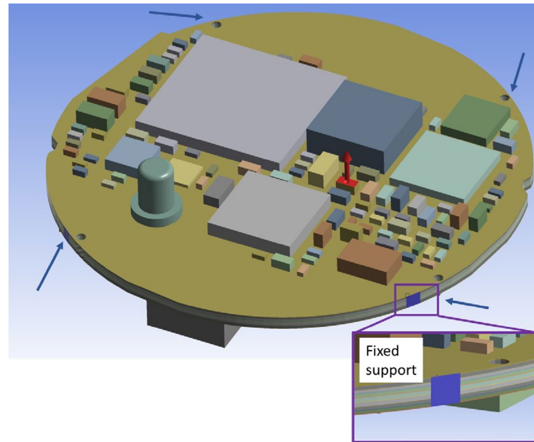

Figure 1. Mechanical model of the PCB. Blue arrows indicate the locations of fixed support. The red arrow indicates the location of the external force added to the dominant MLCC to simulate the board response. The inset shows an expanded view of one of the fixed supports.

The material density, volume and Young's modulus of the PCB and the mounted components are critical to accurately determining the mechanical response of the system. The dielectric material in the PCB was modeled as a uniform structure with density 1.85 g/cm^3 and Young's modulus 20 GPa. As modeling the copper traces directly would require a small mesh size and many elements, the copper layers were modeled as uniform layers with an appropriate mix of copper and FR4, and the equivalent density and Young's modulus was calculated accordingly. The parameters for the components were obtained from vendors and datasheets.

The PCB under study was fixed to the shell of the earbud with glue at four locations. Four fixed supports were added to the sides of the PCB at similar locations, as

shown by the blue arrows in Figure 1. These fixed supports were the boundary conditions for modal analysis.

Simulation of the first 8 modes gave the natural frequencies shown in Table 1. The first and second natural frequencies are 8417 Hz and 11756 Hz, respectively. The modal shapes for these frequencies are shown in Figure 2. Because the structure tends to vibrate at the natural frequencies, higher acoustic noise is expected at these frequencies.

Table 1. First eight modal frequencies of the DUT

Mode	Frequency [Hz]	Mode	Frequency [Hz]
1	8417	5	23681
2	11756	6	30547
3	13093	7	35871
4	17822	8	38385

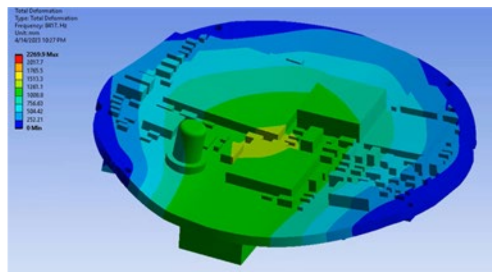

(a)

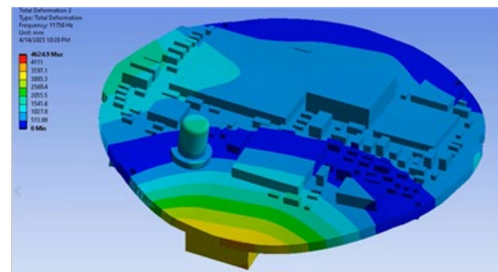

(b)

Figure 2. Modal shapes associated with (a) Mode 1, and (b) Mode 2.

3.2. HARMONIC ANALYSIS OF PCB

The power noise at the MLCCs is needed to determine the total PCB response. While there are several MLCCs in this prototype earbud, one MLCC was found to have up to 20 dB more power noise than other MLCCs and to dominate the acoustic noise. The power noise spectrum on this MLCC is shown in Figure 3. The measured frequency is from 100 Hz to 20 kHz, which covers the hearing range of most humans. There is a peak at 800 Hz, which is the fundamental frequency of the IC, as well as harmonics at 1600 Hz, 2400 Hz and so on. Broadband power rail noise is also shown in the power noise spectrum.

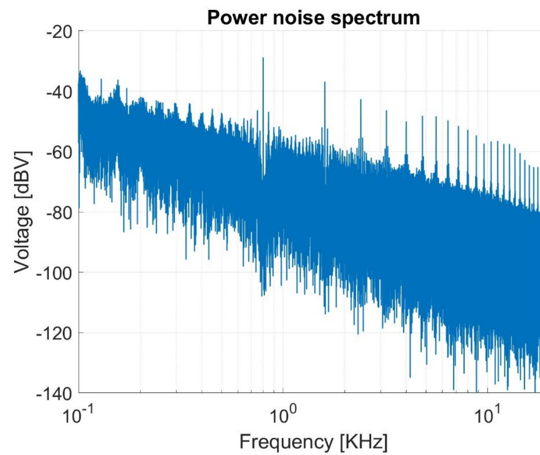

Figure 3. Power noise spectrum of the dominant MLCC.

As the power noise on one MLCC is expected to dominate the PCB response, a harmonic analysis was performed with a uniform force applied to the surface of this MLCC as shown in Figure 1 (Red arrow) in order to obtain $D_{k,\boldsymbol{X}}(f)$ as in (6). The simulation was performed from 0 to 20000 Hz in 50 Hz steps. ‘Cluster results’ was

activated, so the software (Ansys Mechanical) could automatically increase the frequency points around the natural frequencies without missing the peaks. The force was set to 1 N for all frequencies. To avoid unrealistically high peak values at the natural frequencies, a 0.01 damping ratio was added.

The average deformation across the entire PCB found in simulation from this one MLCC is shown in Figure 4. The frequencies that show peak deformation are matched with the natural frequencies. Below the first natural frequency, especially lower than 4 kHz, the frequency response is almost flat, which means the structure is not sensitive to vibration in this frequency range.

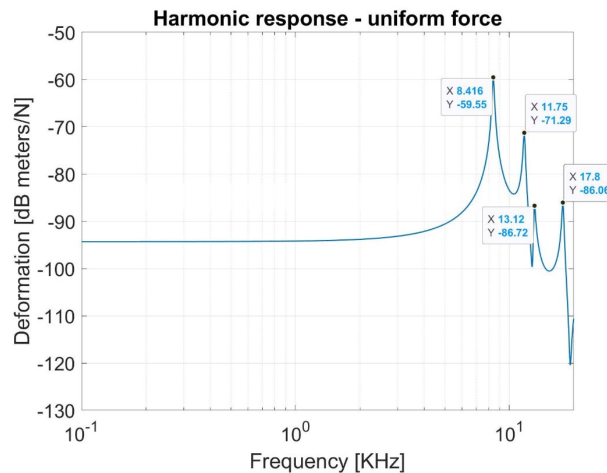

Figure 4. The deformation of the structure.

3.3. MEASURED ACOUSTIC NOISE AND PREDICTED RESPONSE

The acoustic noise of the DUT was measured in a mini acoustic chamber with a very low noise floor. The measurement setup is shown in Figure 5. An ear simulator was

placed in the chamber. Ear simulators are important devices for objective evaluation of the acoustic performance of different earphones. In this setup, the earbud was placed in the ear simulator and the acoustic noise was measured while blank audio was playing.

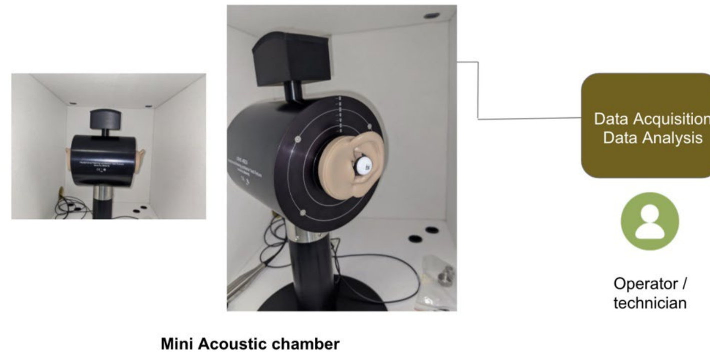

Figure 5. Acoustic noise measurement setup.

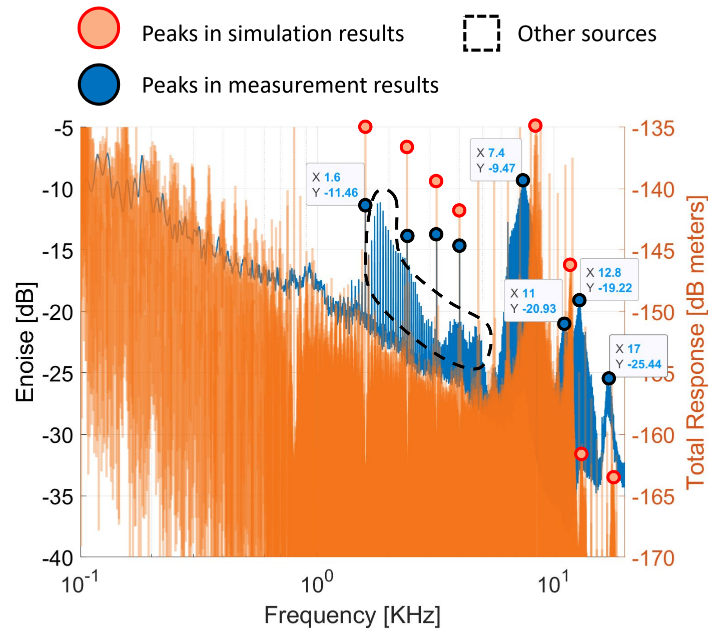

Figure 6. Blue curve/dots: measured acoustic noise. Orange curve/dots: Average absolute displacement across the PCB predicted from noise on the dominate MLCC. Area circled with dotted line: “other” sources of noise.

The measured acoustic noise from 100 Hz to 20 kHz is shown with the blue curve in Figure 6. The harmonics of the 800 Hz fundamental frequency are shown in the acoustic noise measurement at 1.6 kHz, 2.4 kHz and so on. Between 1.6 kHz and 3 kHz, there are many narrow peaks, which were shown to come from other sources but not further investigated (circled in black). Four broad peaks are shown at 7.4 kHz, 11.0 kHz, 12.8 kHz, and 17 kHz which are most likely caused by the 'singing' capacitor effect.

Table 2. Comparison of the Broad Peaks

Peaks	Prediction	Measurement
1	8.4 kHz	7.4 kHz
2	11.8 kHz	11.0 kHz
3	13.1 kHz	12.8 kHz
4	17.8 kHz	17.0 kHz

The displacement of the PCB caused by vibration of the dominant MLCC was estimated from the measured power noise across this MLCC and the simulated transfer function $D_{k,\boldsymbol{X}}(f)$, assuming $a_k(f) = 1$. The orange curve in Figure 6 shows the average absolute displacement predicted across the entire PCB. The impact of the power rail noise is shown in the response. Overall, the average predicted displacement tends to follow a similar trend as the measured acoustic noise. The four broad peaks in the total response match peaks in the measured acoustic noise, as shown in Table 2, though these peaks in measurement occur at somewhat lower frequencies than the predicted resonant frequencies, most likely because of the added weight of components connected to the

board that were not simulated, like the shell, cables, connectors, etc. The narrow peaks which are the harmonics of the 800 Hz fundamental frequency are also shown in the total response. These results suggest that the proposed simulation method could be used to predict the frequency response of acoustic noise. While this simulation did not find the "broadband" noise, e.g. circled in black in Figure 6, simulations were performed only for the capacitor with the largest power-supply noise.

4. CONCLUSIONS

The mechanisms by which MLCCs generate acoustic noise on PCBs were studied, and a method for predicting the severity of that noise was presented. The inherent vibration properties of a PCB can be analyzed using modal analysis, and a transfer function for MLCC vibration to board response can be estimated using modal superposition. An equation predicting the PCB displacement from the MLCC/board transfer function and the MLCC power supply noise was proposed. The proposed methods were validated on a prototype earbud. The trends in the average predicted board displacement are similar to the measured acoustic noise, with the major broad peaks in the acoustic noise found in both simulations and measurement. The proposed simulation methods show promise for analyzing the impact of singing capacitors on acoustic noise.

The proposed method demonstrates that the acoustic noise can be predicted from three components: the power supply noise at the MLCCs, the transfer function(s) that converts power supply noise into MLCC vibration, and the transfer function for system deformation resulting from the MLCC vibration. Acoustic noise could be mitigated by

reducing any of these effects. The flow chart of acoustic noise analysis is given in Figure 7.

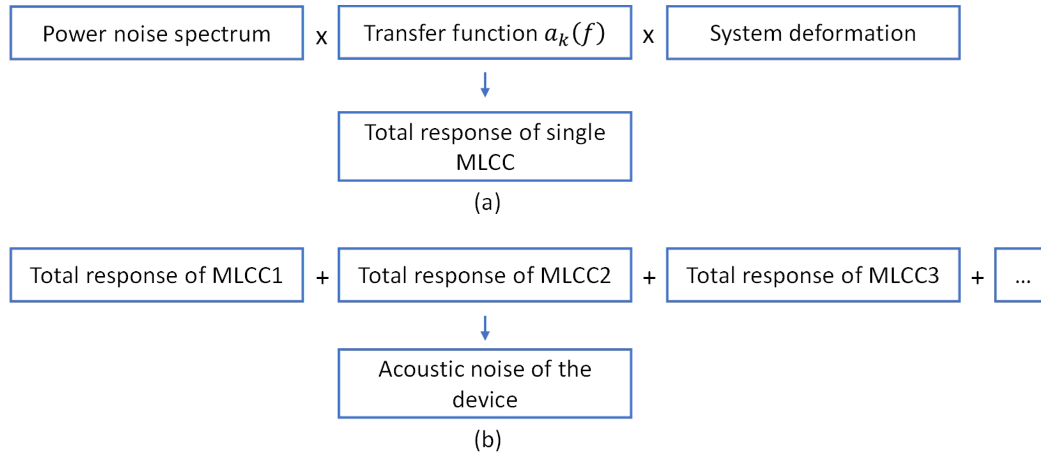

Figure 7. Flow chart of the proposed acoustic noise analysis. (a) Total response of single MLCC. (b) Acoustic noise of the device.

In the DUT studied here, the power noise was worst on one MLCC which also dominated the acoustical noise, so acoustical noise was only estimated from this one MLCC. In reality, multiple MLCCs are 'singing' in this design. The total response from all singing capacitors could be predicted as a superposition of each response, as indicated in (7), so long as the power supply noise is known.

In this study, the transfer function $a_k(f)$ from power supply noise at the MLCC to a vibrational force was assumed to be 1 for simplicity. With accurate $a_k(f)$, the predicted frequency response will be more accurate, and comparison of absolute values of the acoustic noise can be achieved. Better determining this transfer function is an important task for future study.

REFERENCES

[1] L. Zhang, Z. Zhang, C. Huang, H. Deng, H. Lin, B. Tseng, J. Drewniak and C. Hwang, "Decoupling Capacitor Selection Algorithm for PDN Based on Deep Reinforcement Learning," *2019 IEEE International Symposium on Electromagnetic Compatibility, Signal & Power Integrity (EMC+SIPI)*, 2019, pp. 616-620.

[2] B. Zhao et al., "Decoupling capacitor power ground via layout analysis for multi-layered PCB PDNs," in *IEEE Electromagnetic Compatibility Magazine*, vol. 9, no. 3, pp. 84-94, 3rd Quarter 2020.

[3] J.D. Prymak, "Piezoelectric effects ceramic chip capacitors (singing capacitors), " *Arrow Asian Times*, 2006.

[4] *Singing Capacitors (Piezoelectric Effect)*, TDK, Dec 2006. [Online]. Available: https://product.tdk.com/system/files/contents/faq/capacitors-0031/singing_capacitors_piezoelectric_effect.pdf

[5] B.H. Ko, S.G. Jeong, Y.G. Ahn, K.S. Park, N.C. Park, and Y.P. Park, "Analysis of the correlation between acoustic noise and vibration generated by a multi-layer ceramic capacitor," *Microsyst. Technol.*, vol. 20, no. 8-9 , pp.1671-1677, Aug. 2014.

[6] Y. Sun, S. Wu, J. Zhang, C. Hwang and Z. Yang, "Simulation Methodologies for Acoustic Noise Induced by Multilayer Ceramic Capacitors of Power Distribution Network in Mobile Systems," in *IEEE Transactions on Electromagnetic Compatibility*, vol. 63, no. 2, pp. 589-597, April 2021.

[7] Y. Sun, S. Wu, J. Zhang, C. Hwang and Z. Yang, "Decoupling Capacitor Layout Design Guidelines for Acoustic Noise Consideration in Power Distribution Network," *2020 IEEE International Symposium on Electromagnetic Compatibility & Signal/Power Integrity (EMCSI)*, 2020, pp. 357-362.

[8] Y. Sun, S. Wu, J. Zhang, C. Hwang and Z. Yang, "Measurement Methodologies for Acoustic Noise Induced by Multilayer Ceramic Capacitors of Power Distribution Network in Mobile Systems," in *IEEE Transactions on Electromagnetic Compatibility*, vol. 62, no. 4, pp. 1515-1523, Aug. 2020.

[9] X. Yan, S. Wu, M. Xue, C. K. B. Leung, D. Beetner and J. Zhang, "A Practical Simulation Flow for Singing Capacitor Based Acoustic Noise Analysis," *2022 IEEE International Symposium on Electromagnetic Compatibility & Signal/Power Integrity (EMCSI)*, Spokane, WA, USA, 2022, pp. 29-33.

IV. UNWANTED FIELD COUPLING MECHANISM OF MAGNETIC NEAR-FIELD PROBE

Xin Yan, Wei Zhang, Sajjad Sadeghi, Mehdi Gholizadeh, David J. Pommerenke, and Daryl G. Beetner

ABSTRACT

Unwanted field coupling is always a major concern when using magnetic near-field probes for near-field scanning. The unwanted coupling to a tangential E-field has been studied extensively and in detail. This paper shows a second unwanted coupling mechanism: Coupling to a vertical magnetic field The standing wave of a shorted microstrip is utilized to separate the magnetic and electric field coupling in simulation and measurements. Simulation results show that the opposite eddy currents induced within the probe by the vertical magnetic field, which then generate tangential magnetic field inside the probe and couple to the probe trace. It shows that a symmetric stack-up PCB probe could mitigate the unwanted magnetic field effectively. The unwanted magnetic field coupling mechanism is validated through both simulation and measurement, and two optimization designs are proposed.

Keywords: Unwanted field coupling, magnetic near-field probe, shorted microstrip

1. INTRODUCTION

N ear-field scanning is often utilized to investigate EMC issues [1]-[3]. In recent years, various magnetic near-field probes have been designed [4]-[22]. Most of the

designs are manufactured using PCB and consist of outer ground (on top and bottom layers) and inner trace (on middle layer) structures. Via fence or edge plating technique are usually applied to achieve better shielding to suppress unwanted E-field coupling. Different properties have been optimized: such as narrow band resonant probes [5][6], or broadband passive and active probes [7]-[13], probes with high electric field suppression [15]-[17], probes that use spatial resolution improvement techniques [18][19] and multi-component magnetic field probes [20][21]. A practical and effective of probe calibration was presented in [22]. By referencing measured data to the known field above microstrip, the probe factor is obtained over a broad frequency range. This method is still widely used today.

Unwanted field coupling of magnetic probes is always a major concern in the near-field measurement. The unwanted E-field coupling mechanism has been explained extensively in [23][24]. The common mode E-field coupling could be reduced effectively by a highly symmetrical outer shield. Thus, the differential mode E-field is the major unwanted E-field source, and the highest level of the coupling occurs at the edges of the trace, where the tangential E-field dominates [23]. It is worth mentioning that the difference of the coupling mechanisms between the wanted magnetic field and the unwanted electric field is also visible in the difference in the frequency response of the probe output. The magnetic probe output from wanted coupling is proportional to ω [14], which gives 20 dB per decade response on S-parameter before the parasitics of the probe dominates at high frequency. On the other hand, the unwanted E-field coupling is proportional to ω^2 (equation 17 in [24]), as the voltage induced on the inductance of the probe is caused by the capacitive source $j\omega C$, and 40 dB per decade response is excepted.

The frequency dependences of the E-field coupling can be also understood from the circuit diagram of Figure 18 in [23], where the probe output (voltage across the inductances) is induced by the capacitance coupling from the probe to the DUT trace. It is noticed that the 40 dB per decade behavior is barely seen in practice. Around 30 dB per decade response from the unwanted coupling was shown in the measured results in [23][24], which can be explained by the measurement error (not fully rotated 90 degrees) and the parasitics of the probe. In [14], however, a pure 20 dB per decade of unwanted coupling was shown, which indicates that there could be an unknown coupling mechanism for the magnetic probe.

In this paper, we reveal and analyze another unwanted coupling mechanism – the unwanted magnetic field coupling. The differences of the unwanted coupling between symmetric and asymmetric stack-up PCB probe are observed first. Shorted microstrip is utilized to separate the magnetic and electric field coupling in full wave simulation tool. Simulation results show that a symmetric stack-up probe could mitigate the unwanted magnetic field coupling effectively. The mitigation method is validated through simulation, and two optimization designs are proposed from the analysis.

2. PROBE STRUCTURE AND UNWANTED COUPLING TEST

2.1. PROBE STRUCTURE

The probe structure is shown in Figure 1. The probe is made on multiple layers PCB, where top and bottom layers form the shield. The trace is in the middle layer. Edge plating, including a slot to allow the H-field to reach the trace is modelled. An SMA

connector is used for probe output. Simulation ensures low reflection at the probe trace to SMA transition.

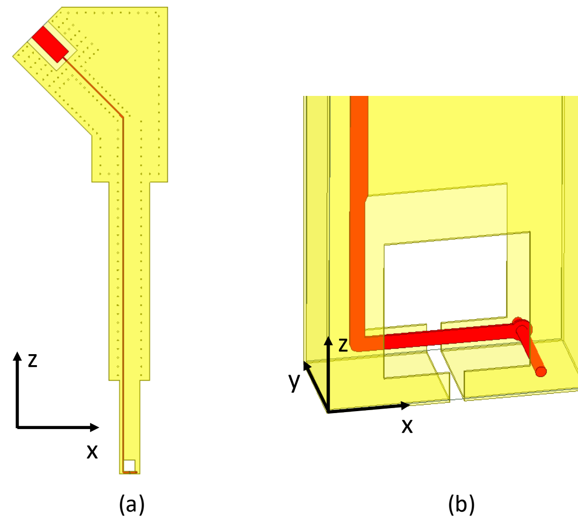

Figure 1. (a) Overview of the probe (b) Probe tip structure. The figure shows an asymmetrical design, other designs place the trace symmetric between the two shield layers.

2.2. UNWANTED COUPLING TEST

As previous mentioned, the highest level of the unwanted coupling locates at the edges or some distance from the trace, because the differential mode E-field coupling is the major unwanted source [23] as the common mode coupling has been suppressed by the highly symmetrical outer shield. To accurately obtain the unwanted field coupling level, the probe should be scanned across the microstrip after 90 degrees rotation, as described in Figure 2 (a). In Figure 2 (b), a typical distribution of the unwanted coupling across a 3mm microstrip is presented. It can be seen that highest coupling is at the outside of the trace, and the lowest coupling is at the center of the trace where only the common

mode coupling exists. Afterwards, the frequency response of the unwanted coupling can be obtained by taking the highest values along the x direction at each frequency.

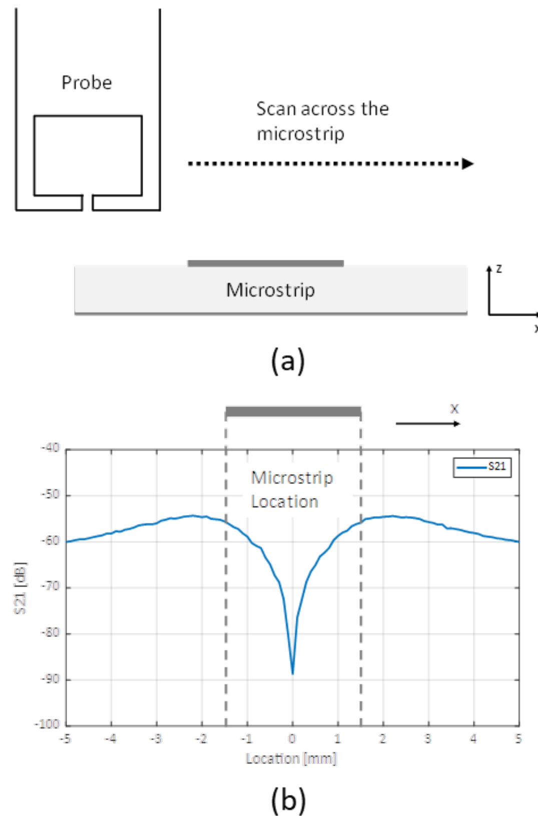

Figure 2. (a) Diagram of unwanted coupling test. (b) A typical distribution of the unwanted coupling across the microstrip.

3. UNWANTED MAGNETIC FIELD COUPLING MECHANISM

3.1. SYMMETRIC AND ASYMMETRIC PROBE

First, the differences of the unwanted coupling for symmetric and asymmetric probes were observed in simulation. The ‘symmetric’ term in this paper means the symmetry of the PCB stack up, instead of the structure of the probe, as shown in Figure 3

(a). The asymmetric probe is usually built with a 4-layer PCB, where one middle layer is unused. The symmetric probe can be considered as a 3-layer PCB probe, which is less common. The trace width for symmetric probe above the loop structure is adjusted to match 50-ohm impedance.

The unwanted coupling simulated results of both probes are shown in Figure 3 (b). It shows a trend of about 40 dB/dec up to 1 GHz. Above, parasitics effects dominate. The 40 dB/dec trend is explained by the tangential E-field coupling mechanism [23]. The asymmetric probe shows 20 dB/dec which cannot be explained by the tangential E-field coupling. Thus, a second, so far unpublished mechanism dominates.

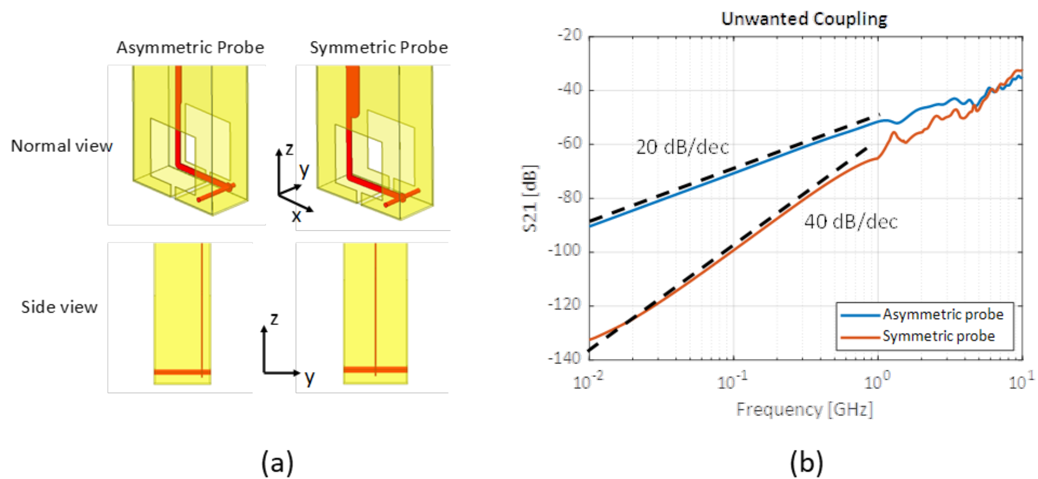

Figure 3. (a) Structures of asymmetric and symmetric probes. (b) Unwanted coupling of asymmetric and symmetric probes.

3.2. SHORTED MICROSTRIP

To analyze the E-field and H-field couplings separately, shorted microstrip was utilized. Standing wave can be generated on shorted microstrip, so that E-field maxima

correspond to H-field minima, and vice versa. The shorted microstrip is designed in Ansys HFSS, as shown in Figure 4 (a). One end of the microstrip was a wave port excitation and the other end was terminated with a zero-ohm lumped element. Air dielectric was used to provide TEM-mode wave. To obtain the frequency behavior of the unwanted coupling, two difference lengths of microstrip were built. 300 cm length microstrip was used for 100 MHz simulation, and 30 cm length microstrip was for 1 GHz. As the length of the shorted microstrip is equal to the wavelength of interested frequency, the maximum E-field is at the middle of the microstrip - half wavelength position and the maximum H-field is at the quarter wavelength position.

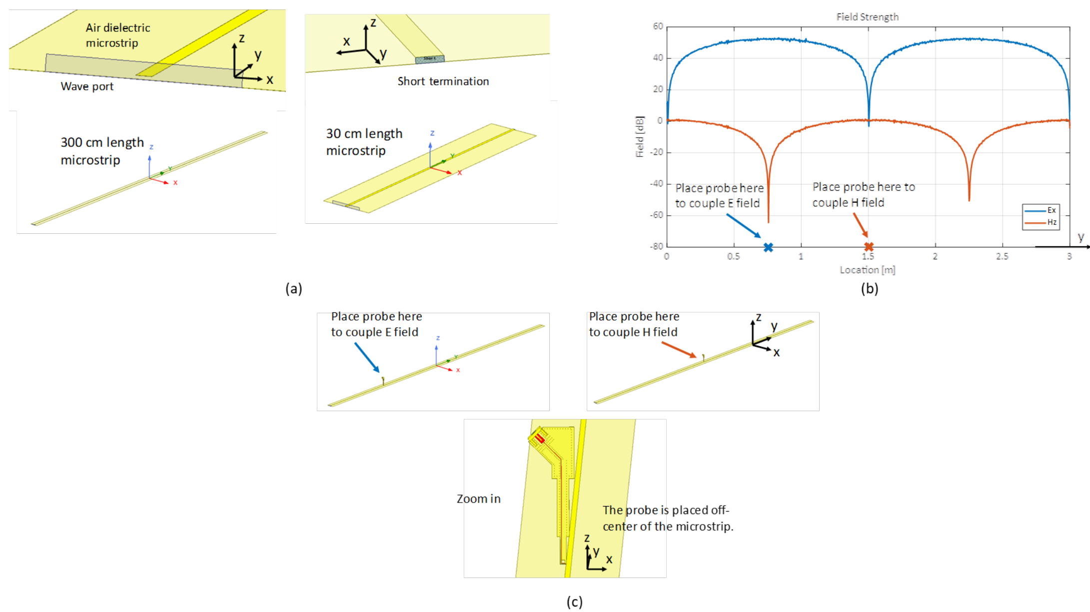

Figure 4. (a) Shorted microstrips with air dielectric. (b) Off-center Ex and Hz field distributions along the 300 cm microstrip. (c) Diagram of probe positions for unwanted E and H field coupling.

Figure 4 (b) shows the simulated Hz and Ex field on the side above of the 300 cm microstrip. The standing waves pattern is clearly visible, and the maximum E-field and H-field are at the half-wavelength and quarter wavelength positions respectively, as expected.

The probe was placed at the minimum H-field and E-field positions on both 300 cm and 30 cm microstrips, to couple to E-field and H-field separately. The probe was placed off-center of the microstrip to couple highest unwanted field, as shown in Figure 4 (c).

Table 1. Unwanted Coupling from E-field and H-field

	E-field	Delta of E-field	H-field	Delta of H-field
100 MHz Asymmetric probe	-93.9 dB	42.3 dB	-71.8 dB	19.7 dB
1 GHz Asymmetric probe	-51.6 dB		-52.1 dB	
100 MHz Symmetric probe	-96.0 dB	43.8 dB	-112.4 dB	23.6 dB
1 GHz Symmetric probe	-52.2 dB		-88.8 dB	

The unwanted coupling results from E-field and H-field for both asymmetric and symmetric probes are given in Table 1. By comparing the couplings at 100 MHz and 1 GHz, we calculate the increment of the couplings over a decade. The results show two interesting behaviors of the probes:

1. About 40 dB/dec trend is shown from E-field coupling for both asymmetric and symmetric probes. The E-field coupling strength for both probes is similar.
2. About 20 dB/dec trend is shown from H-field coupling for both asymmetric and symmetric probes. However, the H-field coupling for asymmetric probe is much higher than symmetric probe.

The results in Table 1 correlate with the Figure 3 (b), where a common microstrip (3 mm trace width, FR4 dielectric and 50-ohm termination) was used. For asymmetric probe, the unwanted H-field coupling dominates, then 20 dB/dec trend is shown. For symmetric probe, the H-field coupling is smaller than E-field coupling, therefore 40 dB/dec trend is observed.

It is worth mentioning that after the probe is rotated 90 degrees for unwanted coupling test, Hx is no longer able to couple to the probe as the side edge-plating or via fence blocks it. Hy – the H-field along the propagation direction should be neglectable since it tends to zero above a 50-ohm terminated microstrip (quasi-TEM mode) at low frequencies. Therefore, it is reasonable to consider that Hz is the source of unwanted H-field coupling. It is worth noting that the distribution of Hz across the microstrip is same as Ex, and the highest level is located off-center of the microstrip.

3.3. SURFACE CURRENT

To analyze the interaction between the Hz field and probe structure, surface current on the probe was simulated and plotted at the minimum H-field and E-field positions. Surface current on top and bottom grounds and bottom edge-plating plane are

plotted. Figure 5 and Figure 6 show the surface currents from H-field and E-field couplings respectively. In Figure 5 (a), it can be seen that opposite eddy currents are induced on the top and bottom loop structures for both outer and inner surfaces. In Figure 5 (b), eddy currents are shown on the outer surface of the bottom edge-plating plane. On the inner surface, the current is flowing in y direction – between the top and bottom layers, and the currents on both sides of the gap are in opposite directions. When coupled from E-field shown in Figure 6 (a), however, the surface currents are much weaker and the currents on the top and bottom grounding layers are in the same direction. The surface currents on bottom metal plane are also much weaker, as shown in Figure 6 (b). The eddy current on outer surface is caused by weak H-field at the E-field maxima location and can be ignored. In the inner surface, no significant y-direction current is observed.

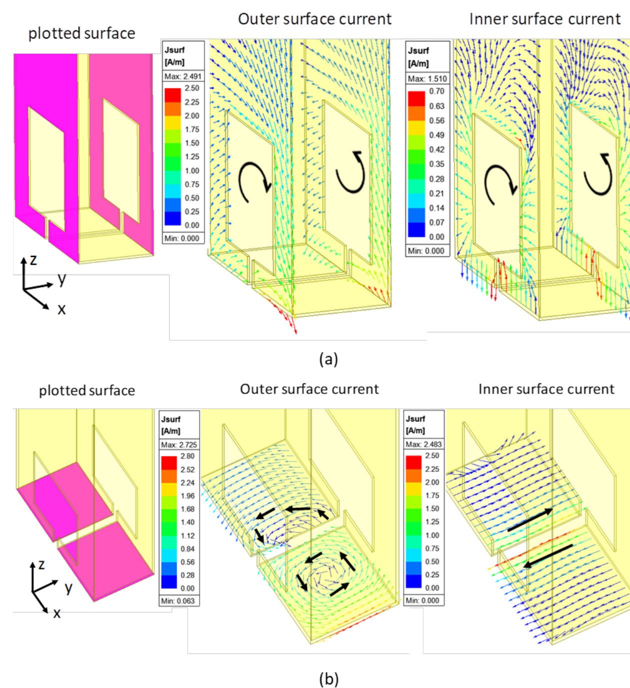

Figure 5. Surface current from H-field coupling. (a) Probe ground surface. (b) Bottom edge-plating surface.

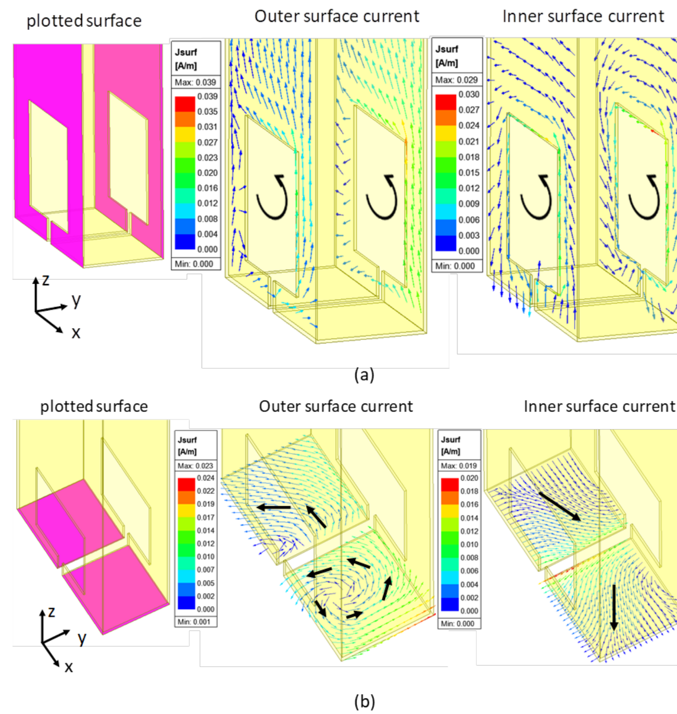

Figure 6. Surface current from E-field coupling. (a) Probe ground surface. (b) Bottom edge-plating surface.

The surface current results show the unwanted H-field and E-field couplings have different mechanisms. Under the E-field coupling (Ex, the tangential E-field), the metals on both sides of the gap can be treated as a capacitor and have different voltage potentials. The top and bottom layers on one side of the gap have equal potentials, therefore the currents on the grounding loop structures of top and bottom layers are in the same direction. Under the H-field coupling (Hz), however, loop currents are induced, and the top and bottom ground planes on one side of the gap no longer have equal potentials. As a results, the opposite currents flow on top and bottom layers, along with the opposite currents on the bottom metal plates, form a complete loop current.

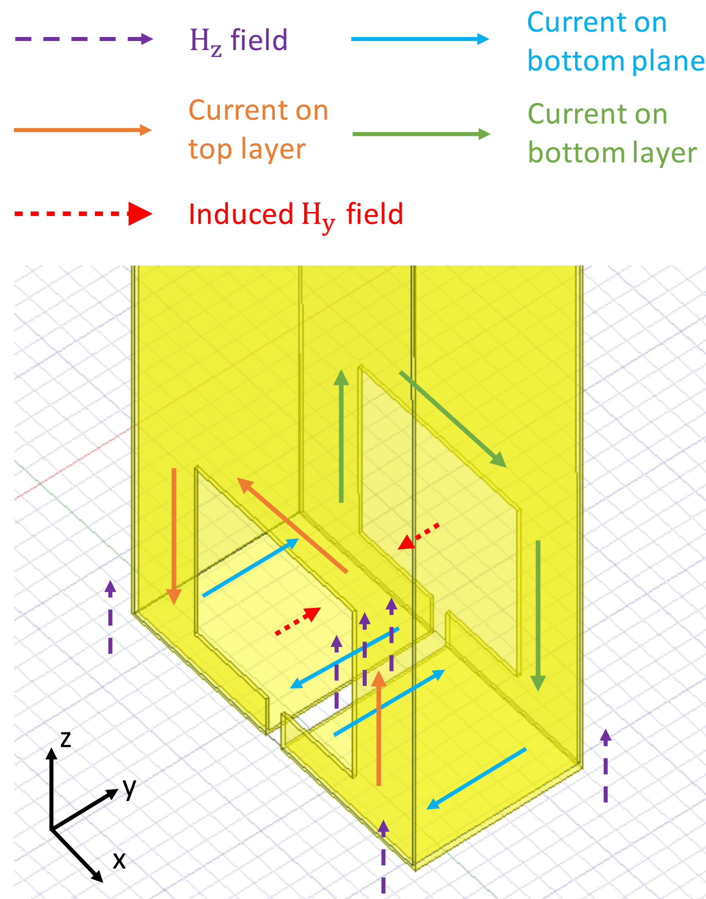

Figure 7. Diagram of the unwanted magnetic field coupling mechanism.

3.4. UNWANTED MAGNETIC FIELD COUPLING MECHANISM

Based on the above analysis and simulation results, we propose the unwanted magnetic field coupling mechanism. The diagram of the mechanism is shown in Figure 7. The probe is surrounded by the Hz field, which can also go inside of the probe through the gap. Surface loop currents are induced by the Hz field on the bottom and side edge-plating planes. On the same side of the gap, some currents flow through the outer and inner surfaces and form the loop. Some of the currents, however, flow through the top or bottom layer and go to the other side of the gap. These currents form a large loop and

cause the opposite directions on the top and bottom ground loop structures. As a result, Hy fields are induced from the top and bottom loop structures in opposite directions. The Hy fields are coupled to the probe trace as the unwanted magnetic coupling. For asymmetric probe, the probe trace is closer to one ground layer and the coupling is strong. For symmetric probe, however, as the Hy fields are in opposite directions, the field is cancelled at the middle of the probe, thus the unwanted magnetic coupling is suppressed significantly.

One evidence for the coupling mechanism is the Hy field strength inside the probe. Figure 8 shows the H field distributions along the y-direction at the location of the maximum unwanted coupling. The air microstrip was terminated with 50 ohms, and the Hy and Hz field were simulated with and without the probe structure at 100 MHz. The location of the plotted field was at the center of the loop (same location when no probe exists), as shown in Figure 8 (a). Figure 8 (b) shows the Hy magnitudes with and without the probe structure. As can be seen, Hy field is very low and negligible when no probe exists because of the TEM mode. With the probe structure, Hy field is induced and reaches its maximum near the top or bottom layers of the probe. At the middle of the probe, local minimum of the Hy field is shown, as we analyzed previously. The phase of the Hy field in Figure 8 (c) shows that the phase difference between the left and right sides of the probe is about 180 degrees, with the transition occurring at the center. The Hz field with the probe is only about 5 dB lower than the Hz without the probe, as shown in Figure 8 (d), indicating that the Hz field can enter the probe through the gap at the bottom.

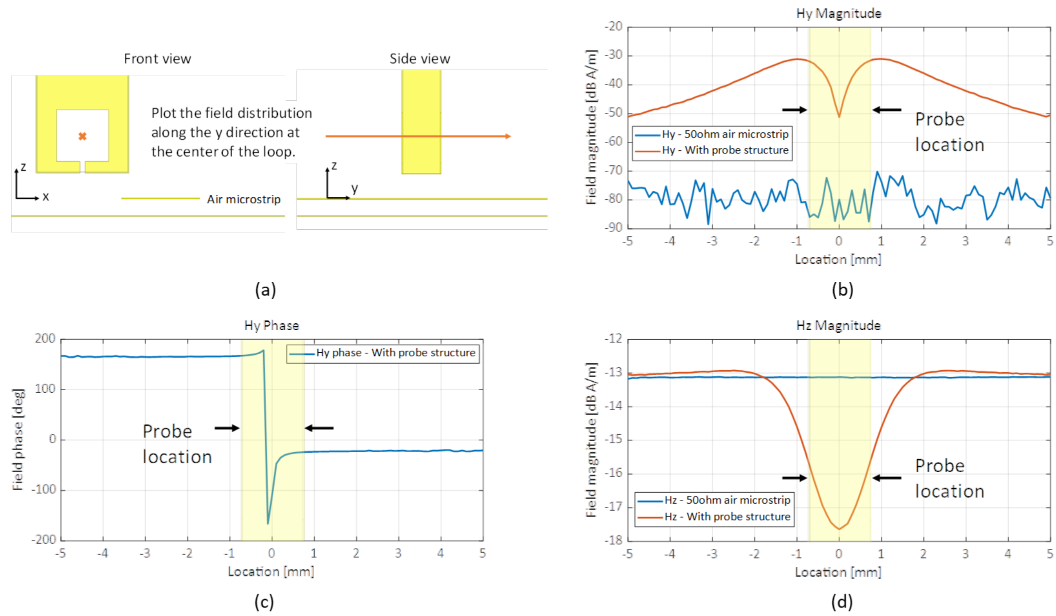

Figure 8. Hy and Hz distributions above air microstrip with and without probe grounding structure. (a) Overview of the simulation setup. (b) Comparison of the Hy magnitudes. (c) Phase the Hy with the probe structure. (d) Comparison of the Hz magnitudes.

4. PROBE DESIGN OPTIMIZATION

Based on above analyzes and explanations of unwanted magnetic coupling, there are two main directions to mitigate the coupling – make a symmetric structure or suppress the unwanted field. In this paper, we propose two optimization designs to reduce the unwanted magnetic coupling. Figure 9 (a) shows a 4 layers probe with parallel traces. In this case, both traces couple to the unwanted Hy field with opposite current directions. The coupled currents are shorted and form a loop current by the two trace vias directly, therefore the unwanted signal to the probe output is reduced significantly. In Figure 9 (b), we add a shielding structure under the probe while the probe design is unchanged. The shielding structure could suppress the Hz field that goes into the probe, so the induced Hy

field is suppressed, as shown in Figure 10. Figure 11 shows the comparisons of the couplings between different probes. As can be seen in Figure 11 (a), the unwanted couplings of the two optimization approaches are suppressed efficiently at low frequencies, while above 2 GHz, the unwanted coupling is dominated by other parasitics, and the optimization methods don't have much effect. Figure 11 (b) shows the wanted coupling of these designs. The optimization approaches don't affect the sensitivity of the probe at low frequencies. The probe with parallel traces shows a lower resonant frequency as the additional trace introduces more inductance. Overall, the two optimization approaches work as expected and further prove the unwanted magnetic field coupling mechanism.

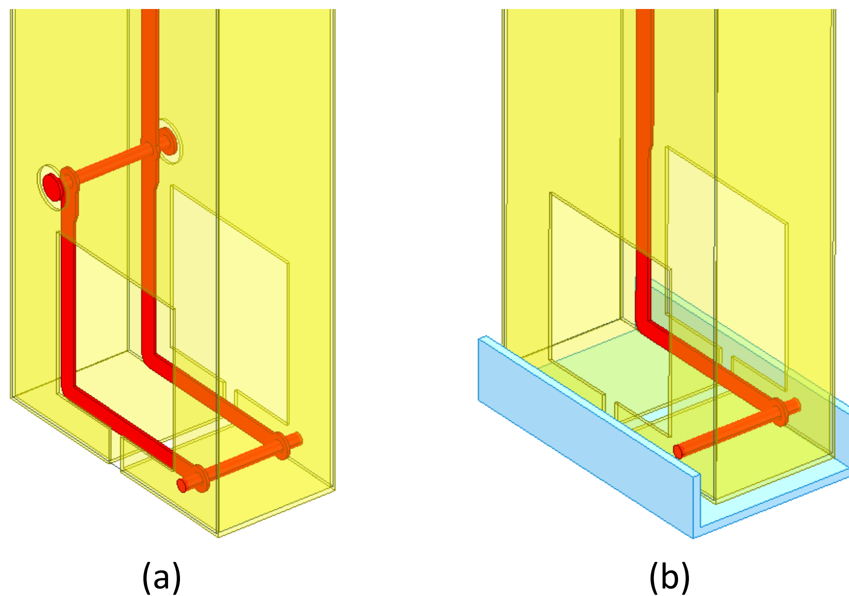

Figure 9. Probe optimization methods. (a) Probe with parallel traces. (b) Shielding structure under the probe.

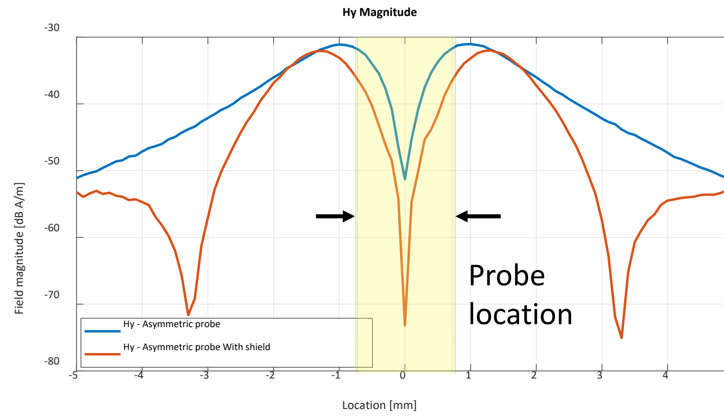

Figure 10. Comparison of the Hy magnitude between original asymmetric probe and the probe with shield (design shown in Figure 9 (b)).

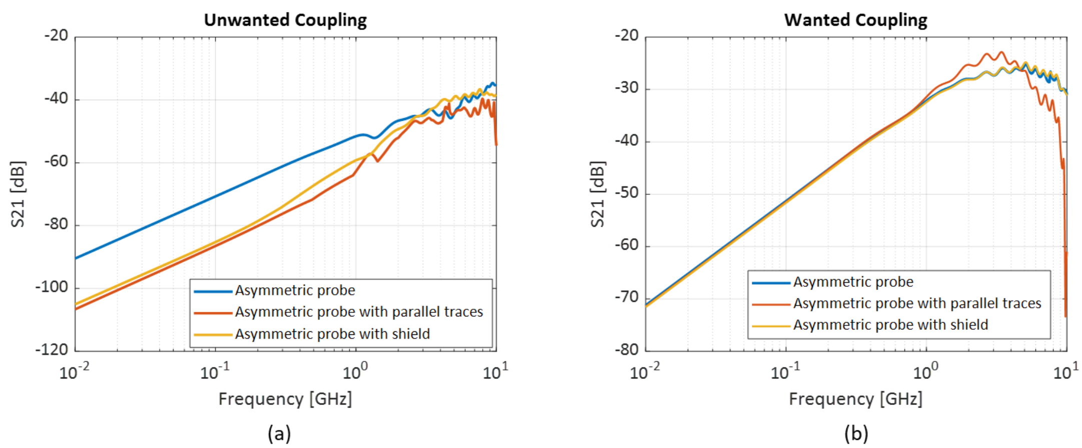

Figure 11. Comparisons of the optimization designs. (a) Unwanted coupling. (b) Wanted coupling.

5. CONCLUSION

In this paper, the unwanted magnetic field coupling of magnetic near-field probe is analyzed and explained. The differences of the unwanted coupling between asymmetric and symmetric probes are shown first. To analyze the E-field and H-field couplings

separately, shorted microstrip was utilized. About 40 dB/dec trend is shown from E-field coupling for both asymmetric and symmetric probes and about 20 dB/dec trend is shown from H-field coupling, indicating the mechanisms between E-field and H-field couplings are different. Surface currents shows that strong opposite eddy currents are induced on the ground loop structures under H-field coupling. The unwanted magnetic field coupling mechanism is proposed. The Hz fields induce loop currents and the currents on the top and bottom layers are in opposite directions. As a result, Hy fields are induced and coupled to the probe trace as the unwanted magnetic coupling. The Hy field is canceled at the middle of the probe, thus the unwanted magnetic coupling of symmetric probe is suppressed significantly. Two optimized designs are proposed and further demonstrating the unwanted magnetic field coupling mechanism.

REFERENCES

[1] Q. Huang et al., "Desense Prediction and Mitigation from DDR Noise Source," *2018 IEEE Symposium on Electromagnetic Compatibility, Signal Integrity and Power Integrity (EMC, SI & PI)*, Long Beach, CA, USA, 2018, pp. 139-144, doi: 10.1109/EMCSI.2018.8495224.

[2] H. Weng, D. G. Beetner and R. E. DuBroff, "Prediction of Radiated Emissions Using Near-Field Measurements," in *IEEE Transactions on Electromagnetic Compatibility*, vol. 53, no. 4, pp. 891-899, Nov. 2011, doi: 10.1109/TEMC.2011.2141998.

[3] H. Weng, D. G. Beetner, R. E. DuBroff and J. Shi, "Estimation of High-Frequency Currents From Near-Field Scan Measurements," in *IEEE Transactions on Electromagnetic Compatibility*, vol. 49, no. 4, pp. 805-815, Nov. 2007, doi: 10.1109/TEMC.2007.908264.

[4] M. Spang, T. Stoeckel, G. Schubert and M. Albach, "Application of probes with multiple outputs on probe-compensated EMC near-field measurements," *2010 IEEE International Conference on Industrial Technology*, Via del Mar, Chile, 2010, pp. 188-193, doi: 10.1109/ICIT.2010.5472677.

[5] H. -H. Chuang et al., "A Magnetic-Field Resonant Probe With Enhanced Sensitivity for RF Interference Applications," in *IEEE Transactions on Electromagnetic Compatibility*, vol. 55, no. 6, pp. 991-998, Dec. 2013, doi: 10.1109/TEMC.2013.2248011.

[6] S. Shinde, S. Marathe, G. Li, R. Zoughi and D. Pommerenke, "A Frequency Tunable High Sensitivity H-Field Probe Using Varactor Diodes and Parasitic Inductance," in *IEEE Transactions on Electromagnetic Compatibility*, vol. 58, no. 1, pp. 331-334, Feb. 2016, doi: 10.1109/TEMC.2015.2508898.

[7] N. Ando et al., "Miniaturized thin-film magnetic field probe with high spatial resolution for LSI chip measurement," *2004 International Symposium on Electromagnetic Compatibility (IEEE Cat. No.04CH37559)*, Silicon Valley, CA, USA, 2004, pp. 357-362 vol.2, doi: 10.1109/ISEMC.2004.1349815.

[8] Chun-Ping Chen, Kohei Sugawara, Zhewang Ma, Tetsuo Anada and D. W. P. Tomas, "Compact magnetic loop probe for microwave EM field-mapping and its applications in dielectric constant measurement," *2007 European Microwave Conference*, Munich, Germany, 2007, pp. 226-229, doi: 10.1109/EUMC.2007.4405167.

[9] Z. Yan, J. Wang, W. Zhang, Y. Wang and J. Fan, "A Simple Miniature Ultrawideband Magnetic Field Probe Design for Magnetic Near-Field Measurements," in *IEEE Transactions on Antennas and Propagation*, vol. 64, no. 12, pp. 5459-5465, Dec. 2016, doi: 10.1109/TAP.2016.2606556.

[10] Z. Yan, W. Liu, J. Wang, D. Su, X. Yan and J. Fan, "Noncontact Wideband Current Probes With High Sensitivity and Spatial Resolution for Noise Location on PCB," in *IEEE Transactions on Instrumentation and Measurement*, vol. 67, no. 12, pp. 2881-2891, Dec. 2018, doi: 10.1109/TIM.2018.2830859.

[11] J. Wang, Z. Yan, J. Liu, Y. Zhou, C. Fu and D. Su, "Miniature Active Differential Magnetic Field Probe With High Sensitivity for Near-Field Measurements," in *IEEE Transactions on Antennas and Propagation*, vol. 70, no. 2, pp. 1575-1580, Feb. 2022, doi: 10.1109/TAP.2021.3111300.

[12] L. Wang, X. Liu, G. Lu and Z. Zhu, "A New Method to Improve the Detection Sensitivity of Differential Magnetic-Field Probe for Near-Field Scanning," in *IEEE Transactions on Antennas and Propagation*, vol. 71, no. 7, pp. 6225-6230, July 2023, doi: 10.1109/TAP.2023.3281060.

[13] L. Wang, X. Liu, H. Wang and Z. Zhu, "A Simple Wideband Differential Magnetic Probe Loaded with Out-of-phase Balun and Parasitic Loop," in *IEEE Transactions on Antennas and Propagation*, doi: 10.1109/TAP.2023.3307937.

[14] L. Zhang, Y. -R. Feng, T. -H. Song and X. -C. Wei, "Effect of Electric Field on the Magnetic Probe," *2020 International Symposium on Electromagnetic Compatibility - EMC EUROPE*, Rome, Italy, 2020, pp. 1-3, doi: 10.1109/EMCEUROPE48519.2020.9245846.

[15] Y. -T. Chou and H. -C. Lu, "Magnetic Near-Field Probes With High-Pass and Notch Filters for Electric Field Suppression," in *IEEE Transactions on Microwave Theory and Techniques*, vol. 61, no. 6, pp. 2460-2470, June 2013, doi: 10.1109/TMTT.2013.2258034.

[16] G. Li et al., "Ultrawideband Differential Magnetic Near Field Probe With High Electric Field Suppression," in *IEEE Sensors Journal*, vol. 20, no. 14, pp. 7669-7676, 15 July15, 2020, doi: 10.1109/JSEN.2020.2981764.

[17] X. He, X. -C. Li, Z. -H. Peng, Y. -X. Liu and J. -F. Mao, "An Ultrawideband Magnetic Probe With High Electric Field Suppression Ratio," in *IEEE Transactions on Instrumentation and Measurement*, vol. 70, pp. 1-9, 2021, Art no. 8005309, doi: 10.1109/TIM.2021.3121493.

[18] H. Funato and T. Suga, "Magnetic near-field probe for GHz band and spatial resolution improvement technique," *2006 17th International Zurich Symposium on Electromagnetic Compatibility*, Singapore, 2006, pp. 284-287, doi: 10.1109/EMCZUR.2006.214926.

[19] Y. -T. Chou and H. -C. Lu, "Space Difference Magnetic Near-Field Probe With Spatial Resolution Improvement," in *IEEE Transactions on Microwave Theory and Techniques*, vol. 61, no. 12, pp. 4233-4244, Dec. 2013, doi: 10.1109/TMTT.2013.2288089.

[20] L. Wang, Y. En and Z. Zhu, "A Broadband Magnetic Probe with Multi-Components Measurement Characteristics," in *IEEE Antennas and Wireless Propagation Letters*, 2022, doi: 10.1109/LAWP.2022.3189526.

[21] L. Wang, X. Liu, Y. En and Z. Zhu, "A Composite Probe Capable of Simultaneously Measuring Two Orthogonal Magnetic-Fields," in *IEEE Transactions on Circuits and Systems II: Express Briefs*, vol. 70, no. 2, pp. 521-525, Feb. 2023, doi: 10.1109/TCSII.2022.3214731.

[22] J. Zhang, K. W. Kam, J. Min, V. V. Khilkevich, D. Pommerenke and J. Fan, "An Effective Method of Probe Calibration in Phase-Resolved Near-Field Scanning for EMI Application," in *IEEE Transactions on Instrumentation and Measurement*, vol. 62, no. 3, pp. 648-658, March 2013, doi: 10.1109/TIM.2012.2218678.

[23] S. Yang, Q. Huang, G. Li, R. Zoughi and D. J. Pommerenke, "Differential E -Field Coupling to Shielded H -Field Probe in Near-Field Measurements and a Suppression Approach," in *IEEE Transactions on Instrumentation and Measurement*, vol. 67, no. 12, pp. 2872-2880, Dec. 2018, doi: 10.1109/TIM.2018.2831398.

[24] S. Liu, X. Fang, T. Song, M. -H. Kim, H. -W. Shim and C. Hwang, "Field Coupling Mechanism Investigation of mm-Wave Magnetic Near-Field Probe Based on a Generalized Equivalent Circuit," in *IEEE Transactions on Instrumentation and Measurement*, vol. 71, pp. 1-9, 2022, Art no. 8002409, doi: 10.1109/TIM.2022.3152317.

SECTION

2. CONCLUSIONS AND RECOMMENDATIONS

In this dissertation, four papers are presented to model and analyze ESD and EMI problems. In the first paper, a simplified physics-based model for SCR-type snapback TVS devices was proposed. The model can be relatively easily tuned using only measurements performed on the package device, without the need for detailed silicon-level information. Issues with convergence were studied to determine its root cause and were eliminated by adding a non-linear damping resistance in series with the PN junction capacitance of the junction responsible for turn on. The damping resistance was set according to the simulation time step to ensure stability in a wide variety of simulation setups, though could also be set to a constant value if required for compatibility with a specific SPICE tool. Simulation results demonstrate matched measurements within about 20% for both quasistatic and transient results for each of the TLP conditions tested. Overall, this model show promise as a tool for representing TVS devices in SEED simulations. In the second paper, we proposed a phaseless EMI source imaging method based on microwave holography, which is an alternative solution for localization and characterization of active radiation sources by measuring only the magnitude of the fields. The hologram is created by combining the signal from a scan antenna with a reference signal obtained by a stationary antenna. The normalized hologram is backpropagated to the source plane and the image of sources are reconstructed. The proposed algorithm is efficient and reliable in identifying major radiation sources,

determining their location and relative strength. In the third paper, the mechanisms by which MLCCs generate acoustic noise on PCBs were studied, and a method for predicting the severity of that noise was presented. The inherent vibration properties of a PCB can be analyzed using modal analysis, and a transfer function for MLCC vibration to board response can be estimated using modal superposition. An equation predicting the PCB displacement from the MLCC/board transfer function and the MLCC power supply noise was proposed. The proposed methods were validated on a prototype earbud. The trends in the average predicted board displacement are similar to the measured acoustic noise, with the major broad peaks in the acoustic noise found in both simulations and measurement. The proposed simulation methods show promise for analyzing the impact of singing capacitors on acoustic noise. In the last paper, the unwanted magnetic field coupling of magnetic near-field probe is analyzed and explained. Shorted microstrip is utilized to separate the magnetic and electric field coupling in full wave simulation tool. Simulation results show that the opposite eddy currents on top and bottom ground loop structures are induced by the vertical magnetic field, which then generate tangential magnetic field inside the probe and couple to the probe trace. It shows that a symmetric stack-up PCB probe could mitigate the unwanted magnetic field effectively. The unwanted magnetic field coupling mechanism is validated through simulation, and optimization designs are proposed.

REFERENCES

[1] "White Paper 3: System level ESD—Part 1: Common misconceptions and recommended basic approaches, "*Industry Council on ESD Target Levels*, Dec. 2010. [Online]. Available: https://www.esdindustrycouncil.org/ic/docs/Industry%20Council%20White%20Paper%203%20PI%20Rev1%20Dec%202010.pdf

[2] P. Wei, G. Maghlakelidze, A. Patnaik, H. Gossner and D. Pommerenke, "TVS Transient Behavior Characterization and SPICE Based Behavior Model," *2018 40th Electrical Overstress/Electrostatic Discharge Symposium (EOS/ESD)*, 2018, pp. 1-10.

[3] J. Di Sarro and E. Rosenbaum, "A Scalable SCR Compact Model for ESD Circuit Simulation," *2008 IEEE International Reliability Physics Symposium*, Phoenix, AZ, USA, 2008, pp. 254-261, doi: 10.1109/RELPHY.2008.4558895.

[4] J. P. Di Sarro and E. Rosenbaum, "A Scalable SCR Compact Model for ESD Circuit Simulation," in *IEEE Transactions on Electron Devices*, vol. 57, no. 12, pp. 3275-3286, Dec. 2010, doi: 10.1109/TED.2010.2081674.

[5] R. Mertens and E. Rosenbaum, "A Physics-based Compact Model for SCR Devices Used in ESD Protection Circuits," *2013 IEEE International Reliability Physics Symposium (IRPS)*, Monterey, CA, USA, 2013, pp. 2B.2.1-2B.2.7, doi: 10.1109/IRPS.2013.6531947.

[6] N. Monnereau, F. Caignet, N. Nolhier, D. Trémouilles and M. Bafleur, "Behavioral-modeling Methodology to Predict Electrostatic-Discharge Susceptibility Failures at System Level: An IBIS Improvement," *10th International Symposium on Electromagnetic Compatibility*, York, UK, 2011, pp. 457-463.

[7] L. Wei, C. E. Gill, W. Li, R. Wang and M. Zunino, "A Convergence Robust Method to Model Snapback for ESD Simulation," *CAS 2011 Proceedings (2011 International Semiconductor Conference)*, Sinaia, Romania, 2011, pp. 369-372.

[8] F. Caignet, N. Monnereau, N. Nolhier and M. Bafleur, "Behavioral ESD Protection Modeling to Perform System Level ESD Efficient Design," *2012 Asia-Pacific Symposium on Electromagnetic Compatibility*, Singapore, 2012, pp. 401-404, doi: 10.1109/APEMC.2012.6238002.

[9] J. Zhou, Y. Xu, S. Bub, S. Holland, J. Meiguni, D. Pommerenke, D. Beetner, "Transient Response of ESD Protection Devices for a High-Speed I/O Interface," in *IEEE Transactions on Electromagnetic Compatibility*, vol. 64, no. 4, pp. 907-14, 2022.

[10] L. Shen, Y. Xu, S. Holland, S. Bub, D. Pommerenke, D. Beetner, "Application of TVS Models for SEED Simulation of a Variety of TVS Devices," *Asia-Pacific EMC Symposium*, 2023.

[11] Y. Li, Y. Wang and Y. Wang, "Modeling IC Snapback Characteristics Using a VCCS Model for Circuit-Level ESD Simulation," *2019 IEEE 26th International Symposium on Physical and Failure Analysis of Integrated Circuits (IPFA)*, Hangzhou, China, 2019, pp. 1-3, doi: 10.1109/IPFA47161.2019.8984808.

[12] J. Xiong, Z. Chen, Y. Xiu, Z. Mu, M. Raginsky and E. Rosenbaum, "Enhanced IC Modeling Methodology for System-level ESD Simulation," *2018 40th Electrical Overstress/Electrostatic Discharge Symposium (EOS/ESD)*, Reno, NV, USA, 2018, pp. 1-10.

[13] W. Liang, X. Yang, A. Loiseau, S. Mitra and R. Gauthier, "Novel ESD Compact Modeling Methodology Using Machine Learning Techniques," *2020 42nd Annual EOS/ESD Symposium (EOS/ESD)*, Reno, NV, USA, 2020, pp. 1-7.

[14] W. Liang, X. Yang, M. Miao, A. Loiseau, S. Mitra and R. Gauthier, "Novel ESD Compact Modeling Methodology Using Machine Learning Techniques for Snapback and Non-Snapback ESD Devices," in *IEEE Transactions on Device and Materials Reliability*, vol. 21, no. 4, pp. 455-464, Dec. 2021, doi: 10.1109/TDMR.2021.3116599.

[15] Y. Xu, J. Zhou, S. Bub, S. Holland, J. Meiguni, D. Pommerenke, D. Beetner, "Improved SEED Modeling of an ESD Discharge to a USB Cable," in *IEEE Transactions on Electromagnetic Compatibility*, vol. 65, no. 3, 2023.

[16] K. J. Tseng and S. Pan, "Modified charge-control equation for more realistic simulation of power diode characteristics," *Proceedings of Power Conversion Conference - PCC '97*, Nagaoka, Japan, 1997, pp. 439-444 vol.1, doi: 10.1109/PCCON.1997.645651.

[17] G. Notermans, H. Ritter, S. Holland and D. Pogany, "Dynamic Voltage Overshoot During Triggering of an SCR-Type ESD Protection," in *IEEE Transactions on Device and Materials Reliability*, vol. 19, no. 4, pp. 583-590, Dec. 2019, doi: 10.1109/TDMR.2019.2952713.

[18] F. L. Alvarado, R. H. Lasseter and J. J. Sanchez, "Testing of Trapezoidal Integration with Damping for the Solution of Power Transient Problems," in *IEEE Transactions on Power Apparatus and Systems*, vol. PAS-102, no. 12, pp. 3783-3790, Dec. 1983.

[19] *PESD3V3Y1BSF*, Nexperia. [Online]. Available: https://www.nexperia.com/products/esd-protection-tvs-filtering-and-signal-conditioning/esd-protection/low-capacitance-esd-protection-for-high-speed-interfaces/PESD3V3Y1BSF.html

[20] *PESD1V2Y1BSF*, Nexperia. [Online]. Available: https://www.nexperia.com/products/esd-protection-tvs-filtering-and-signal-conditioning/esd-protection/low-capacitance-esd-protection-for-high-speed-interfaces/PESD1V2Y1BSF.html

[21] R. Mertens, "A Compact Model for Silicon Controlled Rectifiers in Low Voltage CMOS Processes." M.S. thesis, Dept. Elect. Comput. Eng., University of Illinois at Urbana-Champaign, 2014.

[22] L. Zhang et al., "EMI Coupling Paths and Mitigation in Optical Transceiver Modules," in *IEEE Transactions on Electromagnetic Compatibility*, vol. 59, no. 6, pp. 1848-1855, Dec. 2017.

[23] P. Maheshwari, V. Khilkevich, D. Pommerenke, H. Kajbaf and J. Min, "Application of emission source microscopy technique to EMI source localization above 5 GHz," *2014 IEEE International Symposium on Electromagnetic Compatibility (EMC)*, 2014, pp. 7-11.

[24] P. Maheshwari, H. Kajbaf, V. V. Khilkevich and D. Pommerenke, "Emission Source Microscopy Technique for EMI Source Localization," in *IEEE Transactions on Electromagnetic Compatibility*, vol. 58, no. 3, pp. 729-737, June 2016.

[25] L. Zhang et al., "Sparse Emission Source Microscopy for Rapid Emission Source Imaging," in *IEEE Transactions on Electromagnetic Compatibility*, vol. 59, no. 2, pp. 729-738, April 2017.

[26] J. Li, J. Zhou, S. Yong, Y. Liu and V. Khilkevich, "Automatic sparse ESM scan using Gaussian process regression," *2020 IEEE International Symposium on Electromagnetic Compatibility & Signal/Power Integrity (EMCSI)*, 2020, pp. 671-675.

[27] M. Sørensen, H. Kajbaf, V. V. Khilkevich, L. Zhang and D. Pommerenke, "Analysis of the Effect on Image Quality of Different Scanning Point Selection Methods in Sparse ESM," in *IEEE Transactions on Electromagnetic Compatibility*, vol. 61, no. 6, pp. 1823-1831, Dec. 2019.

[28] D. Gabor, "A new microscopic principle, " *Nature*, vol. 161, no. 4098, pp. 777-778, 1948.

[29] G. Tricoles and N. H. Farhat, "Microwave holography: Applications and techniques," in *Proceedings of the IEEE*, vol. 65, no. 1, pp. 108-121, Jan. 1977.

[30] J. Laviada Martínez, A. Arboleya-Arboleya, Y. Álvarez-López, C. García-González and F. Las-Heras, "Phaseless Antenna Diagnostics Based on Off-Axis Holography With Synthetic Reference Wave," in *IEEE Antennas and Wireless Propagation Letters*, vol. 13, pp. 43-46, 2014.

[31] Tatiana Latychevskaia and Hans-Werner Fink, "Practical algorithms for simulation and reconstruction of digital in-line holograms," Appl. Opt. 54, 2424-2434 (2015).

[32] L. Zhang, Z. Zhang, C. Huang, H. Deng, H. Lin, B. Tseng, J. Drewniak and C. Hwang, "Decoupling Capacitor Selection Algorithm for PDN Based on Deep Reinforcement Learning," *2019 IEEE International Symposium on Electromagnetic Compatibility, Signal & Power Integrity (EMC+SIPI)*, 2019, pp. 616-620.

[33] B. Zhao et al., "Decoupling capacitor power ground via layout analysis for multi-layered PCB PDNs," in *IEEE Electromagnetic Compatibility Magazine*, vol. 9, no. 3, pp. 84-94, 3rd Quarter 2020.

[34] J.D. Prymak, "Piezoelectric effects ceramic chip capacitors (singing capacitors), " *Arrow Asian Times*, 2006.

[35] *Singing Capacitors (Piezoelectric Effect)*, TDK, Dec 2006. [Online]. Available: https://product.tdk.com/system/files/contents/faq/capacitors-0031/singing_capacitors_piezoelectric_effect.pdf

[36] B.H. Ko, S.G. Jeong, Y.G. Ahn, K.S. Park, N.C. Park, and Y.P. Park, "Analysis of the correlation between acoustic noise and vibration generated by a multi-layer ceramic capacitor," *Microsyst. Technol.*, vol. 20, no. 8-9 , pp.1671-1677, Aug. 2014.

[37] Y. Sun, S. Wu, J. Zhang, C. Hwang and Z. Yang, "Simulation Methodologies for Acoustic Noise Induced by Multilayer Ceramic Capacitors of Power Distribution Network in Mobile Systems," in *IEEE Transactions on Electromagnetic Compatibility*, vol. 63, no. 2, pp. 589-597, April 2021.

[38] Y. Sun, S. Wu, J. Zhang, C. Hwang and Z. Yang, "Decoupling Capacitor Layout Design Guidelines for Acoustic Noise Consideration in Power Distribution Network," *2020 IEEE International Symposium on Electromagnetic Compatibility & Signal/Power Integrity (EMCSI)*, 2020, pp. 357-362.

[39] Y. Sun, S. Wu, J. Zhang, C. Hwang and Z. Yang, "Measurement Methodologies for Acoustic Noise Induced by Multilayer Ceramic Capacitors of Power Distribution Network in Mobile Systems," in *IEEE Transactions on Electromagnetic Compatibility*, vol. 62, no. 4, pp. 1515-1523, Aug. 2020.

[40] X. Yan, S. Wu, M. Xue, C. K. B. Leung, D. Beetner and J. Zhang, "A Practical Simulation Flow for Singing Capacitor Based Acoustic Noise Analysis," *2022 IEEE International Symposium on Electromagnetic Compatibility & Signal/Power Integrity (EMCSI)*, Spokane, WA, USA, 2022, pp. 29-33.

[41] Q. Huang et al., "Desense Prediction and Mitigation from DDR Noise Source," *2018 IEEE Symposium on Electromagnetic Compatibility, Signal Integrity and Power Integrity (EMC, SI & PI)*, Long Beach, CA, USA, 2018, pp. 139-144, doi: 10.1109/EMCSI.2018.8495224.

[42] H. Weng, D. G. Beetner and R. E. DuBroff, "Prediction of Radiated Emissions Using Near-Field Measurements," in *IEEE Transactions on Electromagnetic Compatibility*, vol. 53, no. 4, pp. 891-899, Nov. 2011, doi: 10.1109/TEMC.2011.2141998.

[43] H. Weng, D. G. Beetner, R. E. DuBroff and J. Shi, "Estimation of High-Frequency Currents From Near-Field Scan Measurements," in *IEEE Transactions on Electromagnetic Compatibility*, vol. 49, no. 4, pp. 805-815, Nov. 2007, doi: 10.1109/TEMC.2007.908264.

[44] M. Spang, T. Stoeckel, G. Schubert and M. Albach, "Application of probes with multiple outputs on probe-compensated EMC near-field measurements," *2010 IEEE International Conference on Industrial Technology*, Via del Mar, Chile, 2010, pp. 188-193, doi: 10.1109/ICIT.2010.5472677.

[45] H. -H. Chuang et al., "A Magnetic-Field Resonant Probe With Enhanced Sensitivity for RF Interference Applications," in *IEEE Transactions on Electromagnetic Compatibility*, vol. 55, no. 6, pp. 991-998, Dec. 2013, doi: 10.1109/TEMC.2013.2248011.

[46] S. Shinde, S. Marathe, G. Li, R. Zoughi and D. Pommerenke, "A Frequency Tunable High Sensitivity H-Field Probe Using Varactor Diodes and Parasitic Inductance," in *IEEE Transactions on Electromagnetic Compatibility*, vol. 58, no. 1, pp. 331-334, Feb. 2016, doi: 10.1109/TEMC.2015.2508898.

[47] N. Ando et al., "Miniaturized thin-film magnetic field probe with high spatial resolution for LSI chip measurement," *2004 International Symposium on Electromagnetic Compatibility (IEEE Cat. No.04CH37559)*, Silicon Valley, CA, USA, 2004, pp. 357-362 vol.2, doi: 10.1109/ISEMC.2004.1349815.

[48] Chun-Ping Chen, Kohei Sugawara, Zhewang Ma, Tetsuo Anada and D. W. P. Tomas, "Compact magnetic loop probe for microwave EM field-mapping and its applications in dielectric constant measurement," *2007 European Microwave Conference, Munich, Germany*, 2007, pp. 226-229, doi: 10.1109/EUMC.2007.4405167.

[49] Z. Yan, J. Wang, W. Zhang, Y. Wang and J. Fan, "A Simple Miniature Ultrawideband Magnetic Field Probe Design for Magnetic Near-Field Measurements," in *IEEE Transactions on Antennas and Propagation*, vol. 64, no. 12, pp. 5459-5465, Dec. 2016, doi: 10.1109/TAP.2016.2606556.

[50] Z. Yan, W. Liu, J. Wang, D. Su, X. Yan and J. Fan, "Noncontact Wideband Current Probes With High Sensitivity and Spatial Resolution for Noise Location on PCB," in *IEEE Transactions on Instrumentation and Measurement*, vol. 67, no. 12, pp. 2881-2891, Dec. 2018, doi: 10.1109/TIM.2018.2830859.

[51] J. Wang, Z. Yan, J. Liu, Y. Zhou, C. Fu and D. Su, "Miniature Active Differential Magnetic Field Probe With High Sensitivity for Near-Field Measurements," in *IEEE Transactions on Antennas and Propagation*, vol. 70, no. 2, pp. 1575-1580, Feb. 2022, doi: 10.1109/TAP.2021.3111300.

[52] L. Wang, X. Liu, G. Lu and Z. Zhu, "A New Method to Improve the Detection Sensitivity of Differential Magnetic-Field Probe for Near-Field Scanning," in *IEEE Transactions on Antennas and Propagation*, vol. 71, no. 7, pp. 6225-6230, July 2023, doi: 10.1109/TAP.2023.3281060.

[53] L. Wang, X. Liu, H. Wang and Z. Zhu, "A Simple Wideband Differential Magnetic Probe Loaded with Out-of-phase Balun and Parasitic Loop," in *IEEE Transactions on Antennas and Propagation*, doi: 10.1109/TAP.2023.3307937.

[54] L. Zhang, Y. -R. Feng, T. -H. Song and X. -C. Wei, "Effect of Electric Field on the Magnetic Probe," *2020 International Symposium on Electromagnetic Compatibility - EMC EUROPE*, Rome, Italy, 2020, pp. 1-3, doi: 10.1109/EMCEUROPE48519.2020.9245846.

[55] Y. -T. Chou and H. -C. Lu, "Magnetic Near-Field Probes With High-Pass and Notch Filters for Electric Field Suppression," in *IEEE Transactions on Microwave Theory and Techniques*, vol. 61, no. 6, pp. 2460-2470, June 2013, doi: 10.1109/TMTT.2013.2258034.

[56] G. Li et al., "Ultrawideband Differential Magnetic Near Field Probe With High Electric Field Suppression," in *IEEE Sensors Journal*, vol. 20, no. 14, pp. 7669-7676, 15 July15, 2020, doi: 10.1109/JSEN.2020.2981764.

[57] X. He, X. -C. Li, Z. -H. Peng, Y. -X. Liu and J. -F. Mao, "An Ultrawideband Magnetic Probe With High Electric Field Suppression Ratio," in *IEEE Transactions on Instrumentation and Measurement*, vol. 70, pp. 1-9, 2021, Art no. 8005309, doi: 10.1109/TIM.2021.3121493.

[58] H. Funato and T. Suga, "Magnetic near-field probe for GHz band and spatial resolution improvement technique," *2006 17th International Zurich Symposium on Electromagnetic Compatibility*, Singapore, 2006, pp. 284-287, doi: 10.1109/EMCZUR.2006.214926.

[59] Y. -T. Chou and H. -C. Lu, "Space Difference Magnetic Near-Field Probe With Spatial Resolution Improvement," in *IEEE Transactions on Microwave Theory and Techniques*, vol. 61, no. 12, pp. 4233-4244, Dec. 2013, doi: 10.1109/TMTT.2013.2288089.

[60] L. Wang, Y. En and Z. Zhu, "A Broadband Magnetic Probe with Multi-Components Measurement Characteristics," in *IEEE Antennas and Wireless Propagation Letters*, 2022, doi: 10.1109/LAWP.2022.3189526.

[61] L. Wang, X. Liu, Y. En and Z. Zhu, "A Composite Probe Capable of Simultaneously Measuring Two Orthogonal Magnetic-Fields," in *IEEE Transactions on Circuits and Systems II: Express Briefs*, vol. 70, no. 2, pp. 521-525, Feb. 2023, doi: 10.1109/TCSII.2022.3214731.

[62] J. Zhang, K. W. Kam, J. Min, V. V. Khilkevich, D. Pommerenke and J. Fan, "An Effective Method of Probe Calibration in Phase-Resolved Near-Field Scanning for EMI Application," in *IEEE Transactions on Instrumentation and Measurement*, vol. 62, no. 3, pp. 648-658, March 2013, doi: 10.1109/TIM.2012.2218678.

[63] S. Yang, Q. Huang, G. Li, R. Zoughi and D. J. Pommerenke, "Differential E -Field Coupling to Shielded H -Field Probe in Near-Field Measurements and a Suppression Approach," in *IEEE Transactions on Instrumentation and Measurement*, vol. 67, no. 12, pp. 2872-2880, Dec. 2018, doi: 10.1109/TIM.2018.2831398.

[64] S. Liu, X. Fang, T. Song, M. -H. Kim, H. -W. Shim and C. Hwang, "Field Coupling Mechanism Investigation of mm-Wave Magnetic Near-Field Probe Based on a Generalized Equivalent Circuit," in *IEEE Transactions on Instrumentation and Measurement*, vol. 71, pp. 1-9, 2022, Art no. 8002409, doi: 10.1109/TIM.2022.3152317.

VITA

Xin Yan was born in Wugang, Henan, China. He received a Bachelor of Science in Applied Physics from Beihang University, Beijing, China, in 2015. He then joined the EMC Laboratory at the Missouri University of Science and Technology, Rolla, MO, USA. He received a Master of Science and a Doctor of Philosophy in Electrical Engineering from the Missouri University of Science and Technology in December 2018 and December 2023, respectively.

His research interests included ESD, EMI, and desense analysis.